Wave Propagation in an Elastic Half-Space with Quadratic Nonlinearity

A Thesis
Presented to
The Academic Faculty

by

Sebastian Küchler

In Partial Fulfillment
of the Requirements for the Degree
Master of Science in Engineering Science and Mechanics

School of Civil and Environmental Engineering
Georgia Institute of Technology
December 2007

Wave Propagation in an Elastic Half-Space with Quadratic Nonlinearity

Approved by:

Dr. Laurence J. Jacobs, Advisor
School of Civil and Environmental Engineering
Georgia Institute of Technology

Dr. Jianmin Qu
George W. Woodruff School of Mechanical Engineering
Georgia Institute of Technology

Dr. Reginald DesRoches
School of Civil and Environmental Engineering
Georgia Institute of Technology

Date Approved: August 24, 2007

ACKNOWLEDGEMENTS

My sincere gratitude is expressed toward everyone who has supported me in the making of this thesis and in my studies over the past five years.

I would like to thank Prof. Laurence J. Jacobs for being an outstanding advisor and friend. I am very grateful for his support and suggestions during my studies at Georgia Tech and during the work on this research. Due to his great organizational and financial efforts I received the opportunity to present the results of this thesis at the QNDE conference in Golden, Colorado. He made my stay in the U.S. a great experience.

My gratitude goes also to Prof. Jianmin Qu from the Woodruff School of Mechanical Engineering for his priceless advice in all phases of the research, and for his help to interpret the obtained results.

Moreover I would like to thank Dr. Thomas Meurer from the Technical University of Vienna for assisting me in all steps of this research. Especially in the phase of the numerical implementation, his suggestions showed me always the way out whenever I thought I was stuck. I cannot thank him enough for his advice.

I would also like to thank Prof. Reginald DesRoches for his help and support, particular in the last steps of this research.

Furthermore, my thankfulness goes to Prof. Thorsten Stoesser for granting access to the computer of his lab. Without this facility, it would be impossible to obtain the presented results in this time-frame.

I would also express my gratefulness to Dr. Jin-Yeon Kim for fruitful and interesting discussions in all phases of the research, and for his help to understand the theory of nonlinear material properties. Thanks go also to Dr. Kritsakorn Luangvilai, who

answered all my questions regarding the analytical solution of the original Lamb's problem.

For their friendship, their moral support and the interesting discussions at work I express my gratitude to my lab fellows Christoph Prüll, Richie Kmack and Dr. Kritsakorn Luangvilai. Through their contribution there was always a nice atmosphere in our lab.

In Germany, I want to thank Prof. Lothar Gaul from the University of Stuttgart for giving me the opportunity to study at Georgia Tech and furthermore the DAAD (German Academic Exchange Service) for providing generous financial support.

Finally, I am deeply indebted to my parents, who support me in an unprecedented way and always have faith in my intentions and plans. Their loving encouragement always accompanies me.

TABLE OF CONTENTS

LIST OF TABLES

LIST OF FIGURES

LIST OF SYMBOLS OR ABBREVIATIONS

FFT	fast Fourier transform
NDE	nondestructive evaluation
x, y, t	spatial and temporal coordinates
ξ	characteristic coordinate
$v(x,y,t)$, $\mathbf{v}(x,y,t)$	state-scalar equation, system
v_0, $\mathbf{v}_0$	initial condition - scalar equation, system
c	wave speed
$\mathbf{f}(\mathbf{v})$, $\mathbf{g}(\mathbf{v})$	flux vectors
$\mathbf{A}$, $\mathbf{B}$, $\mathbf{C}$, $\mathbf{D}$	system matrices
$\mathbf{d}$, $\mathbf{e}$	vectors
ν_i	ith eigenvalue
$\mathbf{r}_i$	ith eigenvector
$\mathbf{I}$	identity matrix
$\boldsymbol{\omega}$	direction in (x,y)-domain
$\mathbf{H}(\mathbf{v},\boldsymbol{\omega})$	matrix "in the direction $\boldsymbol{\omega}$"
Λ	region in (x,y)-domain
IVP	initial value problem
BVP	boundary value problem

IBVP	initial boundary value problem
j, k	indices spatial coordinates
n	index temporal coordinate
Δx, Δy	spatial stepsizes
Δt	temporal stepsize
λ, μ	ratios $\Delta t/\Delta x$ and $\Delta t/\Delta y$
$\mathbf{q}_{j,k}^n$	numerical approximation at $j\Delta x$, $n\Delta t$
$\mathbf{F}_{j,k}^n$, $\mathbf{G}_{j,k}^n$	numerical fluxes
CFL-condition	Courant-Friedrichs-Lewy condition
a_p, b_p	pth eigenvalue ν_p at $\mathbf{q}_{j,k}^n$
TVB	total variation bounded
TVD	total variation diminishing
$\bar{\mathbf{q}}$	sliding cell average
$\mathbf{p}_j$, $\mathbf{u}_k$	polynomials in $\mathbf{q}$
$\chi_{j,k}$	indicator function
ODE	ordinary differential equation
$\mathbf{q}^-$, $\mathbf{q}^+$	state behind and ahead of discontinuity
ρ	spectral radius
$(\mathbf{q}_x)_{j,k}$, $(\mathbf{q}_y)_{j,k}$	slope approximation
Θ	parameter of adjustable viscosity
σ_{ij}	stress

u, v	displacements into x- and y-direction
ρ	density
$F(t)$	excitation signal
Q	excitation amplitude
$\delta(\cdot)$	Dirac delta impulse function
λ, μ	second-order elastic constants
l, m, n	third-order elastic constants
ϕ	scalar potential
$\boldsymbol{\psi}$	vector potential
c_l, c_t, c_r	longitudinal, transverse and Rayleigh wave velocity
$\bar{f}(p)$	Laplace transformed of $f(t)$
$\hat{f}(\xi)$	Fourier transformed of $f(x)$
$s_{\cdot}$	$1/c_{\cdot}$
η	ξ/p
f_l, h_l, g_l	longitudinal displacement parts
f_t, h_t, g_t	transverse displacement parts
r, θ	radius and angle of Polar coordinates
$\eta_{\cdot\,\pm}$	Cagniard-deHoop path in the η-plane
$H(t)$	Heaviside step function
ν	Poisson's ratio
Γ	internal energy density
I_k	invariants of the strain tensor

ε	strain
$q^i\,(x,y,t)$	ith component of $\mathbf{q}\,(x,y,t)$
ν_i	ith eigenvalue
$\tilde{x}$, $\tilde{y}$	numerical boundaries
f_f	frequency of the excitation signal
t_f	duration of the excitation signal
t_{sim}	simulation time
$A\,(f)$	magnitude of the FFT
A_1	magnitude of the fundamental frequency
A_i	magnitude of the ith higher harmonic frequency
β	acoustical nonlinearity parameter
κ_x, κ_y	nonlinearity parameter for x- and y-direction
l_{Al}, m_{Al}	third-order elastic constants for Aluminum D54S
l_{a}, m_{b}	a% of l_{Al}, b% of m_{Al}
$\kappa_x^{'}$, $\kappa_y^{'}$	relative nonlinearity parameter for x- and y-direction
δ_{ij}	Kronecker delta symbol
$\nabla\mathbf{f}$	divergence
∇f	gradient
$\nabla^2\mathbf{f}$	Laplace operator
$\nabla \wedge \mathbf{f}$	curl

SUMMARY

This study investigates wave propagation in an elastic half-space with quadratic nonlinearity due to a line load on the surface. The consideration of this problem is one of the well known Lamb problems. Even since Lamb's original solution, numerous investigators have obtained solutions to many different variants of the Lamb problem. However, most of the solutions existing in the current literature are limited to wave propagation in a linear elastic half-space. In this work, the Lamb problem in an elastic half-space with quadratic nonlinearity is considered. For this, the problem is first formulated as a hyperbolic system of conservation laws, which is then solved numerically using a semi-discrete central scheme. The numerical method is implemented using the package CentPack. The accuracy of the numerical method is first studied by comparing the numerical solution with the analytical solution for a half-space with linear response (the original Lamb's problem). The numerical results for the half-space with quadratic nonlinearity are than studied using signal-processing tools such as the fast Fourier transform (FFT) in order to analyze and interpret any nonlinear effects. This in particular gives the possibility to evaluate the excitation of higher order harmonics whose amplitude is used to infer material properties. To quantify and compare the nonlinearity of different materials, two parameters are introduced; these parameters are similar to the acoustical nonlinearity parameter β for plane waves.

CHAPTER I

INTRODUCTION

Nondestructive evaluation (NDE) has evolved into an interdisciplinary area of extensive research with a broad variety of applications from non-inversive medical diagnosis to the characterization of new materials. NDE includes the development of new measurement technologies capable of making a quantitative assessment of micro- and macro-structural properties - a critical component of these techniques is the corresponding analysis and interpretation of measured data to infer a material's condition. Since measurement, analysis, and the evolution of theoretical foundations interact, the study of wave propagation for materials' characterization is an extremely challenging discipline.

To get deep insights into a material's structure and its "damage" history, the study of propagating waves in an elastic media can be very helpful. The observation of nonlinear effects in elastic waves that propagate in laboratory experiments can arise from either damaged materials, or naturally nonlinear materials such as rock or sandstone - this nonlinear behavior forms the basis for the development of an underlying theory of nonlinear wave propagation. This analysis requires the solution of nonlinear hyperbolic partial differential equations that only allow closed form solutions in a few special cases. The application of perturbation methods to these hyperbolic partial differential equations yields asymptotic solutions, and the associated disadvantages of a rather demanding and complicated analysis that often provides a solution that is valid in a limited interval (and determination of this interval is not obvious and can be difficult to determine). On the other hand, many numerical solution algorithms have been developed and successfully applied to computational fluid dynamics - these

algorithms approximate the solution to nonlinear wave propagation problems.

One classical problem in the field of wave propagation in solids, is wave propagation in a two-dimensional elastic half-space, which is also called Lamb's problem. Solving this problem analytically is even in the linear case a very demanding problem, since the free surface boundary conditions have to be taken into account. At the present, there exist many solutions to different variations of the original Lamb's problem, but most of them are limited to wave propagation in a linear elastic half-space, so they do not consider the nonlinear behavior of either damaged materials, or naturally nonlinear materials.

The objectives are to apply an advanced numerical solution procedure to solve Lamb's problem for an elastic half-space with quadratic nonlinearity. The results are used to understand the relationship between the nonlinear material response and the third-order elastic coefficients. Moreover, the dependency between the nonlinear response and the propagation distance as well as the angle to the source is exploited. All these results and relationships can be used to get more knowledge about the effects of nonlinear behavior in materials.

Especially in the case of two-dimensional wave propagation in a nonlinear elastic half-space does not exist many information in the literature. Most of the solved problems in the literature do not treat an exact half-space, as the source is not placed exactly at the free surface [28], [30] or some simplifications are applied to the governing equations [1], [30].

There exists for the case of plane waves a nonlinearity parameter, which quantifies the degree of nonlinearity present in the material. One focus of this research is to determine such a nonlinearity parameter for cylindrical waves and to investigate the relationship between this parameter and the third-order elastic coefficients from the nonlinear stress-strain relationship. Furthermore, the dependency of the nonlinear response in the media on the position in the half-space is studied.

In order to understand the numerical solution used in this research, some basic mathematical concepts are required. These concepts are introduced in Chapter 2, giving an overview about the theory of hyperbolic partial differential equations. First, some basic solution concepts for scalar partial differential equations in one dimension are introduced, thereafter follows the treatment of systems of hyperbolic partial differential equations in one and two dimensions. Chapter 3 gives in the first part an introduction to the numerical approximation of hyperbolic systems of conservation laws. In the second part of the chapter, the numerical scheme used in this research is described for one- and two-dimensional systems. Subsequently, in Chapter 4 the topic of wave propagation in an elastic half-space is treated. First, a linear elastic half-space is considered and the analytical solution to the original Lamb's problem is derived. Afterwards, the mathematical model of an elastic half-space with quadratic nonlinearity is presented. In Chapter 5 the implementation of the numerical scheme for this special problem is described and an evaluation of the convergence of the numerical solution to the analytical one is performed. The results of the numerical simulation of wave propagation in an elastic half-space with quadratic nonlinearity are presented in Chapter 6. Finally, the results are summarized and discussed in Chapter 7. An outlook on open questions and future work is given as well.

CHAPTER II

THEORY OF HYPERBOLIC PARTIAL DIFFERENTIAL EQUATIONS

Many fundamental laws of nature are expressed by partial differential equations, which frequently arise in the mathematical analysis of many diverse problems in science and engineering. One of the main reasons for developing solutions to nonlinear partial differential equations is the study of wave propagation problems, e.g. in gas dynamics, fluid dynamics and solid mechanics.

This chapter introduces the basic theoretical concepts of hyperbolic partial differential equations. Special emphasis is placed on hyperbolic systems of conservation laws in order to provide tools and support for their numerical approximation - this is important for the applications discussed in this thesis. In the first section of this chapter a brief introduction to scalar partial differential equations in one dimension is given in order to introduce the basic solution concepts. In the following part the theory of systems of hyperbolic partial differential equations is introduced in one- and two dimensions. In the last part of the chapter conservation laws in two dimensions are described and different problem formulations are discussed. In order to get a fundamental introduction, the author recommends [7], [17], and especially [29]. For a more detailed and mathematically profound treatment of the subject, the theoretical chapters of [10], and [25] as well as [27] are recommended.

In this chapter and the following ones the summation notation, i.e. summation over the repeated index, is used if not other mentioned. Furthermore, the coordinates used for the two-dimensional problems are Cartesian coordinates, if not other mentioned

2.1 Scalar Hyperbolic Equations

This section introduces the main concepts needed to determine solutions to scalar partial differential equations in one dimension. All concepts described in the following part are based on quasi-linear equations, i.e. equations of the form

$$\frac{\partial v}{\partial t} + c\left(v\right)\frac{\partial v}{\partial x} \;=\; 0, \quad x \in \mathbb{R},\ t > 0. \tag{2.1}$$

The term quasi-linear is defined in section 2.2.1 in the context of systems. One way to solve equations of the form of (2.1) is given by the method of characteristics; a short depiction of this solution procedure follows.

Consider a function $v\left(x,t\right)$ and its total derivative

$$\frac{dv}{dt} \;=\; \frac{\partial v}{\partial t} + \frac{dx}{dt}\frac{\partial v}{\partial x}. \tag{2.2}$$

By comparison, the original scalar equation (2.1) represents the total derivative of $v\left(x,t\right)$ along a curve with the slope

$$\frac{dx}{dt} \;=\; c\left(v\right) \tag{2.3}$$

at every point of the (x,t)-plane. The slope (2.3) represents the local wave speed and the curves defined by it are denoted as the characteristics of equation (2.1). From (2.2) it can easily be seen that the solution $v\left(x,t\right)$ remains constant along the characteristics, making the characteristics straight lines in the (x,t)-plane (for quasi-linear equations). But it is important to note that this straight line is not the case in general.

The solution to (2.1) can now be determined, by specifying smooth initial data

$$v\left(x, t=0\right) \;=\; g\left(x\right),\ -\infty < x < \infty. \tag{2.4}$$

If one of the characteristics intersects $t = 0$ at $x = \xi$ in the (x,t)-plane then

$$v \;=\; g\left(\xi\right) \tag{2.5}$$

on the whole of that characteristic curve. The corresponding slope of the curve is $c(g(\xi)) = G(\xi)$; it is a known function of ξ calculated from the function $c(v)$ and the given initial function $g(\xi)$. The equation of the characteristic then is

$$x = \xi + G(\xi)\, t. \tag{2.6}$$

This determines one typical curve and the value of v on it is $g(\xi)$. Allowing ξ to vary, we obtain the whole family

$$v = g(\xi), \quad c = G(\xi) = c(g(\xi)) \tag{2.7}$$

on

$$x = \xi + G(\xi)\, t. \tag{2.8}$$

To check that the implicit solution given by (2.7) and (2.8) is the solution to (2.1), the t and x derivatives of v,

$$v_t = g'(\xi)\, \xi_t \quad \text{and} \quad v_x = g'(\xi)\, \xi_x, \tag{2.9}$$

and also of (2.8)

$$\begin{aligned} 0 &= G(\xi) + [1 + G'(\xi)\, t]\, \xi_t, \\ 1 &= [1 + G'(\xi)\, t]\, \xi_x \end{aligned} \tag{2.10}$$

are taken. Therefore

$$v_t = -\frac{G(\xi)\, g'(\xi)}{1 + G'(\xi)\, t}, \quad v_x = \frac{g'(\xi)}{1 + G'(\xi)\, t}, \tag{2.11}$$

and it can be seen that

$$v_t + c(v)\, v_x = 0$$

since $c(v) = G(\xi)$. The initial condition $v = g(\xi)$ is satisfied because $\xi = x$ when $t = 0$.

Furthermore, the implicit solution (2.8) provides an interesting insight into the solution dynamics. For a deeper insight into the different phenomena of these solution dynamics, such as shock waves and rarefaction waves, the author refers for interested readers to the literature [25], [29].

2.2 Systems of Hyperbolic Equations

This section considers systems of hyperbolic partial differential equations. Firstly, one-dimensional systems are considered in order to concentrate on the main concepts and properties. After that, a brief description of two-dimensional systems is given, since they are basically extensions of the one-dimensional cases. For a more detailed insight into the topic of systems of hyperbolic equations, the author recommends [10], [25].

2.2.1 System Classification

The following part gives an overview of the classification of first-order systems of partial differential equations in one and two dimensions.

2.2.1.1 One-Dimensional Systems

The classification given in this section is based on the consideration of first-order systems of partial differential equations in one dimension, following [7], [25], [29]. But the terminology can be extended in a straightforward manner to higher-order systems. The most general, first-order system of partial differential equations in one dimension is of the form

$$\mathbf{f}\left(x,t,\mathbf{v},\mathbf{v}_x,\mathbf{v}_t\right) \;=\; 0,\ \mathbf{v}\in\mathbb{R}^P, \tag{2.12}$$

where $\mathbf{f}$ is given and $\mathbf{v}=\mathbf{v}(x,t)$ is an unknown function of the independent variables x and t. In this research x denotes a spatial variable and t the time. Equation (2.12) is said to be a nonlinear system of partial differential equations. If (2.12) is linear in its first-partial derivatives of the unknown function $\mathbf{v}(x,t)$ the resulting equation is called a quasi-linear system of partial differential equations and is given by

$$\mathbf{A}\left(x,t,\mathbf{v}\right)\mathbf{v}_t+\mathbf{B}\left(x,t,\mathbf{v}\right)\mathbf{v}_x+\mathbf{d}\left(x,t,\mathbf{v}\right) \;=\; 0,\ \mathbf{v}\in\mathbb{R}^P. \tag{2.13}$$

Equation (2.13) is called a semi-linear system of partial differential equations if its coefficient matrices $\mathbf{A}$ and $\mathbf{B}$ are independent of $\mathbf{v}$, and hence, the semi-linear system

can be expressed as

$$\mathbf{A}(x,t)\,\mathbf{v}_t + \mathbf{B}(x,t)\,\mathbf{v}_x + \mathbf{d}(x,t,\mathbf{v}) \;=\; 0,\ \mathbf{v} \in \mathbb{R}^P. \tag{2.14}$$

A system of partial differential equations is said to be linear, if $\mathbf{f}$ in (2.12) is linear in each of the variables $\mathbf{v}$, $\mathbf{v}_t$ and $\mathbf{v}_x$, and the coefficients of these variables are functions of only the independent variables x and t. The most general, first-order linear system of partial differential equations has the form

$$\mathbf{A}(x,t)\,\mathbf{v}_t + \mathbf{B}(x,t)\,\mathbf{v}_x + \mathbf{D}(x,t)\,\mathbf{v} + \mathbf{e}(x,t) \;=\; 0,\ \mathbf{v} \in \mathbb{R}^P, \tag{2.15}$$

where the coefficient matrices $\mathbf{A}$, $\mathbf{B}$ and $\mathbf{D}$, in general, are functions of x and t and the vector $\mathbf{e}(x,t)$ is given. Equations of the form (2.15) are called homogeneous if $\mathbf{e}(x,t) \equiv \mathbf{0}$ or inhomogeneous if $\mathbf{e}(x,t) \neq \mathbf{0}$.

2.2.1.2 Two-Dimensional Systems

Now, the classification for one-dimensional systems given above is extended to two-dimensional systems. Again, the classification is based on the consideration of first-order systems of partial differential equations.

The two independent spatial variables in the two-dimensional case are denoted by x and y.

- **Nonlinear System** The most general nonlinear system in two dimensions is of the form

$$\mathbf{f}(x,y,t,\mathbf{v},\mathbf{v}_x,\mathbf{v}_y,\mathbf{v}_t) \;=\; 0,\ \mathbf{v} \in \mathbb{R}^P, \tag{2.16}$$

  where $\mathbf{v} = \mathbf{v}(x,y,t)$ and $\mathbf{f}$ includes nonlinear terms of the highest appearing derivatives of $\mathbf{v}(x,y,t)$.

- **Quasi-linear System** The quasi-linear system in two dimensions is given by

$$\mathbf{A}(x,y,t,\mathbf{v})\,\mathbf{v}_t + \mathbf{B}(x,y,t,\mathbf{v})\,\mathbf{v}_x + \mathbf{C}(x,y,t,\mathbf{v})\,\mathbf{v}_y + \mathbf{d}(x,y,t,\mathbf{v}) = 0,\ \mathbf{v} \in \mathbb{R}^P. \tag{2.17}$$

- **Semi-linear System** Semi-linear systems in two dimensions are of the form

$$\mathbf{A}(x,y,t)\,\mathbf{v}_t+\mathbf{B}(x,y,t)\,\mathbf{v}_x+\mathbf{C}(x,y,t)\,\mathbf{v}_y+\mathbf{d}(x,y,t,\mathbf{v})=0,\ \mathbf{v}\in\mathbb{R}^P. \quad (2.18)$$

- **Linear Systems** The most general, first-order linear system of partial differential equations in two dimensions is expressed by

$$\mathbf{A}(x,y,t)\,\mathbf{v}_t+\mathbf{B}(x,y,t)\,\mathbf{v}_x+\mathbf{C}(x,y,t)\,\mathbf{v}_y+\mathbf{D}(x,y,t)\,\mathbf{v}+\mathbf{e}(x,y,t)=0,\ \mathbf{v}\in\mathbb{R}^P, \quad (2.19)$$

  where the coefficient matrices $\mathbf{A}$, $\mathbf{B}$, $\mathbf{C}$ and $\mathbf{D}$ are functions of x, y and t and the vector $\mathbf{e}(x,y,t)$ is given. As in the one-dimensional case, one can distinguish between homogeneous ($\mathbf{e}\equiv\mathbf{0}$) and inhomogeneous ($\mathbf{e}\neq\mathbf{0}$) systems.

2.2.2 Hyperbolicity and Characteristics

In the following section conditions for first-order quasi-linear systems to be hyperbolic are established. As many physical problems lead to formulations of a quasi-linear system of first-order equations, only these type of equations is considered below.

2.2.2.1 One Dimension

As described in section 2.1, the key to the solution of a single first-order equation (2.1) was the use of the family of characteristic curves in the (x,t)-plane; along each characteristic curve the partial differential equation could be reduced to an ODE. Following [29], the solution to (2.1) can be build up by successive "local" considerations of small regions; the whole solution has not to be calculated at once. This, of course, corresponds to the simple ideas of wave phenomena; in any small time increment the behavior at a point can be influenced only by points near enough for their waves to arrive in time. For the system (2.13) arises the question whether such local calculations are possible. If they are, the system is hyperbolic and a suitable precise definition will be framed.

In order to answer the question if a general quasi-linear system in one dimension (defined by (2.13)) is hyperbolic, consider the development given by [29] that is based on the question if there exists a linear combination

$$l_i \left(A_{ij} \frac{\partial v_j}{\partial t} + B_{ij} \frac{\partial v_j}{\partial x} \right) + l_i d_i \quad = \quad 0, \tag{2.20}$$

where the vector $\mathbf{l}$ is a function of x, t, $\mathbf{v}$ such that (2.20) takes the form

$$m_j \left(\beta \frac{\partial v_j}{\partial t} + \alpha \frac{\partial v_j}{\partial x} \right) + l_j d_j \quad = \quad 0. \tag{2.21}$$

If this is possible, (2.21) provides a relation between the directional derivatives

$$\frac{\partial v_j}{\partial \mathbf{a}} = (\nabla v_j)^T \cdot \mathbf{a}, \quad \text{with } a = [\alpha, \beta]^T \tag{2.22}$$

of all v_j in the single direction $[\alpha, \beta]^T$. By this, curves defined by the vector field $[\alpha, \beta]^T$ in the (x,t)-plane can be introduced. Let $x = X(\eta)$ and $t = T(\eta)$ denote a parametric representation of a typical member of this family. Consider the total derivative of v_j on the curve

$$\frac{dv_j}{d\eta} \quad = \quad \frac{\partial v_j}{\partial t} T'(\eta) + \frac{\partial v_j}{\partial x} X'(\eta) \tag{2.23}$$

and take

$$\alpha = X'(\eta), \quad \beta = T'(\eta). \tag{2.24}$$

Equation (2.21) can now be rewritten in characteristic form

$$m_j \frac{dv_j}{d\eta} + l_j d_j = 0 \ \text{ on } \frac{dX}{d\eta} = \alpha, \ \frac{dT}{d\eta} = \beta. \tag{2.25}$$

Now determine the conditions for (2.20) to be in the form (2.21)

$$l_i A_{ij} = m_j T', \quad l_i B_{ij} = m_j X'. \tag{2.26}$$

Elimination of m_j yields

$$l_i \left(A_{ij} X' - B_{ij} T' \right) \quad = \quad 0, \tag{2.27}$$

which provides a nontrivial solution under the necessary and sufficient condition

$$|A_{ij}X' - B_{ij}T'| \;=\; 0. \tag{2.28}$$

The calculation above, together with a condition (2.29) to exclude degenerate cases (i.e. singularity of $\mathbf{A}$ and/or $\mathbf{B}$), yield the following definition of hyperbolicity in one dimension [29].

Definition 2.1 (Hyperbolicity in One Dimension)**.** *A system (2.13), satisfying*

$$|\nu A_{ij} + \mu B_{ij}| \;\neq\; 0, \tag{2.29}$$

for some ν, μ but not both zero, is hyperbolic if P linearly independent real vectors $\mathbf{l}^{(p)},\ p = 1, \ldots, P$, can be found such that

$$\mathbf{l}_i^{(p)} \left\{ A_{ij}\alpha^{(p)} - B_{ij}\beta^{(p)} \right\} \;=\; 0 \tag{2.30}$$

for each p, and the corresponding directions $\left[\alpha^{(p)}, \beta^{(p)}\right]$ are real with $\alpha^{(p)^2} + \beta^{(p)^2} \neq 0$.

It should be noted that the emphasis is on there being P independent vectors $\mathbf{l}^{(p)}$, and it is not important that the corresponding directions $\left[\alpha^{(p)}, \beta^{(p)}\right]$ be distinct. If the directions are distinct so that there are P different families of characteristics, the system is said to be strictly hyperbolic.

In many problems, the system (2.13) appears in the special form

$$\mathbf{v}_t + \mathbf{B}\left(x, t, \mathbf{v}\right)\mathbf{v}_x + \mathbf{d}\left(x, t, \mathbf{v}\right) \;=\; 0,\ \mathbf{v} \in \mathbb{R}^P, \tag{2.31}$$

where the $\mathbf{A}$ matrix is the unit matrix. In this special case, system (2.31) is said to be hyperbolic if the P eigenvalues ν of the matrix $\mathbf{B}$

$$\left(\mathbf{B} - \nu\mathbf{I}\right)\mathbf{r} \;=\; 0 \tag{2.32}$$

are real with a complete family of (right) eigenvectors $\mathbf{r}$. If the P eigenvalues are real and distinct, it is ensured that the corresponding eigenvectors are linearly independent

and the system is called strictly hyperbolic. The eigenvalues define characteristic velocities along characteristic curves $x = X(t)$ given by

$$\frac{dX(t)}{dt} = \nu. \tag{2.33}$$

The quasi-linear system (2.31) can now be transformed by (2.32), (2.33) into the characteristic form

$$\frac{dv_i}{dt} r_i + d_i r_i = 0 \quad \text{on} \quad \frac{dX}{dt} = \nu. \tag{2.34}$$

It is necessary to emphasize that the eigenvalues ν as well as the eigenvectors $\mathbf{r}$ may be functions of x, t and the variables $v_1, \ldots, v_P$.

2.2.2.2 Two Dimensions

The theoretical aspects for two-dimensional systems of partial differential equations are not fully understood yet and are much more complex than the scalar case or in the one-dimensional case [10]. Therefore only the special case of (2.17) with $\mathbf{A} = \mathbf{I}$, given by

$$\mathbf{v}_t + \mathbf{B}(x, y, t, \mathbf{v})\,\mathbf{v}_x + \mathbf{C}(x, y, t, \mathbf{v})\,\mathbf{v}_y + \mathbf{d}(x, y, t, \mathbf{v}) = 0, \ \mathbf{v} \in \mathbb{R}^P \tag{2.35}$$

is considered. In order to state whether the system (2.35) is hyperbolic or not, the development given by [10] is considered. Hence, the $P \times P$ matrix $\mathbf{H}(\mathbf{v}, \boldsymbol{\omega})$ "in the direction $\boldsymbol{\omega}$" is defined for $\mathbf{v} = [v_1, \ldots, v_P]^T \in \mathbb{R}^P$ and $\boldsymbol{\omega} = [\omega_x, \omega_y]^T \in \mathbb{R}^2$ by

$$\mathbf{H}(\mathbf{v}, \boldsymbol{\omega}) = \mathbf{B} \cdot \omega_x + \mathbf{C} \cdot \omega_y. \tag{2.36}$$

Together with this matrix, hyperbolicity in two dimensions for systems of the form (2.35) can be defined [10].

Definition 2.2 (Hyperbolicity in Two Dimensions)**.** *The system (2.35) is called hyperbolic if for any* $\mathbf{v}$ *and any direction* $\boldsymbol{\omega}$*,* $|\boldsymbol{\omega}| = 1$*, the matrix* $\mathbf{H}(\mathbf{v}, \boldsymbol{\omega})$ *defined by (2.36) has* P *real eigenvalues* ν *with a complete family of (right) eigenvectors* $\mathbf{r}$*.*

It has to be denoted that the eigenvalues ν as well as the eigenvectors $\mathbf{r}$ may be functions of x, y, t, the direction $[\omega_x, \omega_y]^T$ and the variables $v_1, \ldots, v_P$.
Moreover, the system is strictly hyperbolic at a state $\mathbf{v}$ if the P eigenvalues are distinct.

2.2.3 Loss of Hyperbolicity

For some nonlinear physical systems there are regions of state space in which the hyperbolic system looses its hyperbolicity and changes to another type of equations [17]. In the special case of $\mathbf{A} = \mathbf{I}$, it may happen that the Jacobian Matrix of $\mathbf{f}(\mathbf{v})$ and/or $\mathbf{g}(\mathbf{v})$ (only in the two-dimensional case) has real eigenvalues at most points in state space but has complex eigenvalues over some relatively small region, called the elliptic region of state space. It is then an equation of mixed type. In this case it may be that wavelike solutions exist and the Cauchy Problem (which is introduced in section 2.3.2.1) is well posed, at least for certain initial data, in spite of the elliptic region. But the theory of such problems is beyond the scope of this research, therefore the author refers to [17] and the references therein.

2.3 Systems of Conservation Laws

The terminology of conservation laws is of great importance since this research considers the solution of wave propagation problems in continuous media. This is the case because many wave propagation problems described by higher order partial differential equations can be transformed into the conservation form and, because various numerical algorithms have been proposed for this special class (conservation form) of systems.
Only two-dimensional conservation laws are treated in this section. The one-dimensional case can be easily derived from the two-dimensional one by neglecting the terms of the second spatial variable y. For a more detailed description of this topic the author recommends [27] for one-dimensional conservation laws and [10] for several space

dimensions.

2.3.1 Definition

Consider a partial differential equation of the form

$$\frac{\partial \mathbf{v}}{\partial t} + \frac{\partial}{\partial x}\mathbf{f}(\mathbf{v}) + \frac{\partial}{\partial y}\mathbf{g}(\mathbf{v}) \;=\; \mathbf{0}, \quad [x, y] \in \mathbb{R}^2,\ t > 0, \tag{2.37}$$

where

$$\mathbf{v} \;=\; [v_1, v_2, \ldots, v_P]^T$$

is a vector-valued function from $\mathbb{R}^2 \times [0, \infty)$ into the set of states Ω, and the functions

$$\mathbf{f} = [f_1, f_2, \ldots, f_P]^T \quad \text{and} \quad \mathbf{g} = [g_1, g_2, \ldots, g_P]^T$$

are called flux functions. Equation (2.37) is in conservation form and is called a conservation law [10], [17], [27].

Integration of (2.37) by parts with respect to x, y and t over $\Lambda = [x_1, x_2] \times [y_1, y_2]$ and from t_1 to t_2, respectively, yields the integral form of the conservation law in two dimensions

$$\begin{aligned} \mathbf{0} \;=\; & \int_{x_1}^{x_2}\int_{y_1}^{y_2} [\mathbf{v}(x, y, t_2) - \mathbf{v}(x, y, t_1)]\, dy\, dx + \\ & \int_{t_1}^{t_2}\int_{y_1}^{y_2} [\mathbf{f}(\mathbf{v}(x_2, y, t)) - \mathbf{f}(\mathbf{v}(x_1, y, t))]\, dy\, dt + \\ & \int_{t_1}^{t_2}\int_{x_1}^{x_2} [\mathbf{g}(\mathbf{v}(x, y_2, t)) - \mathbf{g}(\mathbf{v}(x, y_1, t))]\, dx\, dt. \end{aligned} \tag{2.38}$$

This formulation (2.38) allows a physical interpretation into the way that the change of conserved quantity $\mathbf{v}$ in the domain $\Lambda = [x_1, x_2] \times [y_1, y_2]$ between times t_1 and t_2 equals the flux of this quantity over the boundaries of the domain in the time interval $[t_1, t_2]$.

System (2.37) is hyperbolic [10], [27], if the $P \times P$ Jacobian Matrices

$$\mathbf{B} = \begin{bmatrix} \dfrac{\partial f_1}{\partial v_1} & \cdots & \dfrac{\partial f_1}{\partial v_P} \\ \vdots & & \vdots \\ \dfrac{\partial f_P}{\partial v_1} & \cdots & \dfrac{\partial f_P}{\partial v_P} \end{bmatrix} \quad \text{and} \quad \mathbf{C} = \begin{bmatrix} \dfrac{\partial g_1}{\partial v_1} & \cdots & \dfrac{\partial g_1}{\partial v_P} \\ \vdots & & \vdots \\ \dfrac{\partial g_P}{\partial v_1} & \cdots & \dfrac{\partial g_P}{\partial v_P} \end{bmatrix} \tag{2.39}$$

fulfill the conditions for hyperbolicity given in definition 2.36.

2.3.2 Problem Formulations

The solution of a partial differential equation requires the specification of variables on the borders of the domain under consideration. Initial value, boundary value and initial-boundary value problems are briefly introduced in this section.

2.3.2.1 Initial Value Problem

The Cauchy problem or initial value problem (IVP) for hyperbolic systems can be stated as [10]: find a function $\mathbf{v} : (x, y, t) \in \mathbb{R}^2 \times [0, \infty) \rightarrow \mathbf{v}(x, y, t)$ that is a solution to (2.37) satisfying the initial condition

$$\mathbf{v}(x, y, 0) \;=\; \mathbf{v}_0(x, y), \; [x, y] \in \mathbb{R}^2, \tag{2.40}$$

where $\mathbf{v}_0$ is a given function.

If the function $\mathbf{v}_0(x, y)$ is given in the following form

$$\mathbf{v}_0(x, y) \;=\; \begin{cases} \mathbf{v}_{LB}, & x < 0,\, y < 0 \\ \mathbf{v}_{LT}, & x < 0,\, y > 0 \\ \mathbf{v}_{RB}, & x > 0,\, y < 0 \\ \mathbf{v}_{RT}, & x > 0,\, y > 0 \end{cases} \tag{2.41}$$

then the Cauchy problem is called the Riemann problem [10]. Riemann problems play an important role in the numerical approximation of hyperbolic systems of conservation laws based on so called upwind schemes, which are not treated in this thesis, therefore the author refers to the literature [10], [17], [27].

2.3.2.2 Boundary Value Problem

The treatment of boundary value problems (BVPs) requires special caution, because of (among other conditions) the well-posedness of the problem. A BVP is defined as the problem of finding a solution to (2.37) in a domain Λ with boundary $\partial\Lambda$ under the condition

$$\mathbf{v}\left(x, y, t\right)|_{\partial\Lambda} = \mathbf{h}\left(t\right), \tag{2.42}$$

where (2.42) represents the most simple family of boundary conditions.

It has to be mentioned that in contrast to IVPs, even the most innocent looking BVP may have exactly one solution, no solution, or an infinite number of solutions [22]. On the other hand, the numerical solution of conservation laws requires the specification of initial, as well as boundary conditions. This leads to initial boundary value problems presented briefly in the next section.

2.3.2.3 Initial Boundary Value Problem

An initial boundary value problem (IBVP) combines the attributes discussed above, and hence can be defined as finding the solution to (2.37), satisfying initial (2.40) and boundary (2.42) conditions. A classical example for an IBVP in two dimensions is given in 4.1, where the solution to Lamb's original problem is calculated.

In general, an IBVP is ill-posed [10], which means that there may be no solution or one that does not depend in a continuous way on the initial or boundary data or nonuniqueness. For nonlinear systems of conservation laws, the solution of IBVPs and their analytical treatment is very demanding - one cannot expect any general existence theorems. Nevertheless, some problem specific results have been achieved which involve boundary entropy considerations and hence admissible boundary values (see, for example, [10] and the references therein).

CHAPTER III

HIGH-RESOLUTION CENTRAL SCHEMES

Some basic theoretical concepts for the numerical solution of hyperbolic systems of conservation laws are introduced in this section. This chapter is organized in a way that first the general concepts for the one- and two-dimensional cases are introduced. In the second part of this chapter, the numerical schemes, used in this research, are described for the one- and two-dimensional cases.

For a detailed treatment of the numerical solution of hyperbolic systems of conservation laws the author recommends consulting [10], [17], [24] and [27].

3.1 General Concepts

In order to approximate the solution of a nonlinear conservation law, some basic concepts are introduced; these concepts specifically relate to the numerical solution of hyperbolic systems. The general concepts, described in this section hold for all Finite Difference Schemes, since Central Schemes correspond to the family of Finite Difference Schemes. The fundamental notions of consistency, convergence, and stability are assumed to be known and will be used without definition.

3.1.1 One-Dimensional Systems

For the one-dimensional case, consider the Cauchy problem

$$\frac{\partial \mathbf{v}}{\partial t} + \frac{\partial}{\partial x}\mathbf{f}(\mathbf{v}) = \mathbf{0}, \quad x \in \mathbb{R},\ t > 0 \tag{3.1}$$

$$\mathbf{v}(x,0) = \mathbf{v}_0(x), \tag{3.2}$$

where $\mathbf{v} \in \mathbb{R}^P$ under the assumption that the system is hyperbolic.

Given an uniform grid with time step Δt and spatial mesh size Δx, an approximation

$\mathbf{q}_j^n$ of $\mathbf{v}(x_j, t_n)$ at the point $(x_j = j\Delta x, t_n = n\Delta t)$ can be defined by the following formula

$$\mathbf{q}_j^{n+1} = \mathbf{q}_j^n - \lambda\left(\mathbf{F}_{j+\frac{1}{2}}^n - \mathbf{F}_{j-\frac{1}{2}}^n\right), \quad j \in \mathbb{Z},\ n \geq 0, \tag{3.3}$$

where $\left(\mathbf{q}_j^0\right)_{j\in\mathbb{Z}}$ is given and $\lambda = \frac{\Delta t}{\Delta x}$ [10]. The continuous function $\mathbf{F}_{j+\frac{1}{2}}^n$ is in general given by

$$\mathbf{F}_{j+\frac{1}{2}}^n = \mathbf{F}\left(\mathbf{q}_{j-J+1}^n, \ldots, \mathbf{q}_{j+J}^n\right), \tag{3.4}$$

where $\mathbf{F} : \mathbb{R}^{P\times 2J} \to \mathbb{R}^P$ and is called the numerical flux. This scheme is said to be consistent [10], [27] with (3.1) if $\mathbf{F}$ satisfies

$$\mathbf{F}(\mathbf{v}, \ldots, \mathbf{v}) = \mathbf{f}(\mathbf{v}), \quad \forall \mathbf{v} \in \mathbb{R}^P. \tag{3.5}$$

The general formulation (3.4) is a $(2J+1)$ scheme, and for $J = 1$ it reduces to a 3-point scheme. A difference scheme is called conservative if it can be written in the form of (3.3), which is called the conservative form. Next, a fundamental theorem [10], [24], [27] for the development of so called "shock capturing" methods will be stated. The limit solutions are weak solutions, if a conservative scheme is used, or

Theorem 3.1 (Lax-Wendroff Theorem)**.** *If $\mathbf{q}_j^n$ is a discrete solution based on a consistent, conservative difference approximation to a given conservation law initial-value problem (3.1), (3.2) and if $\mathbf{q}_j^n \to \mathbf{v}$ in $L_{1,loc}$ (space of locally Lebesgue integrable functions) as $\Delta x, \Delta t \to 0$, then $\mathbf{v} = \mathbf{v}(x,t)$ is a weak solution to the initial-value problem.*

A very important condition for the approximation of hyperbolic systems is the Courant-Friedrichs-Lewy condition (CFL condition) [10], [17], [26], [27]. Finite speed of propagation of disturbances characterize hyperbolic systems. Hence, if for some reason the speed of propagation for the difference scheme is greater than the speed of propagation of the conservation law, at a given point the limiting solution of the difference scheme could be completely unaware of a part of the initial condition on which the

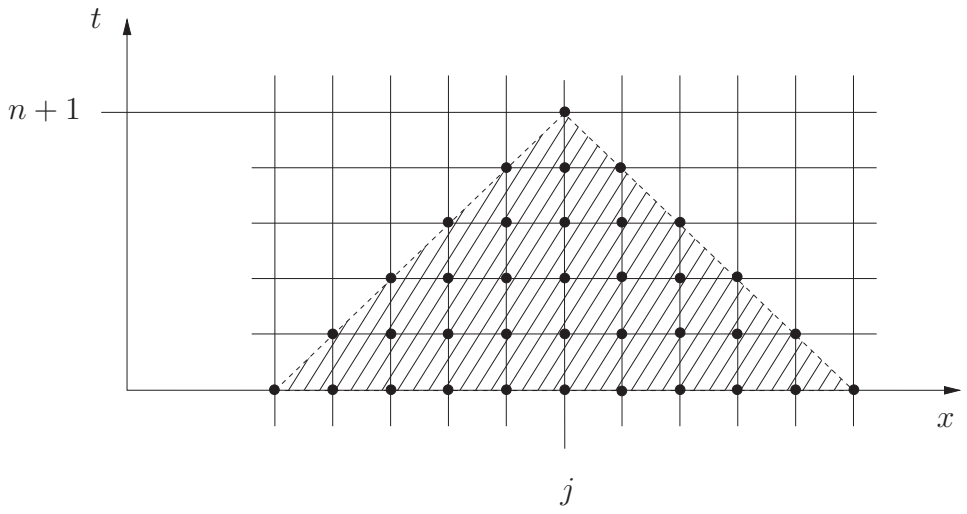

Figure 3.1: Numerical domain of dependence (hatched) of point (x_j, t_n).

solution depends on that point. Therefore, it would be impossible for the limiting solution of the difference scheme to be the same as the analytical solution. In other words, the analytical domain of dependence of the solution at a given point has to be completely included in the numerical domain of dependence of the difference scheme at the same point. In order to illustrate this, the numerical domain of dependence of a 3-point scheme, i.e.

$$\mathbf{q}_j^{n+1} \;=\; \mathbf{q}_j^n - \lambda \left(\mathbf{F}\left(\mathbf{q}_j^n, \mathbf{q}_{j+1}^n\right) - \mathbf{F}\left(\mathbf{q}_{j-1}^n, \mathbf{q}_j^n\right)\right)$$

in the (x,t)-domain is depicted in Figure 3.1.

For the 3-point scheme under consideration, the (discrete) nonlinear CFL condition is given by

$$\lambda_{\max} \left| a_p\left(\mathbf{q}_j^n\right)\right| \;\leq\; 1, \quad 1 \leq p \leq P, \tag{3.6}$$

where $a_p(\mathbf{v})$ denotes the pth eigenvalue $\nu_p(\mathbf{v})$ of the Jacobian matrix $\frac{\partial \mathbf{f}(\mathbf{v})}{\partial \mathbf{v}}$. For the convergence of nonlinear difference schemes to approximate the solution to nonlinear hyperbolic systems, the nonlinear CFL condition, e.g. (3.6) for a 3-point scheme, will be treated as a necessary condition, although this is not as clear as for linear systems. Here it can be shown, that the CFL condition is necessary for the convergence of

linear difference equations to solve linear, hyperbolic partial differential equations. Next, a short introduction to total variation bounded (TVB) approximations is given - this portion illustrates the accuracy and convergence properties of numerical schemes. A very detailed treatment of these terms is presented in [10] and [24]. In the scalar case, i.e. $P = 1$, the TVB notion is replaced by the total variation diminishing (TVD) notion.

Definition 3.1 (Total Variation Diminishing Scheme)**.** *A difference scheme for scalar equations is said to be TVD if the solution produced by the scheme satisfies*

$$\sum_{j\in\mathbb{Z}} \left|q_{j+1}^{n+1} - q_j^{n+1}\right| \;\leq\; \sum_{j\in\mathbb{Z}} \left|q_{j+1}^{n} - q_j^{n}\right|, \quad \forall n > 0.$$

TVD schemes are very attractive because they share the following properties [10], [24]

- convergence
- exclusion of spurious oscillations
- accuracy not restricted to first-order.

Since scalar 3-point schemes are limited to first-order accuracy, high-order approximations can only be developed using 5-point or higher schemes. The extension of Definition 3.1 to systems of hyperbolic equations is not straightforward. Nevertheless, some form of stability is required to guarantee convergence. Hence, the notion of TVB approximations is briefly introduced.

Definition 3.2 (Total Variation Bounded Scheme)**.** *A difference scheme for systems of equations is said to be TVB if the solution produced by the scheme satisfies*

$$TV\left(\mathbf{q}^n\right) \;=\; \sum_{j\in\mathbb{Z}} \left\|\mathbf{q}_{j+1}^{n} - \mathbf{q}_j^{n}\right\| \leq \mathit{Const.},$$

where $\|\cdot\|$ *denotes the usual* $\mathbb{R}^P$ *norm.*

A more detailed treatment of the TVB notion, and hence the convergence of an approximate solution, is outside of the scope of this research and interested readers see [24] for details.

The development of numerical schemes for the solution approximation to conservation laws is based on an appropriate ansatz for the solution inside the grid cells, i.e. introduce the sliding cell average

$$\bar{\mathbf{q}} = \frac{1}{I_x}\int_{I_x}\mathbf{q}(\xi,t)\,d\xi, \tag{3.7}$$

where $I_x = \{\xi : 0 \le \xi - x \le \Delta x\}$ (central idea) or $I_x = \left\{\xi : |\xi - x| \le \frac{\Delta x}{2}\right\}$ (upwind idea), and approximate the solution by the general ansatz

$$\tilde{\mathbf{q}}(x,t^n) = \sum_j \mathbf{p}_j \chi_j(x). \tag{3.8}$$

Where $\mathbf{p}_j$ denotes, in general a polynomial in $\bar{\mathbf{q}}_j^n \approx \bar{\mathbf{q}}(x_j,t^n)$ and reconstructed derivatives $\frac{\partial^m \mathbf{q}}{\partial x^m}$ up to finite order m. It is clear that the order of the scheme, and therefore its accuracy, depends on the maximum order of spatial derivatives $\frac{\partial^m \mathbf{q}}{\partial x^m}$ selected in (3.8). The term $\chi_j(x)$ denotes an indicator function, that is $\chi_j(x) = \mathbf{1}_{\left[x_j - \frac{\Delta x}{2}, x_j + \frac{\Delta x}{2}\right]}$, where $\mathbf{1}_{[a,b]} = 1$ in $[a,b]$ and 0 elsewhere. Starting from the approximations (3.7), (3.8) the integral form of the equations, given in the one-dimensional case by

$$\mathbf{0} = \int_{x_1}^{x_2}\left[\mathbf{v}(x,t_2) - \mathbf{v}(x,t_1)\right]dx + \int_{t_1}^{t_2}\left[\mathbf{f}(\mathbf{v}(x_2,t)) - \mathbf{f}(\mathbf{v}(x_1,t))\right]dt, \tag{3.9}$$

can be used to determine how the cell average varies with time. With this information a numerical scheme based on numerical approximations to the fluxes at each cell edge can be developed. Various approaches to doing this are available [17].

3.1.2 Two-Dimensional Systems

The theory of difference schemes for two-dimensional conservation laws is much less developed than the theory for one- dimensional conservation laws [27]. Nevertheless, in the following part the general concepts introduced above for the one-dimensional

case are extended to systems of conservation laws in two dimensions. Therefore, consider the two-dimensional $P \times P$ hyperbolic system

$$\frac{\mathbf{v}}{\partial t} + \frac{\partial}{\partial x}\mathbf{f}\left(\mathbf{v}\right) + \frac{\partial}{\partial y}\mathbf{g}\left(\mathbf{v}\right) \;\; = \;\; \mathbf{0}, \;\; [x,y] \in \mathbb{R}^2, \; t > 0, \tag{3.10}$$

where $\mathbf{v} \in \mathbb{R}^P$ under the assumption that the system is hyperbolic. The corresponding initial conditions are given by

$$\mathbf{v}\left(x,y,0\right) \;\; = \;\; \mathbf{v}_0\left(x,y\right). \tag{3.11}$$

Assuming a two-dimensional uniform Cartesian spatial grid $\Delta = \Delta x \times \Delta y$ with space increments Δx and Δy and time step Δt, an approximation $\mathbf{q}_{j,k}^n$ can be defined by

$$\mathbf{q}_{j,k}^{n+1} = \mathbf{q}_{j,k}^n - \lambda\left(\mathbf{F}_{j+\frac{1}{2},k}^n - \mathbf{F}_{j-\frac{1}{2},k}^n\right) - \mu\left(\mathbf{G}_{j,k+\frac{1}{2}}^n - \mathbf{G}_{j,k-\frac{1}{2}}^n\right), \;\; j,k \in \mathbb{Z}, \; n \geq 0, \tag{3.12}$$

where $\left(\mathbf{q}_{j,k}^0\right)_{j\in\mathbb{Z}}$ is given and

$$\lambda = \frac{\Delta t}{\Delta x}, \quad \mu = \frac{\Delta t}{\Delta y}.$$

The continuous functions $\mathbf{F}_{j+\frac{1}{2},k}^n$ and $\mathbf{G}_{j,k+\frac{1}{2}}^n$ are given by

$$\begin{aligned} \mathbf{F}_{j+\frac{1}{2},k}^n &= \mathbf{F}\left(\mathbf{q}_{j-J+1,k-K}^n, \ldots, \mathbf{q}_{j+J,k+K}^n\right), \\ \mathbf{G}_{j,k+\frac{1}{2}}^n &= \mathbf{G}\left(\mathbf{q}_{j-J,k-K+1}^n, \ldots, \mathbf{q}_{j+J,k+K}^n\right), \end{aligned} \tag{3.13}$$

where $\mathbf{F} : \mathbb{R}^{2J\times(2K+1)\times P} \to \mathbb{R}^P$ and $\mathbf{G} : \mathbb{R}^{(2J+1)\times 2K\times P} \to \mathbb{R}^P$ are called, as in the one-dimensional case, the numerical fluxes. The scheme given by (3.12) is again in conservation form. As with the one-dimensional conservation laws (3.1), the consistency of the difference scheme can be related to the relationship between $\mathbf{f}$ and $\mathbf{F}$, and $\mathbf{g}$ and $\mathbf{G}$. Hence, the two-dimensional difference scheme (3.12) is said to be consistent [10], [27] with (3.10) if $\mathbf{F}$ and $\mathbf{G}$ satisfy

$$\mathbf{F}\left(\mathbf{v},\ldots,\mathbf{v}\right) = \mathbf{f}\left(\mathbf{v}\right) \quad \text{and} \quad \mathbf{G}\left(\mathbf{v},\ldots,\mathbf{v}\right) = \mathbf{g}\left(\mathbf{v}\right), \quad \forall \mathbf{v} \in \mathbb{R}^P. \tag{3.14}$$

Often there are used simpler formulas where $\mathbf{F}_{j+\frac{1}{2},k} = \mathbf{F}\left(\mathbf{q}_{j-J+1,k},\ldots,\mathbf{q}_{j+J,k}\right)$ and $\mathbf{G}_{j,k+\frac{1}{2}} = \mathbf{G}\left(\mathbf{q}_{j,k-K+1},\ldots,\mathbf{q}_{j,k+K}\right)$ depends only on $2J$ and $2K$ values, respectively.

Naturally, these formulas can be obtained by starting from one-dimensional numerical fluxes $\mathbf{F} : \mathbb{R}^{2J\times P} \to \mathbb{R}^P$ and $\mathbf{G} : \mathbb{R}^{2K\times P} \to \mathbb{R}^P$ consistent respectively with $\mathbf{f}$ and $\mathbf{g}$. There can also be taken a combination of one-dimensional numerical fluxes consistent respectively with $2\mathbf{f}$ and $2\mathbf{g}$; for $J = K = 1$ this ends up in the following 5-point scheme, i.e.

$$\begin{aligned}\mathbf{q}_{j,k}^{n+1} &= \mathbf{q}_{j,k}^n + \frac{\lambda}{2}\left(\mathbf{F}\left(\mathbf{q}_{j,k}^n, \mathbf{q}_{j+1,k}^n\right) - \mathbf{F}\left(\mathbf{q}_{j-1,k}^n, \mathbf{q}_{j,k}^n\right)\right) \\ &\quad + \frac{\mu}{2}\left(\mathbf{G}\left(\mathbf{q}_{j,k}^n, \mathbf{q}_{j,k+1}^n\right) - \mathbf{G}\left(\mathbf{q}_{j,k}^n, \mathbf{q}_{j,k-1}^n\right)\right). \end{aligned} \tag{3.15}$$

Just as for one-dimensional difference schemes, the CFL condition is also a very important condition for two-dimensional difference schemes; the reason for that is in general the same as in the one-dimensional case. For the 5-point scheme given above, the (discrete) nonlinear CFL condition is given by

$$\lambda_{\max}\left|a_p\left(\mathbf{q}_{j,k}^n\right)\right| \le \frac{1}{2} \quad \text{and} \quad \mu_{\max}\left|b_p\left(\mathbf{q}_{j,k}^n\right)\right| \le \frac{1}{2}, \quad 1 \le p \le P, \tag{3.16}$$

where $a_p\left(\mathbf{q}_j^n\right)$ and $b_p\left(\mathbf{q}_j^n\right)$ denotes the pth eigenvalue of the Jacobian matrices $\frac{\partial \mathbf{f}(\mathbf{v})}{\partial \mathbf{v}}$ and $\frac{\partial \mathbf{g}(\mathbf{v})}{\partial \mathbf{v}}$.

Again, the nonlinear CFL condition will be treated as a necessary condition for the convergence of nonlinear difference schemes to approximate the solution to nonlinear hyperbolic systems. In the following work, it will be assumed that a particular (algorithm dependent) CFL condition is satisfied.

In two space dimensions, an estimate of the total variation of either the exact solution of a hyperbolic system or its approximate solution often fails. For all these reasons, the notion of TVD and TVB schemes is not as well adapted as in the one-dimensional case. However, according to [27] a two-dimensional difference scheme is TVD if $TV\left(\mathbf{q}^{n+1}\right) \le TV\left(\mathbf{q}^n\right)$, where

$$TV\left(\mathbf{q}^m\right) = \sum_{j\in\mathbb{Z}}\sum_{k\in\mathbb{Z}}\left[\Delta x\left\|\mathbf{q}_{j+1,k}^m - \mathbf{q}_{j,k}^m\right\| + \Delta y\left\|\mathbf{q}_{j,k+1}^m - \mathbf{q}_{j,k}^m\right\|\right] \tag{3.17}$$

and $\|\cdot\|$ denotes the usual $\mathbb{R}^P$ norm.

The development of numerical schemes for the solution approximation to two-dimensional conservation laws is basically the same as for one-dimensional ones. The sliding cell average is calculated by

$$\bar{\mathbf{q}} \;=\; \frac{1}{I_x \times I_y} \int_{I_x} \int_{I_y} \mathbf{q}\,(\xi, \eta, t)\, d\xi d\eta \;, \tag{3.18}$$

where $I_x = \{\xi : 0 \leq \xi - x \leq \Delta x\}$ and $I_y = \{\eta : 0 \leq \eta - y \leq \Delta y\}$ (central idea) or $I_x = \left\{\xi : |\xi - x| \leq \frac{\Delta x}{2}\right\}$ and $I_y = \left\{\eta : |\eta - y| \leq \frac{\Delta y}{2}\right\}$ (upwind idea). Just as in the one-dimensional case, the solution is approximated by a polynomial ansatz

$$\tilde{\mathbf{q}}\,(x, y, t^n) \;\approx\; \sum_{j,k} \left[\mathbf{p}_j + \mathbf{u}_k\right] \chi_{j,k}\,(x, y)\,, \tag{3.19}$$

where $\mathbf{p}_j$ and $\mathbf{u}_k$ denote, in general polynomials in $\bar{\mathbf{q}}^n_{j,k} \approx \bar{\mathbf{q}}\,(x_j, y_k, t^n)$ and reconstructed derivatives $\frac{\partial^m \mathbf{q}}{\partial x^m}$ and $\frac{\partial^m \mathbf{q}}{\partial y^m}$ up to finite order m. Again, the order of the scheme depends on the maximum order of spatial derivatives selected in (3.19). Similar to the one-dimensional case, the term $\chi_{j,k}\,(x, y)$ denotes an indicator function, given by $\chi_{j,k}\,(x, y) = \mathbf{1}_{\left[x_j - \frac{\Delta x}{2}, x_j + \frac{\Delta x}{2}\right] \times \left[y_k - \frac{\Delta y}{2}, y_k + \frac{\Delta y}{2}\right]}$, where $\mathbf{1}_{[a,b]\times[c,d]} = 1$ in $[a, b] \times [c, d]$ and 0 elsewhere. Starting from the approximations (3.18), (3.19), the integral form (2.38) can be used to determine how the cell average varies with time. Out of this information a numerical scheme based on numerical approximations to the fluxes at each cell edge can be developed. Again, various approaches can be found in the literature [17].

3.2 Numerical Schemes

In this section a description of the semi-discrete central scheme used in this research is given. Semi-discrete schemes differ from the schemes above in a way that they are only discretized in space. The evolution in time is done separately by some ODE solver.

The scheme described in this section was proposed by Kurganov and Tadmor [14] and provides a high-resolution solution for hyperbolic conservation laws. It enjoys

the major advantages of central schemes over upwind ones: first, no Riemann solvers are involved, and second - as a result of being Riemann solver free - its realization and generalization for complicated multidimensional systems is considerably simpler than in the upwind case [14]. Riemann solver free solution schemes are also called black box solvers, because the algorithm is independent of the eigenstructure of the system under consideration, i.e. no characteristic decomposition is necessary.

In general, semi-discrete formulations are very important for solving "real", practical problems associated with multidimensional systems. Semi-discrete schemes are especially effective when they combine high-resolution, nonoscillatory spatial discretization with high-order, large stepsize ODE solvers for their time evolution.

For other schemes, such as fully discrete methods and upwind schemes, the author refers to the literature [10], [17].

3.2.1 One-Dimesnional Semi-Discrete Central Scheme

In the case of one-dimensional central schemes, the solution is averaged by integrating (3.1) over the rectangle $[x_j, x_{j+1}] \times [t^n, t^{n+1}]$ which yields to

$$\bar{\mathbf{q}}_{j+\frac{1}{2}}^{n+1} = \bar{\mathbf{q}}_{j+\frac{1}{2}}^{n} - \frac{1}{\Delta x} \int_{t^n}^{t^{n+1}} \left[\mathbf{f}\left(\mathbf{q}\left(x_{j+1}, \tau\right)\right) - \mathbf{f}\left(\mathbf{q}\left(x_j, \tau\right)\right) \right] d\tau. \tag{3.20}$$

Equation (3.20) illustrates the character of central schemes. The averages are integrated over the entire Riemann fan (discontinuities are located at $x_{j\pm\frac{1}{2}}$ by equation (3.8)) so that the corresponding fluxes are evaluated at the smooth centers of the cells, which is shown in Figure 3.2.

Approximating the flux with the numerical flux and letting $\Delta t \to 0$, (3.20) gives the semi-discrete central scheme proposed by Kurganov and Tadmor [14]. This scheme is second order and is given by

$$\frac{d}{dt}\mathbf{q}_j\left(t\right) = -\frac{\mathbf{F}_{j+\frac{1}{2}}\left(t\right) - \mathbf{F}_{j-\frac{1}{2}}\left(t\right)}{\Delta x}, \tag{3.21}$$

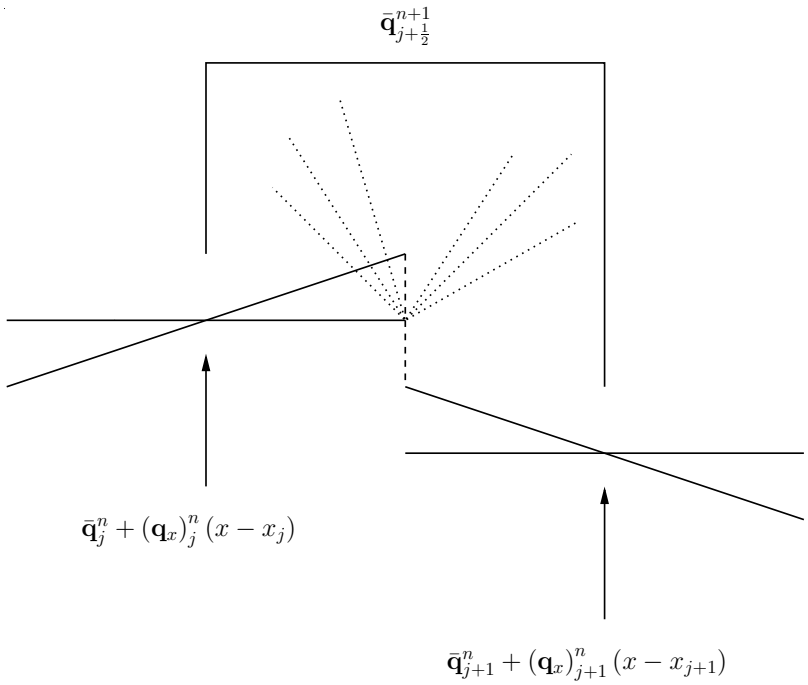

Figure 3.2: Central differencing approach - staggered integration over the local Riemann fan.

where the numerical flux function is defined by

$$\mathbf{F}_{j+\frac{1}{2}}(t) = \frac{\mathbf{f}\left(\mathbf{q}_{j+\frac{1}{2}}^{+}(t)\right) + \mathbf{f}\left(\mathbf{q}_{j+\frac{1}{2}}^{-}(t)\right)}{2} - \frac{a_{j+\frac{1}{2}}(t)}{2}\left[\mathbf{q}_{j+\frac{1}{2}}^{+}(t) - \mathbf{q}_{j+\frac{1}{2}}^{-}(t)\right] \quad (3.22)$$

with the local speed of propagation

$$a_{j+\frac{1}{2}}(t) = \max\left\{\rho\left(\frac{\partial \mathbf{f}}{\partial \mathbf{v}}\left(\mathbf{q}_{j+\frac{1}{2}}^{+}(t)\right)\right), \rho\left(\frac{\partial \mathbf{f}}{\partial \mathbf{v}}\left(\mathbf{q}_{j+\frac{1}{2}}^{-}(t)\right)\right)\right\}, \quad (3.23)$$

where the intermediate values are given by (see Figure 3.2)

$$\mathbf{q}_{j+\frac{1}{2}}^{+}(t) = \mathbf{q}_{j+1}(t) - \frac{\Delta x}{2}(\mathbf{q}_x)_{j+1}(t), \quad \mathbf{q}_{j+\frac{1}{2}}^{-}(t) = \mathbf{q}_j(t) + \frac{\Delta x}{2}(\mathbf{q}_x)_j(t) \quad (3.24)$$

and ρ denotes the spectral radius of the Jacobian matrix evaluated at the specified values. The derivatives $\mathbf{q}_x$ are determined (componentwise) by a slope limiting method, i.e. at the Θ-dependent family of minmod-like limiters [14]

$$(\mathbf{q}_x)_j(t) = \text{minmod}\left(\Theta\frac{\mathbf{q}_j(t) - \mathbf{q}_{j-1}(t)}{\Delta x}, \frac{\mathbf{q}_{j+1}(t) - \mathbf{q}_{j-1}(t)}{2\Delta x}, \Theta\frac{\mathbf{q}_{j+1}(t) - \mathbf{q}_j(t)}{\Delta x}\right), \quad (3.25)$$

where $1 \leq \Theta \leq 2$, together with the multivariable minmod function

$$\text{minmod}\left(x_1, x_2, \ldots\right) \;=\; \begin{cases} \min\left\{x_j\right\} & \text{, if } x_j > 0 \;\forall j, \\ \max\left\{x_j\right\} & \text{, if } x_j < 0 \;\forall j, \\ 0 & \text{, otherwise.} \end{cases} \tag{3.26}$$

The introduction of the parameter Θ allows the adjustment of the numerical dissipation, where $\Theta = 1$ ensures a non-oscillatory nature of the approximate solution and $\Theta = 2$ corresponds to the least dissipative limiter [14]. It is recommended [14] to select $\Theta = 2$ for scalar equations and $1.1 \leq \Theta \leq 1.5$ for systems.

In order to obtain convergence of the scheme, the ratio $\lambda = \frac{\Delta t}{\Delta x}$ must be chosen in order to satisfy the CFL condition

$$\lambda a_{j+\frac{1}{2}}\left(t\right) \;\leq\; \frac{1}{2}, \tag{3.27}$$

where $a_{j+\frac{1}{2}}\left(t\right)$ is evaluated by equation (3.23).

The resulting system of ODEs can be solved by any ODE method; in general, the Runge-Kutta time differencing is preferable over the multilevel differencing, since the former enables a straightforward use of variable time steps.

3.2.2 Two-Dimensional Semi-Discrete Central Scheme

The one-dimensional scheme described in section 3.2.1 can be easily extended to two dimensions [14]. Hence, the two-dimensional semi-discrete central scheme can be written in the conservative form

$$\frac{d}{dt}\mathbf{q}_{j,k}\left(t\right) \;=\; -\frac{\mathbf{F}_{j+\frac{1}{2},k}\left(t\right) - \mathbf{F}_{j-\frac{1}{2},k}\left(t\right)}{\Delta x} - \frac{\mathbf{G}_{j,k+\frac{1}{2}}\left(t\right) - \mathbf{G}_{j,k-\frac{1}{2}}\left(t\right)}{\Delta y} \tag{3.28}$$

with the numerical fluxes

$$\mathbf{F}_{j+\frac{1}{2},k}\left(t\right) \;=\; \frac{\mathbf{f}\left(\mathbf{q}^{+}_{j+\frac{1}{2},k}\left(t\right)\right) + \mathbf{f}\left(\mathbf{q}^{-}_{j+\frac{1}{2},k}\left(t\right)\right)}{2} - \frac{a_{j+\frac{1}{2},k}\left(t\right)}{2}\left[\mathbf{q}^{+}_{j+\frac{1}{2},k}\left(t\right) - \mathbf{q}^{-}_{j+\frac{1}{2},k}\left(t\right)\right],$$

$$\mathbf{G}_{j,k+\frac{1}{2}}\left(t\right) \;=\; \frac{\mathbf{g}\left(\mathbf{q}^{+}_{j,k+\frac{1}{2}}\left(t\right)\right) + \mathbf{g}\left(\mathbf{q}^{-}_{j,k+\frac{1}{2}}\left(t\right)\right)}{2} - \frac{b_{j,k+\frac{1}{2}}\left(t\right)}{2}\left[\mathbf{q}^{+}_{j,k+\frac{1}{2}}\left(t\right) - \mathbf{q}^{-}_{j,k+\frac{1}{2}}\left(t\right)\right],$$

(3.29)

which are expressed in terms of the intermediate values

$$\begin{aligned} \mathbf{q}^{\pm}_{j+\frac{1}{2},k}(t) &= \mathbf{q}_{j+1,k}(t) \mp \tfrac{\Delta x}{2}(\mathbf{q}_x)_{j+\frac{1}{2}\pm\frac{1}{2},k}(t), \\ \mathbf{q}^{\pm}_{j,k+\frac{1}{2}}(t) &= \mathbf{q}_{j,k+1}(t) \mp \tfrac{\Delta y}{2}(\mathbf{q}_y)_{j,k+\frac{1}{2}\pm\frac{1}{2}}(t), \end{aligned} \tag{3.30}$$

and the local speeds of propagation

$$\begin{aligned} a_{j+\frac{1}{2},k}(t) &= \max\left\{\rho\left(\tfrac{\partial \mathbf{f}}{\partial \mathbf{v}}\left(\mathbf{q}^{+}_{j+\frac{1}{2},k}(t)\right)\right), \rho\left(\tfrac{\partial \mathbf{f}}{\partial \mathbf{v}}\left(\mathbf{q}^{-}_{j+\frac{1}{2},k}(t)\right)\right)\right\}, \\ b_{j,k+\frac{1}{2}}(t) &= \max\left\{\rho\left(\tfrac{\partial \mathbf{g}}{\partial \mathbf{v}}\left(\mathbf{q}^{+}_{j,k+\frac{1}{2}}(t)\right)\right), \rho\left(\tfrac{\partial \mathbf{g}}{\partial \mathbf{v}}\left(\mathbf{q}^{-}_{j,k+\frac{1}{2}}(t)\right)\right)\right\}. \end{aligned} \tag{3.31}$$

As in the one-dimensional scheme, ρ denotes the spectral radius of the Jacobian matrix evaluated at the specified values and the derivatives $\mathbf{q}_x$ and $\mathbf{q}_y$ are determined (componentwise) by (3.25) and (3.26).

As described in the one-dimensional case, the system of ODEs can be solved by any ODE method. In this research the numerical scheme described above is implemented by using the package CentPack [3]. The system of ODEs is solved via an explicit second order Runge-Kutta method (modified Euler method) [9].

CHAPTER IV

WAVE PROPAGATION IN AN ELASTIC HALF-SPACE

This chapter discusses wave propagation in an elastic half-space under a normal line load source on the surface. Wave propagation is a broad subject, therefore a complete coverage of the subject is beyond the scope of this thesis, so only the concepts needed for this special problem are reviewed here. In order to get a broad overview of elastic wave propagation and the theory of elasticity, the author recommends [2], [11], [12] and [20] to interested readers.

Wave propagation in an elastic half-space generated by a time-harmonic line load applied normal to the surface is a two-dimensional problem. Figure 4.1 shows the normal line load on the surface of the half-space. Two-dimensional, non-dispersive wave propagation is governed by the following second order hyperbolic system of partial differential equations

$$\begin{aligned} \frac{\partial \sigma_{11}}{\partial x} + \frac{\partial \sigma_{12}}{\partial y} &= \rho \frac{\partial^2 u}{\partial t^2}, \\ \frac{\partial \sigma_{12}}{\partial x} + \frac{\partial \sigma_{22}}{\partial y} &= \rho \frac{\partial^2 v}{\partial t^2}, \end{aligned} \tag{4.1}$$

where ρ denotes the density of the material, $u = u\,(x, y, t)$ and $v = v\,(x, y, t)$ denote the displacements into the x- and y-direction, $\sigma_{11} = \sigma_{11}\,(x, y, t)$ and $\sigma_{22} = \sigma_{22}\,(x, y, t)$ denote the normal stresses into the x- and y-direction and $\sigma_{12} = \sigma_{12}\,(x, y, t)$ denotes the shear stress into the x- and y-direction. The boundary conditions for the problem

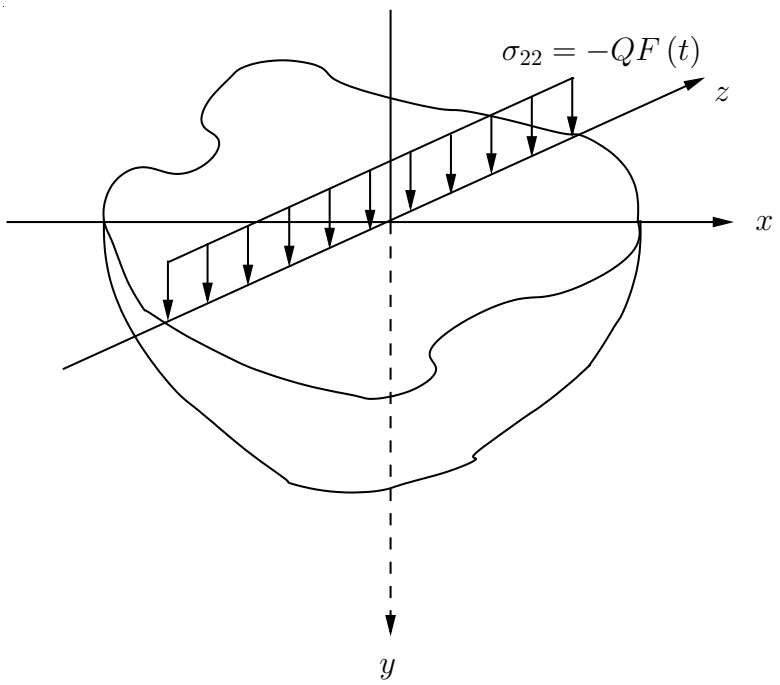

Figure 4.1: Problem of line load applied normal to the surface of an half-space.

depicted in Figure 4.1 are given by

$$\begin{aligned} \sigma_{22}(x,0,t) &= -Q\delta(x)F(t), \\ \sigma_{12}(x,0,t) &= 0. \end{aligned} \tag{4.2}$$

This chapter is arranged as follows: first a linear elastic half-space is investigated. For this linear IBVP, governed by (4.1) and (4.2), it is possible to derive an analytical solution, which is done in the next section. In the second part of this chapter, an elastic half-space with quadratic nonlinearity is considered. So far the author knows, no analytical solution for this nonlinear IBVP, governed by (4.1) and (4.2), exists at the present time. Therefore a numerical study of this demanding problem is done in Chapter 6.

4.1 Original Lamb's Problem

Lamb published one of the most significant contributions in the area of wave propagation in elastic solids [15]. In this work, Lamb investigated the wave motion generated

at the surface and inside the half-space with linear response. The problem of wave propagation due to a time-harmonic line load applied normal to the surface is one of the classical problems in elastic wave propagation and was solved by Lamb in almost complete detail, therefore it is also called "Lamb's Problem". This section considers the original Lamb's Problem and presents the analytical solution to the line load source with arbitrary time signal normal to the surface of a half-space.

4.1.1 Problem Formulation

The governing system of partial differential equations for Lamb's Problem is given by (4.1) with the corresponding boundary conditions (4.2). The half-space is initially at rest, and the initial conditions thus are given by

$$\begin{aligned} u(x,y,0) &= v(x,y,0) = 0, \\ \dot{u}(x,y,0) &= \dot{v}(x,y,0) = 0. \end{aligned} \tag{4.3}$$

In the linear case, the constitutive equations, i.e. the stress-strain relationships are

$$\sigma_{11} = (\lambda + 2\mu)\frac{\partial u}{\partial x} + \lambda\frac{\partial v}{\partial y}, \tag{4.4}$$

$$\sigma_{22} = (\lambda + 2\mu)\frac{\partial v}{\partial y} + \lambda\frac{\partial u}{\partial x}, \tag{4.5}$$

$$\sigma_{12} = \mu\left(\frac{\partial u}{\partial y} + \frac{\partial v}{\partial x}\right), \tag{4.6}$$

where λ and μ are the second-order elastic constants (Lamé coefficients). Together with the constitutive equations (4.4) - (4.6), the equations of motion (4.1) can be written in form of displacement potentials [2], which is shown in Appendix A, and results in

$$\begin{aligned} \frac{\partial^2\phi}{\partial x^2} + \frac{\partial^2\phi}{\partial y^2} &= \frac{1}{c_l^2}\frac{\partial^2\phi}{\partial t^2}, \\ \frac{\partial^2\psi_z}{\partial x^2} + \frac{\partial^2\psi_z}{\partial y^2} &= \frac{1}{c_t^2}\frac{\partial^2\psi_z}{\partial y^2}, \end{aligned} \tag{4.7}$$

where $c_l = \sqrt{\frac{\lambda+2\mu}{\rho}}$ is the velocity of the longitudinal wave and $c_t = \sqrt{\frac{\mu}{\rho}}$ the velocity

of the transverse wave; the scalar potential ϕ and the vector potential $\boldsymbol{\psi}$ are given in this case by

$$\phi = \phi\left(x, y, t\right) \quad \text{and} \quad \boldsymbol{\psi} = \begin{bmatrix} 0 \\ 0 \\ \psi_z\left(x, y, t\right) \end{bmatrix}. \tag{4.8}$$

The stress-potential relations are given in this case by

$$\sigma_{11} = \frac{\lambda}{c_l^2}\ddot{\phi} + 2\mu\left(\frac{\partial^2\phi}{\partial x^2} + \frac{\partial^2\psi_z}{\partial x \partial y}\right), \tag{4.9}$$

$$\sigma_{22} = \frac{\lambda}{c_l^2}\ddot{\phi} + 2\mu\left(\frac{\partial^2\phi}{\partial y^2} - \frac{\partial^2\psi_z}{\partial x \partial y}\right), \tag{4.10}$$

$$\sigma_{12} = \mu\left(-\frac{1}{c_t^2}\ddot{\psi}_z + 2\left(\frac{\partial^2\phi}{\partial x \partial y} + \frac{\partial^2\psi_z}{\partial y^2}\right)\right), \tag{4.11}$$

which is also shown in Appendix A. The initial conditions (4.3) in form of displacement potentials are

$$\begin{aligned} &\phi\left(x, y, 0\right) = \psi_z\left(x, y, 0\right) = 0, \\ &\dot{\phi}\left(x, y, 0\right) = \dot{\psi}_z\left(x, y, 0\right) = 0. \end{aligned} \tag{4.12}$$

The solution to the problem above is obtained by applying integral transform methods to (4.7) and follows generally the one given in [20].

4.1.2 Integral Transforms

In this section, first the Laplace transform is applied to (4.7) and then to the resulting equation the Fourier transform is applied. The Laplace transform and its inverse one are given by [5]

$$\bar{f}\left(p\right) = \int_0^\infty f\left(t\right) e^{-pt} dt \quad \text{and} \quad f\left(t\right) = \frac{1}{2\pi i}\int_{a-i\infty}^{a+i\infty} \bar{f}\left(p\right) e^{pt} dp, \tag{4.13}$$

the Fourier transform and its inverse one can be written as [5]

$$\hat{f}\left(\xi\right) = \int_{-\infty}^{\infty} f\left(x\right) e^{-i\xi t} dt \quad \text{and} \quad f\left(x\right) = \frac{1}{2\pi}\int_{-\infty}^{\infty} \hat{f}\left(\xi\right) e^{i\xi t} d\xi. \tag{4.14}$$

Applying the Laplace transform (4.13) with respect to t to (4.7) with the initial conditions (4.12) yields

$$\begin{aligned} \frac{\partial^2 \bar{\phi}}{\partial x^2} + \frac{\partial^2 \bar{\phi}}{\partial y^2} &= \frac{p^2}{c_l^2}\bar{\phi}, \\ \frac{\partial^2 \bar{\psi}_z}{\partial x^2} + \frac{\partial^2 \bar{\psi}_z}{\partial y^2} &= \frac{p^2}{c_t^2}\bar{\psi}_z, \end{aligned} \tag{4.15}$$

where $\bar{\phi} = \bar{\phi}(x, y, p)$ and $\bar{\psi}_z = \bar{\psi}_z(x, y, p)$. Executing the Fourier transform (4.14) with respect to x to (4.15) results in

$$\begin{aligned} \frac{\partial^2 \hat{\bar{\phi}}}{\partial y^2} - \underbrace{\left(\frac{p^2}{c_l^2} + \xi^2\right)}_{=\alpha_l^2} \hat{\bar{\phi}} &= 0, \\ \frac{\partial^2 \hat{\bar{\psi}}_z}{\partial y^2} - \underbrace{\left(\frac{p^2}{c_t^2} + \xi^2\right)}_{=\alpha_t^2} \hat{\bar{\psi}}_z &= 0, \end{aligned} \tag{4.16}$$

where $\hat{\bar{\phi}} = \hat{\bar{\phi}}(\xi, y, p)$ and $\hat{\bar{\psi}}_z = \hat{\bar{\psi}}_z(\xi, y, p)$; solutions of (4.16) are of the form

$$\begin{aligned} \hat{\bar{\phi}}(\xi, y, p) &= A(\xi, p)\, e^{-\alpha_l y} + C(\xi, p)\, e^{\alpha_l y}, \\ \hat{\bar{\psi}}_z(\xi, y, p) &= B(\xi, p)\, e^{-\alpha_t y} + D(\xi, p)\, e^{\alpha_t y}. \end{aligned} \tag{4.17}$$

Now (4.17) must vanish for $y \to \infty$ by definition of the Fourier transform [5]. Hence, since ξ is real by definition [5] and one can consider p as real and positive [20], it is possible to choose

$$\Re\{\alpha_l\} \geq 0 \quad \text{and} \quad \Re\{\alpha_t\} \geq 0, \tag{4.18}$$

and then require C and D to vanish. Therefore (4.17) reduces to

$$\begin{aligned} \hat{\bar{\phi}}(\xi, y, p) &= A(\xi, p)\, e^{-\alpha_l y}, \\ \hat{\bar{\psi}}_z(\xi, y, p) &= B(\xi, p)\, e^{-\alpha_t y}. \end{aligned} \tag{4.19}$$

These equations have to satisfy the boundary conditions (4.2). Applying the Laplace transform (4.13) to the stress-potentials (4.10) and (4.11), and then to this, the

Fourier transform (4.14) yields

$$\begin{aligned}
\hat{\bar{\sigma}}_{22}(\xi,y,p) &= \lambda\frac{p^2}{c_l^2}\hat{\bar{\phi}}+2\mu\left(\frac{\partial^2\hat{\bar{\phi}}}{\partial y^2}-i\xi\frac{\partial\hat{\bar{\psi}}_z}{\partial y}\right),\\
\hat{\bar{\sigma}}_{12}(\xi,y,p) &= \mu\left[-\frac{p^2}{c_t^2}\hat{\bar{\psi}}_z+2\left(i\xi\frac{\partial\hat{\bar{\phi}}}{\partial y}+\frac{\partial^2\hat{\bar{\psi}}_z}{\partial y^2}\right)\right].
\end{aligned} \tag{4.20}$$

Substitute (4.19) into (4.20) yields together with the boundary conditions (4.2) to the following two algebraic equations

$$\begin{aligned}
\hat{\bar{\sigma}}_{22}(\xi,0,p) &= \lambda\frac{p^2}{c_l^2}A+2\mu\left(\alpha_l^2A+i\xi\alpha_tB\right) \quad \stackrel{!}{=} \quad -Q\bar{F}(p),\\
\hat{\bar{\sigma}}_{12}(\xi,0,p) &= \mu\left[-2i\xi\alpha_lA+2\alpha_t^2B-\frac{p^2}{c_t^2}B\right] \quad \stackrel{!}{=} \quad 0,
\end{aligned} \tag{4.21}$$

which can be rewritten in matrix form as

$$\begin{bmatrix} \frac{p^2}{c_t^2}+2\xi^2 & 2i\xi\alpha_t \\ -2i\xi\alpha_l & \frac{p^2}{c_t^2}+2\xi^2 \end{bmatrix}\begin{bmatrix} A \\ B \end{bmatrix} = \begin{bmatrix} -\frac{Q\bar{F}(p)}{\mu} \\ 0 \end{bmatrix}. \tag{4.22}$$

Equation (4.22) is a linear system of equations and can be solved by standard methods resulting in

$$\begin{aligned}
A(\xi,p) &= -\frac{Q\bar{F}(p)}{\mu}\frac{\frac{p^2}{c_t^2}+2\xi^2}{R(\xi,p)},\\
B(\xi,p) &= -\frac{Q\bar{F}(p)}{\mu}\frac{2i\alpha_l\xi}{R(\xi,p)},
\end{aligned} \tag{4.23}$$

where

$$R(\xi,p) = \left(\frac{p^2}{c_t^2}+2\xi^2\right)^2-4\alpha_l\alpha_t\xi^2. \tag{4.24}$$

Substitute α_l and α_t into (4.24) yields

$$R(\xi,p) = \xi^4\left[\left(\frac{p^2}{c_t^2\xi^2}+2\right)^2-4\left(1+\frac{p^2}{\xi^2c_l^2}\right)^{\frac{1}{2}}\left(1+\frac{p^2}{\xi^2c_t^2}\right)^{\frac{1}{2}}\right]. \tag{4.25}$$

By comparison of (4.25) with the Rayleigh equation

$$\left(2-\frac{c^2}{c_t^2}\right)^2-4\left(1-\frac{c^2}{c_l^2}\right)^{\frac{1}{2}}\left(1-\frac{c^2}{c_t^2}\right)^{\frac{1}{2}} \;=\; 0, \tag{4.26}$$

which has zeros at $c=\pm c_r$ [2], where c_r denotes the velocity of the Rayleigh wave, it can be easily seen that (4.25) has zeros at

$$\frac{p^2}{\xi^2} \;=\; -c_r^2. \tag{4.27}$$

Substitution of (4.23) into (4.19) completes the definition of the transformed solutions of the potentials.

The displacements $u(x,y,t)$ and $v(x,y,t)$ can be obtained from the potentials [2] by

$$\begin{aligned} u &= \frac{\partial\phi}{\partial x}+\frac{\partial\psi_z}{\partial y}, \\ v &= \frac{\partial\phi}{\partial y}-\frac{\partial\psi_z}{\partial x}. \end{aligned} \tag{4.28}$$

Applying the Laplace transform (4.13) and the Fourier transform (4.14) to (4.28) results in

$$\begin{aligned} \hat{\bar{u}} &= i\xi\hat{\bar{\phi}}+\frac{\partial\hat{\bar{\psi}}_z}{\partial y}, \\ \hat{\bar{v}} &= \frac{\partial\hat{\bar{\phi}}}{\partial y}-i\xi\hat{\bar{\psi}}_z \end{aligned} \tag{4.29}$$

and substituting $\hat{\bar{\phi}}(\xi,y,p)$ and $\hat{\bar{\psi}}_z(\xi,y,p)$ by their solution (4.19) yields

$$\begin{aligned} \hat{\bar{u}}(\xi,y,p) &= i\xi A(\xi,p)\,e^{-\alpha_l y}-\alpha_t B(\xi,p)\,e^{-\alpha_t y}, \\ \hat{\bar{v}}(\xi,y,p) &= -A(\xi,p)\,\alpha_l e^{-\alpha_l y}-i\xi B(\xi,p)\,e^{-\alpha_t y} \end{aligned} \tag{4.30}$$

with $A(\xi,p)$ and $B(\xi,p)$ given by (4.23).

Now the inverse Laplace transform and the inverse Fourier transform have to be applied to (4.30).

4.1.3 Inverse Integral Transforms

To get the solution in the real x- and time-domain one has to apply the inverse integral transforms to the double transformed solution (4.30) - which is done in the following. Applying the inverse Fourier transform (4.14) to (4.30) yields

$$\bar{u}(x,y,p) = \frac{1}{2\pi}\int_{-\infty}^{\infty}\left[i\xi A(\xi,p)\,e^{-\alpha_l y}e^{i\xi x} - \alpha_t B(\xi,p)\,e^{-\alpha_t y}e^{i\xi x}\right]d\xi, \tag{4.31}$$

$$\bar{v}(x,y,p) = \frac{1}{2\pi}\int_{-\infty}^{\infty}\left[-A(\xi,p)\,\alpha_l e^{-\alpha_l y}e^{i\xi x} - i\xi B(\xi,p)\,e^{-\alpha_t y}e^{i\xi x}\right]d\xi. \tag{4.32}$$

The next step in the solution process is the inversion of the Laplace transforms $\bar{u}$ and $\bar{v}$ in (4.31) and (4.32). This inversion is carried out by the Cagniard-deHoop method, which is described in [2]. The use of the Laplace inversion integral (4.13) is not very suitable to this problem, because one would have a double inversion integral involving branch points of α_l and α_t in the p-plane [20].

By substituting $c_l = \frac{1}{s_l}$ and $c_t = \frac{1}{s_t}$ and introducing the real variable $\eta = \frac{\xi}{p}$, which is possible since p is real and positive, into the integrals (4.31) and (4.32), that is, with

$$\begin{aligned} &\xi = \eta p, && d\xi = p\,d\eta, \\ &\alpha_l = p\left(s_l^2+\eta^2\right)^{\frac{1}{2}}, && \alpha_t = p\left(s_t^2+\eta^2\right)^{\frac{1}{2}}, \end{aligned} \tag{4.33}$$

these integrals become

$$\begin{bmatrix}\bar{u}(x,y,p)\\ \bar{v}(x,y,p)\end{bmatrix} = \frac{Q\bar{F}(p)}{2\pi\mu}\int_{-\infty}^{\infty}\left(\begin{bmatrix}f_l(\eta)\\ h_l(\eta)\end{bmatrix}e^{-pg_l(\eta)} + \begin{bmatrix}f_t(\eta)\\ h_t(\eta)\end{bmatrix}e^{-pg_t(\eta)}\right)d\eta, \tag{4.34}$$

where

$$\begin{aligned} g_l(\eta) &= \left(\eta^2+s_l^2\right)^{\frac{1}{2}}y - i\eta x & g_t(\eta) &= \left(\eta^2+s_t^2\right)^{\frac{1}{2}}y - i\eta x \\ f_l(\eta) &= -\frac{i\eta}{\tilde{R}(\eta)}\left(s_t^2+2\eta^2\right) & f_t(\eta) &= \frac{2i\eta}{\tilde{R}(\eta)}\left(\eta^2+s_t^2\right)^{\frac{1}{2}}\left(\eta^2+s_l^2\right)^{\frac{1}{2}} \\ h_l(\eta) &= \left(\eta^2+s_l^2\right)^{\frac{1}{2}}\frac{s_t^2+2\eta^2}{\tilde{R}(\eta)} & h_t(\eta) &= -\frac{2\eta^2}{\tilde{R}(\eta)}\left(\eta^2+s_l^2\right)^{\frac{1}{2}}, \end{aligned}$$

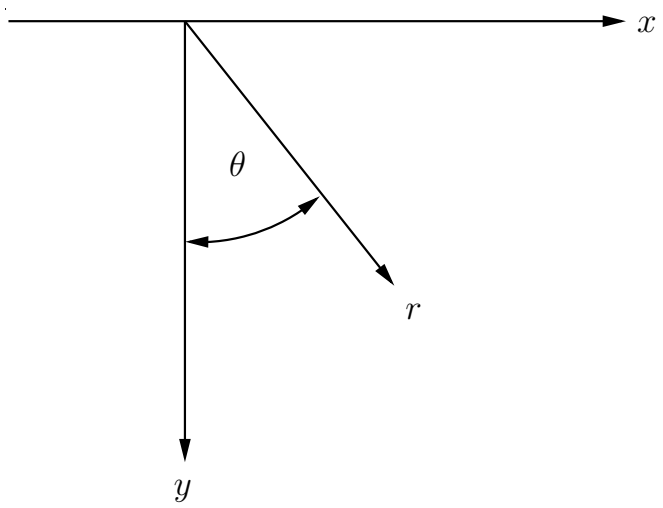

Figure 4.2: Relation between cartesian and polar coordinates.

and

$$\tilde{R}(\eta) \;=\; \left(s_t^2+2\eta^2\right)^2-4\eta^2\left(\eta^2+s_l^2\right)^{\frac{1}{2}}\left(\eta^2+s_t^2\right)^{\frac{1}{2}},$$

where the "sub l and t" terms in the integrals of (4.34) are associated with the longitudinal and transverse parts of the displacements, respectively.

For the further steps in the derivation of the solution it is easier to use polar coordinates. Figure 4.2 shows that the relation between the Cartesian and Polar coordinates is given by

$$x = r\sin\theta \quad \text{and} \quad y = r\cos\theta, \tag{4.35}$$

with $0 \le r \le \infty$ and $-\frac{\pi}{2} \le \theta \le \frac{\pi}{2}$. In the following only the area for $0 \le \theta \le \frac{\pi}{2}$ is considered, since the displacements are symmetric to $x = 0$.

The basic idea in the Cagniard-deHoop inversion of integrals like (4.34) is to let $g(\eta) = t$, which is real and positive. This deforms the path of integration off the real axis of η. Clearly then, consideration must be given to the character of f, g and h in (4.34) in the η-plane, since the integration path must not cross any poles or branch points for $t \to \infty$. The functions f and h have branch points at $\eta = \pm is_l,\ \pm is_t$, and simple poles at $\eta = \pm is_r$. The function g has branch points at $\eta = \pm is_l$ and

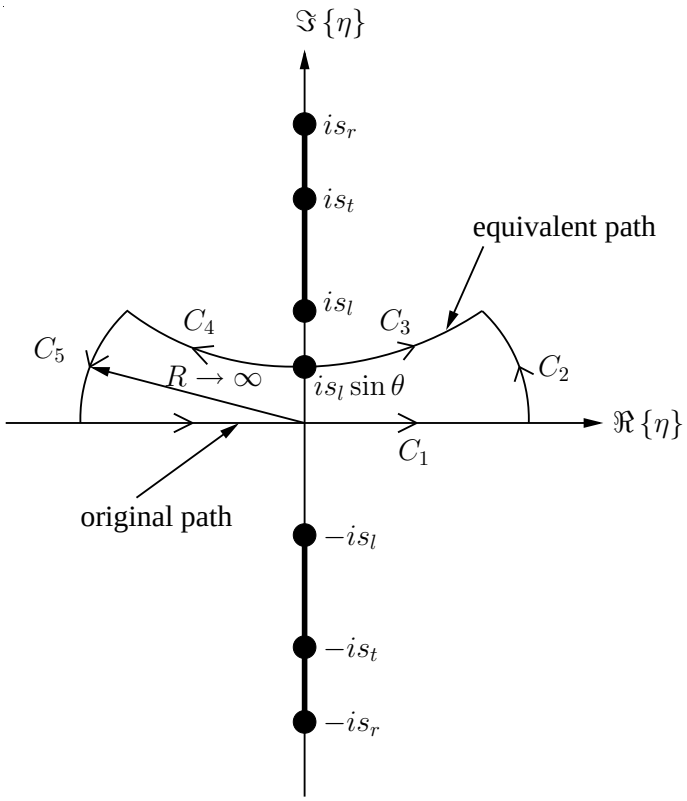

Figure 4.3: Equivalent path of integration in Cagniard-deHoop method.

$\eta = \pm is_t$.

Applying Jordan's Lemma [5] to the integration of the integrals in (4.34) over the completed path shown in Figure 4.3, imposing $y \geq 0$, and $x \geq 0$, shows that the integrals over C_2 and C_5 vanish. Hence, the integrals in (4.34) (along the original path, which is the real axis) are equivalent to those on any path in the upper half plane, from $-\infty$ in the second quadrant to ∞ in the first quadrant, passing between $\eta = 0$ and $\eta = is_l$, as shown in Figure 4.3. Imposing $g_l(\eta) = t$, leads to an upper half plane contour of the type of the equivalent path in Figure 4.3, given by

$$\eta = \eta_{l\pm}(t) = \pm\left(\frac{t^2}{r^2} - s_l^2\right)^{\frac{1}{2}} \cos\theta + \frac{it}{r}\sin\theta, \quad \frac{t}{r} \geq s_l, \tag{4.36}$$

which is a branch of a hyperbola lying in the upper half η-plane [20] with asymptotes $\frac{\Im\{\eta\}}{\Re\{\eta\}} = \pm\tan\theta$. The earliest time, when (4.36) is valid is $t = rs_l$, which gives $\eta = is_l \sin\theta$, the vertex of the branch. As t grows, the real parts ($\pm$), and the positive

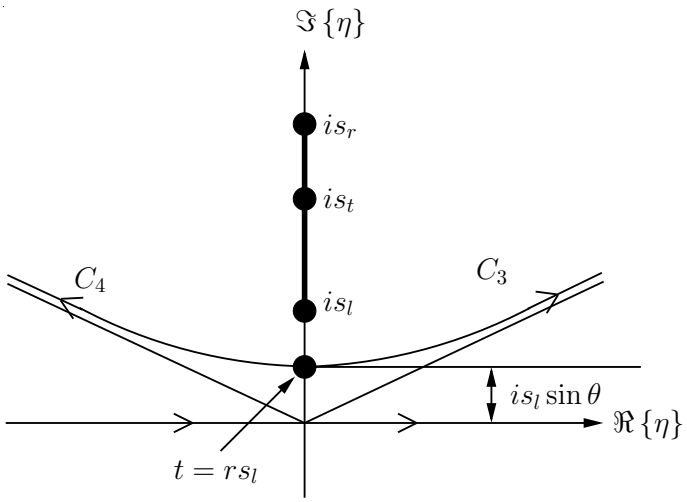

Figure 4.4: The Cagniard path corresponding to the longitudinal waves.

imaginary part grow, until $t \to \infty$, $\frac{\Im\{\eta\}}{\Re\{\eta\}} \to \pm \tan\theta$., i.e. (4.36) tends to its asymptotes. Figure 4.4 provides a sketch of this Cagniard path. Imposing $0 \leq \theta < \frac{\pi}{2}$, the Cagniard path does not intersect the branch cut shown in Figure 4.4. Integrating the g_l integrals, in (4.34), over the path (4.36), $-C_3 + C_4$ in Figure 4.4, and using the fact that

$$\int_{C_k} = -\left(\int_{C_l}\right)^*, \tag{4.37}$$

if $C_k = -C_l^*$ [20], yields

$$\begin{bmatrix} \bar{u}_l \\ \bar{v}_l \end{bmatrix} = \frac{Q\bar{F}(p)}{\pi\mu} \int_{rs_l}^{\infty} \Re\left\{ \begin{bmatrix} f_l(\eta_{l+}(t)) \\ h_l(\eta_{l+}(t)) \end{bmatrix} \frac{d\eta_{l+}}{dt} \right\} e^{-pt}\, dt. \tag{4.38}$$

The process is basically the same for the g_t integrals in (4.34), therefore set $g_t(\eta) = t$ to gain the path of integration. Hence, the new path of integration is found by

$$\eta = \eta_{t\pm}(t) = \pm\left(\frac{t^2}{r^2} - s_t^2\right)^{\frac{1}{2}} \cos\theta + \frac{it}{r}\sin\theta, \quad \frac{t}{r} \geq s_t. \tag{4.39}$$

Equation (4.39) is again a branch of hyperbola in the upper half η-plane, with asymptotes $\frac{\Im\{\eta\}}{\Re\{\eta\}} = \pm\tan\theta$ [20]. The initial time is now $t = rs_t$, which gives $\eta = is_t \sin\theta$ as the vertex of the branch. Hence, provided $s_t \sin\theta < s_l$, (4.39) does not intersect the

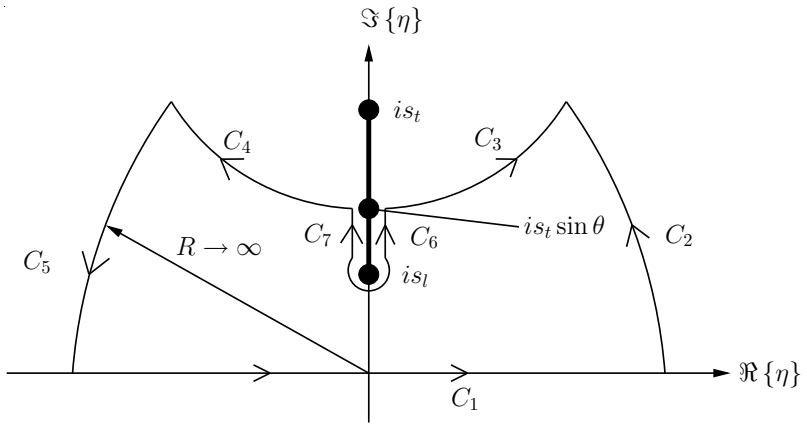

Figure 4.5: The Cagniard path corresponding to the transverse waves with supplemental path H.

cut, and the situation is just the same as in the g_l integrals, i.e. Figure 4.4 applies again, with the simple changes just mentioned. Therefore, integrating the g_t integrals, in (4.34), over the path (4.39),$-C_3 + C_4$ in Figure 4.4, and using again (4.37) yields,

$$\begin{bmatrix} \bar{u}_t \\ \bar{v}_t \end{bmatrix} = \frac{Q\bar{F}(p)}{\pi\mu} \int_{rs_t}^{\infty} \Re\left\{ \begin{bmatrix} f_t(\eta_{t+}(t)) \\ h_t(\eta_{t+}(t)) \end{bmatrix} \frac{d\eta_{t+}}{dt} \right\} e^{-pt}\, dt, \tag{4.40}$$

for $s_t \sin\theta < s_l$. When $s_l < s_t \sin\theta < s_t$, or equivalently $\sin^{-1}\left(\frac{s_l}{s_t}\right) \leq \theta < \frac{\pi}{2}$ the Cagniard contour (4.39) will intersect the cut, so this contour must be supplemented by a path, say $-C_6 + C_7$, that approaches but circumvents this cut and joins the Cagniard contour C_3, C_4 as shown in Figure 4.5.

The lineal paths of $-C_6 + C_7$, along the cut, meet the contour C_3, C_4 at $is_t \sin\theta$, corresponding to the time $t = rs_t$, as Figure 4.5 shows. Now along these paths, η becomes positive imaginary in the limit (as the cut is approached). Further, $|\eta|$ decays along these paths from $\eta = is_t \sin\theta$ toward the ends at the branch point $\eta = is_l$. It follows from (4.39) that these paths are represented by

$$\eta_{tl\pm}(t) = i\left[-\left(s_t^2 - \frac{t^2}{r^2} \right)^{\frac{1}{2}} \cos\theta + \frac{t}{r} \sin\theta \right], \quad t_{tl} \leq t \leq rs_t, \tag{4.41}$$

where

$$t_{tl} \;=\; r\left[s_l \sin\theta + \left(s_t^2 - s_l^2\right)^{\frac{1}{2}} \cos\theta\right], \tag{4.42}$$

is the minimum time, when the branch point is_l is reached. The circular path H in Figure 4.5 can be expressed as $\eta = is_l + \Delta e^{i\delta}$. In [20] it is shown that the possible contribution of the circular path H will vanish for the limit case $\Delta \to 0$. Hence, it follows, again taking into account (4.37) on the lineal paths C_6 and C_7, that this contour yields the further contributions to the Laplace transformed displacements,

$$\begin{bmatrix} \bar{u}_{tl} \\ \bar{v}_{tl} \end{bmatrix} \;=\; \frac{Q\bar{F}(p)}{\pi\mu} \int_{t_{tl}}^{rs_t} \Re\left\{ \begin{bmatrix} f_t\left(\eta_{tl+}(t)\right) \\ h_t\left(\eta_{tl+}(t)\right) \end{bmatrix} \frac{d\eta_{tl+}}{dt} \right\} e^{-pt}\, dt, \tag{4.43}$$

where η_{tl+} and t_{tl}, are given in (4.41) and (4.42), respectively.

The integrals (4.38), (4.40) and (4.43) are valid in the region $0 < r < \infty$, $0 \le \theta < \frac{\pi}{2}$, where the third integral occurs only for $\sin^{-1}\left(\frac{s_l}{s_t}\right) \le \theta < \frac{\pi}{2}$.

The solution representing the surface response is obtained by evaluating (4.34) at $\theta = \frac{\pi}{2}$, which results in

$$\bar{u}(r, \pi/2, p) \;=\; \frac{Q\bar{F}(p)}{2\pi\mu} \int_{-\infty}^{\infty} \frac{-i\eta\left(s_t^2 + 2\eta^2\right) + 2i\eta\left(\eta^2 + s_t^2\right)^{\frac{1}{2}}\left(\eta^2 + s_l^2\right)^{\frac{1}{2}}}{\tilde{R}(\eta)} e^{ip\eta r}\, d\eta, \tag{4.44}$$

$$\bar{v}(r, \pi/2, p) \;=\; \frac{Q\bar{F}(p)}{2\pi\mu} \int_{-\infty}^{\infty} \frac{\left(\eta^2 + s_l^2\right)^{\frac{1}{2}} s_t^2}{\tilde{R}(\eta)} e^{ip\eta r}\, d\eta. \tag{4.45}$$

By substituting $\theta = \frac{\pi}{2}$ into (4.36), (4.39) and (4.41), $\eta = \frac{it}{r}$ is obtained as integration path with $rs_l \le t < \infty$, $rs_t \le t < \infty$ and $t_{tl} \le t \le rs_t$, respectively. This integration path for $\theta = \frac{\pi}{2}$ is sketched in Figure 4.6. Again C_2' and C_5' vanish by Jordan's Lemma and the integration over the path $-C_3' + C_4'$ yields

$$\begin{bmatrix} \bar{u}(r, \pi/2, p) \\ \bar{v}(r, \pi/2, p) \end{bmatrix} \;=\; \begin{bmatrix} \bar{u}_l + \bar{u}_t + \bar{u}_{tl} \\ \bar{v}_l + \bar{v}_t + \bar{v}_{tl} \end{bmatrix}_{\theta=\frac{\pi}{2}}. \tag{4.46}$$

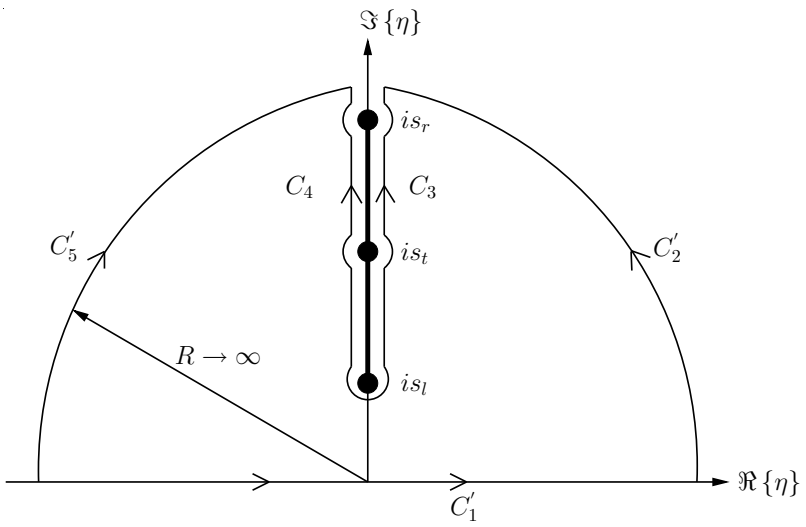

Figure 4.6: The Cagniard path corresponding to the surface solution.

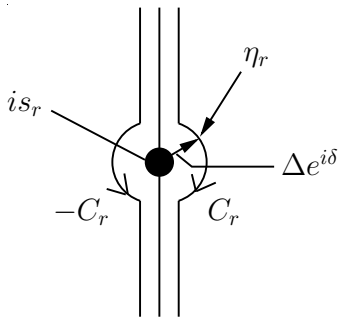

Figure 4.7: Integration around the Rayleigh pole.

The simple pole at $\eta = is_r$ has an additional contribution, which is calculated in the following. Let $\eta = \eta_r = is_r + \Delta e^{i\delta}$, as shown in Figure 4.7. Again the conjugate properties (4.37) can be applied to the resulting integrals. Hence, it follows that

$$\bar{u}\left(r, \pi/2, p\right) = \frac{Q\bar{F}\left(p\right)}{\pi\mu} \lim_{\Delta \to 0} \int_{C_r} \Re\left\{ \frac{-i\eta_r \left(s_t^2 + 2\eta_r^2\right) + 2i\eta_r \left(\eta_r^2 + s_t^2\right)^{\frac{1}{2}} \left(\eta_r^2 + s_l^2\right)^{\frac{1}{2}}}{\tilde{R}\left(\eta_r\right)} e^{ip\eta_r r}\, d\delta \right\}, \tag{4.47}$$

which, noting that near $\eta = is_r$, $\tilde{R}\left(\eta\right) \simeq \Delta e^{i\delta} \tilde{R}'\left(is_r\right)$, where

$$\tilde{R}'\left(is_r\right) = \left[\frac{d\tilde{R}\left(\eta\right)}{d\eta} \right]_{\eta = is_r}, \tag{4.48}$$

reduces to

$$\bar{u}\left(r, \pi/2, p\right) = \bar{u}_r\left(r, p\right) = -\frac{s_t^2 \left(s_t^2 - 2s_r^2\right) Q}{2\mu s_r \left(\frac{\tilde{R}'\left(is_r\right)}{i}\right)} \bar{F}\left(p\right) e^{-prs_r}, \tag{4.49}$$

where $\frac{\tilde{R}'\left(is_r\right)}{i}$ is real [20]. Note that the integrand numerator in (4.44) and (4.45), as $\eta \to is_r$, is real, and the corresponding $\left(\eta^2 + s_l^2\right)^{\frac{1}{2}}$ in (4.45) is imaginary, therefore the pole at is_r has no contribution to $\bar{v}\left(r, \pi/2, p\right)$. Hence, the transformed solution for the surface of the half-space, $\theta = \frac{\pi}{2}$, is given by

$$\bar{u}\left(r, \pi/2, p\right) = \bar{u}_l\left(r, \pi/2, p\right) + \bar{u}_t\left(r, \pi/2, p\right) + \bar{u}_{tl}\left(r, \pi/2, p\right) + \bar{u}_r\left(r, p\right), \tag{4.50}$$

$$\bar{v}\left(r, \pi/2, p\right) = \bar{v}_l\left(r, \pi/2, p\right) + \bar{v}_t\left(r, \pi/2, p\right) + \bar{v}_{tl}\left(r, \pi/2, p\right), \tag{4.51}$$

where the first two integrals in each case (4.38) and (4.40) are Cauchy principal values [20]. The transformed solution for $0 \leq \theta < \frac{\pi}{2}$ is given by (4.38), (4.40) and (4.43)

$$\bar{u}\left(r, \theta, p\right) = \bar{u}_l\left(r, \theta, p\right) + \bar{u}_t\left(r, \theta, p\right) + \bar{u}_{tl}\left(r, \theta, p\right), \tag{4.52}$$

$$\bar{v}\left(r, \theta, p\right) = \bar{v}_l\left(r, \theta, p\right) + \bar{v}_t\left(r, \theta, p\right) + \bar{v}_{tl}\left(r, \theta, p\right). \tag{4.53}$$

To get a closed form solution in the time domain, only the impulse response $F\left(t\right) = \delta\left(t\right)$, so that $\bar{F}\left(p\right) = 1$ is considered in the following. This is no limitation, since the solution for an arbitrary signal $F\left(t\right)$ can be obtained by convolution of the impulse

response with the signal in the time domain. With $\bar{F}(p) = 1$ the transformed "interior" solution (4.52), (4.53) and "surface" solution (4.50), (4.51) are in the form that the inverse Laplace transform [5]

$$L^{-1}\left\{\int_{t_1}^{\infty} e^{-pt} f(t)\, dt\right\} = f(t) H(t - t_1) \tag{4.54}$$

can be applied. For the inverse Laplace transform of (4.49) the following holds

$$L^{-1}\left\{e^{-ap}\right\} = \delta(t - a). \tag{4.55}$$

Therefore the inverse Laplace transform of the different displacement terms, yields

$$\begin{aligned}
u_l(r,\theta,t) &= \frac{Q}{\pi\mu}\Re\left\{f_l(\eta_{l+}(t))\frac{d\eta_{l+}(t)}{dt}\right\} H(t - rs_l), \\
u_t(r,\theta,t) &= \frac{Q}{\pi\mu}\Re\left\{f_t(\eta_{t+}(t))\frac{\eta_{t+}(t)}{dt}\right\} H(t - rs_t), \\
u_{tl}(r,\theta,t) &= \frac{Q}{\pi\mu}\Re\left\{f_t(\eta_{tl+}(t))\frac{d\eta_{tl+}(t)}{dt}\right\} [H(t - t_{tl}) - H(t - rs_t)], \\
u_r(r,t) &= -\frac{s_t^2(s_t^2 - 2s_r^2)Q}{2\mu s_r\left(\frac{\tilde{R}'(is_r)}{i}\right)}\delta(t - rs_r), \\
v_l(r,\theta,t) &= \frac{Q}{\pi\mu}\Re\left\{h_l(\eta_{l+}(t))\frac{d\eta_{l+}(t)}{dt}\right\} H(t - rs_l), \\
v_t(r,\theta,t) &= \frac{Q}{\pi\mu}\Re\left\{h_t(\eta_{t+}(t))\frac{d\eta_{t+}(t)}{dt}\right\} H(t - rs_t), \\
v_{tl}(r,\theta,t) &= \frac{Q}{\pi\mu}\Re\left\{h_t(\eta_{tl+}(t))\frac{d\eta_{tl+}(t)}{dt}\right\} [H(t - t_{tl}) - H(t - rs_t)],
\end{aligned} \tag{4.56}$$

with the terms given in (4.34), (4.36), (4.39), (4.41), (4.42) and (4.48), respectively. Hence, the solution to the original linear Lamb's problem (4.1), (4.2) is

$$\begin{bmatrix} u(r,\theta,t) \\ v(r,\theta,t) \end{bmatrix} = \begin{bmatrix} u_l(r,\theta,t) + u_t(r,\theta,t) + u_{tl}(r,\theta,t) \\ v_l(r,\theta,t) + v_t(r,\theta,t) + v_{tl}(r,\theta,t) \end{bmatrix}, \tag{4.57}$$

for $0 \leq \theta < \frac{\pi}{2}$ and

$$\begin{bmatrix} u(r,\pi/2,t) \\ v(r,\pi/2,t) \end{bmatrix} = \begin{bmatrix} u_l(r,\pi/2,t) + u_t(r,\pi/2,t) + u_{tl}(r,\pi/2,t) + u_r(r,t) \\ v_l(r,\pi/2,t) + u_t(r,\pi/2,t) + u_{tl}(r,\pi/2,t) \end{bmatrix}, \tag{4.58}$$

for $\theta = \frac{\pi}{2}$.

The solution (4.57) and (4.58) for Lamb's problem of the surface normal line load source of delta function time behavior shows that such a source generates four different types of waves that establish the character of the half-space motion [20]. One of these is a circular cylindrical longitudinal wave, the front of which radiates out from the source ($r = 0$) with speed c_l. The second is a circular cylindrical transverse wave, which propagates with speed c_t. The third is a transverse wave, commonly referred to as head wave. This plane fronted head wave occurs only in the region $\beta \leq \theta < \frac{\pi}{2}$, where $\beta = \sin^{-1}\left(\frac{s_l}{s_t}\right)$, traveling with speed c_t along the normal to the front, which makes the angle β with the y-axis. Lastly there is a singular Rayleigh surface wave disturbance which propagates with c_r from the source. This disturbance also occurs in the interior where it is non-singular. Figure 4.8 shows the symmetry of the problem

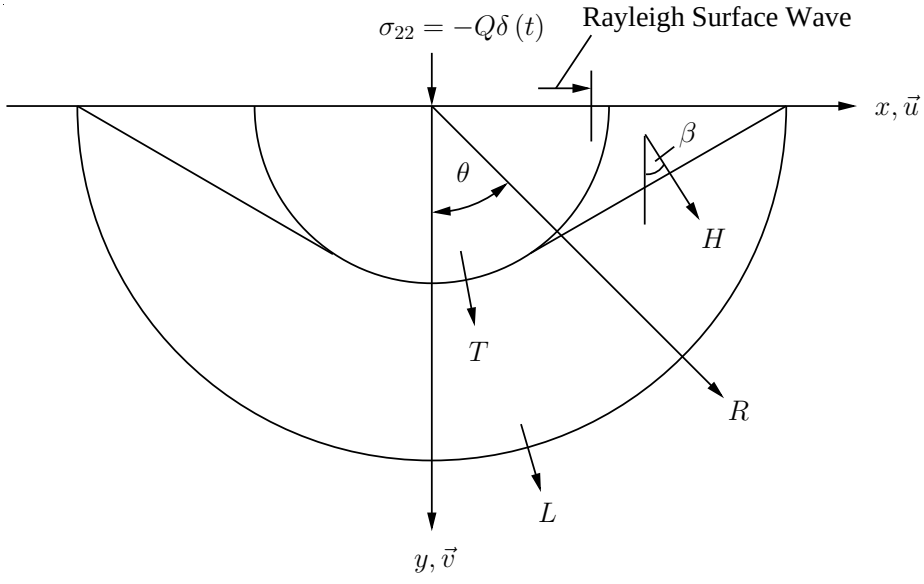

Figure 4.8: The nature of disturbed region of half-space (for fixed time) for surface normal line load source.

with respect to the y-axis and contains a sketch of the waves, for fixed arbitrary time t, showing the parts they play in the solution (4.57), (4.58).

The wave fronts and displacement coefficients at $\theta = 0°$, $30°$, $60°$ are represented in Figure 4.9, 4.10 and 4.11, respectively. Figure 4.12 shows the "surface" solution, $\theta = 90°$, for different values of Poisson's ratio. The delta function singularities in the figure are represented by vertical straight lines.

The results in Figure 4.9, 4.10, 4.11 and 4.12 are consistent with the ones presented by Forrestal [8].

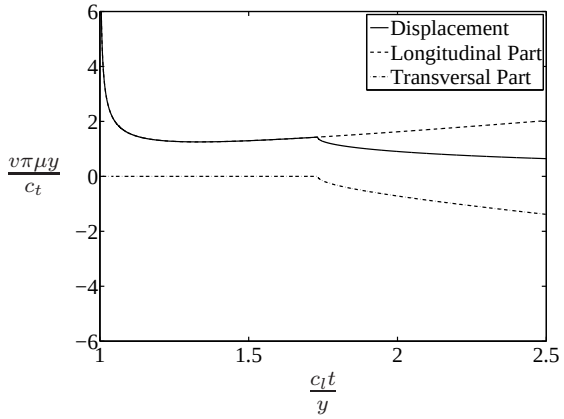

Figure 4.9: Displacement component at $\theta = 0°$.

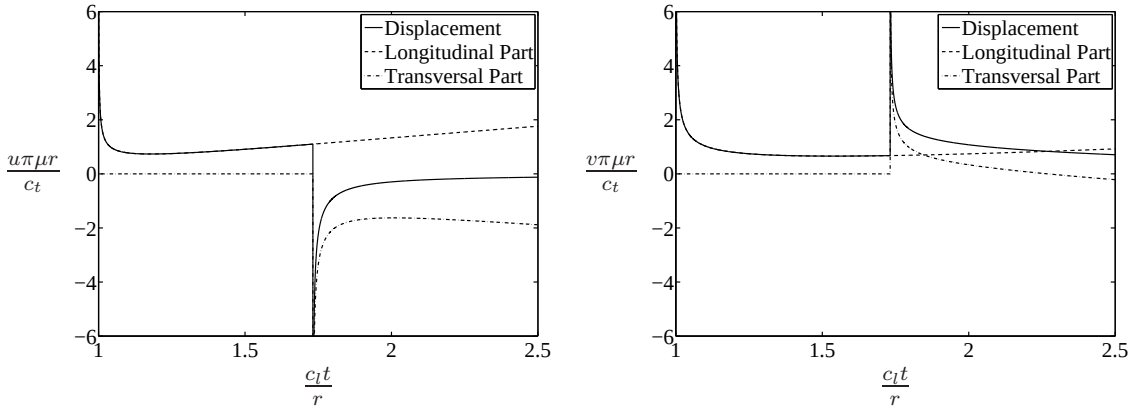

(a) Displacement u (b) Displacement v

Figure 4.10: Displacement components at $\theta = 30°$.

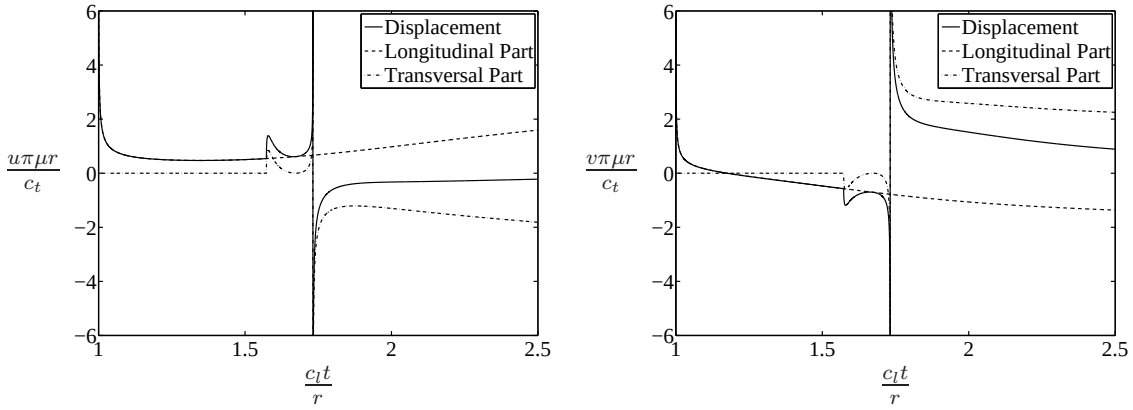

(a) Displacement u (b) Displacement v

Figure 4.11: Displacement components at $\theta = 60°$.

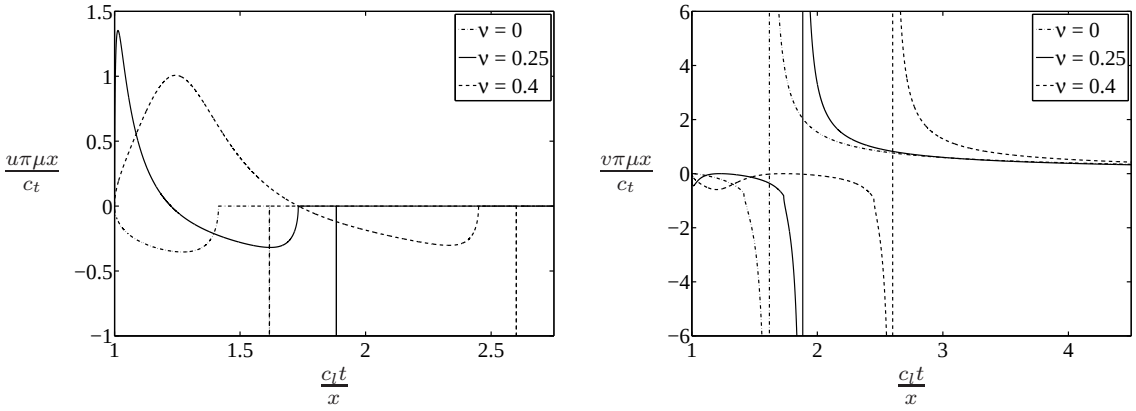

(a) Displacement u (b) Displacement v

Figure 4.12: Surface displacement components produced by a line source.

4.2 Nonlinear Lamb's Problem

In this section, the problem formulation of the IBVP governed by (4.1), (4.2) is presented for an elastic half-space with quadratic nonlinearity. The formulation differs from the one presented in section 4.1.1 in its constitutive equations. The derivation of the constitutive equations used to model the quadratic nonlinearity follows the one presented in [18].

4.2.1 Constitutive Equations with Quadratic Nonlinearity

In general, the stress tensor is given by

$$\sigma_{ij} = \frac{\partial \Gamma}{\partial (u_{i,j})}, \tag{4.59}$$

where Γ is the internal energy density of a homogeneous, elastic solid. Including third-order terms in the strain, the internal energy density may be written

$$\Gamma = \frac{\lambda + 2\mu}{2} I_1^2 - 2\mu I_2 + \frac{l + 2m}{3} I_1^3 - 2m I_1 I_2 + n I_3, \tag{4.60}$$

where λ and μ are again second-order elastic constants; l, m and n are third-order elastic constants (Murnaghan coefficients); and I_1, I_2, I_3 are the three invariants of the strain tensor

$$\begin{aligned} I_1 &= \varepsilon_{ii}, \\ I_2 &= \begin{vmatrix} \varepsilon_{22} & \varepsilon_{23} \\ \varepsilon_{32} & \varepsilon_{33} \end{vmatrix} + \begin{vmatrix} \varepsilon_{33} & \varepsilon_{31} \\ \varepsilon_{13} & \varepsilon_{11} \end{vmatrix} + \begin{vmatrix} \varepsilon_{11} & \varepsilon_{12} \\ \varepsilon_{21} & \varepsilon_{22} \end{vmatrix}, \\ I_3 &= \det \varepsilon_{ij}, \end{aligned} \tag{4.61}$$

where the components of the strain tensor are given by

$$\varepsilon_{ij} = \frac{1}{2} \left(u_{i,j} + u_{j,i} + \underbrace{u_{k,i} u_{k,j}}_{=0} \right). \tag{4.62}$$

In this research only small changes in the displacements are considered, hence the term of the geometrical nonlinearity in the strain tensor is neglected as it was already

done in section 4.1.

Since this research treats a two-dimensional problem, it holds $\varepsilon_{13} = \varepsilon_{23} = \varepsilon_{33} = 0$. Hence, the invariants of the strain tensor (4.61) reduces to

$$\begin{aligned} I_1 &= \varepsilon_{11} + \varepsilon_{22}, \\ I_2 &= \varepsilon_{11}\varepsilon_{22} - \varepsilon_{12}^2, \\ I_3 &= 0, \end{aligned} \tag{4.63}$$

and the internal energy Γ is given by

$$\begin{aligned} \Gamma &= \frac{\lambda + 2\mu}{2} \left(\varepsilon_{11} + \varepsilon_{22}\right)^2 - 2\mu \left(\varepsilon_{11}\varepsilon_{22} - \varepsilon_{12}^2\right) + \frac{l + 2m}{3} \left(\varepsilon_{11} + \varepsilon_{22}\right)^3 \\ &\quad -2m \left(\varepsilon_{11} + \varepsilon_{22}\right) \left(\varepsilon_{11}\varepsilon_{22} - \varepsilon_{12}^2\right). \end{aligned} \tag{4.64}$$

Substituting (4.64) into (4.59) yields the constitutive equations for an elastic half-space with quadratic nonlinearity

$$\begin{aligned} \sigma_{11} &= (\lambda + 2\mu) \frac{\partial u}{\partial x} + \lambda \frac{\partial v}{\partial y} + (l + 2m) \left(\frac{\partial u}{\partial x}\right)^2 \\ &\quad + l \frac{\partial v}{\partial y} \left(2\frac{\partial u}{\partial x} + \frac{\partial v}{\partial y}\right) + \frac{m}{2} \left(\frac{\partial u}{\partial y} + \frac{\partial v}{\partial x}\right)^2, \end{aligned} \tag{4.65}$$

$$\begin{aligned} \sigma_{22} &= (\lambda + 2\mu) \frac{\partial v}{\partial y} + \lambda \frac{\partial u}{\partial x} + (l + 2m) \left(\frac{\partial v}{\partial y}\right)^2 \\ &\quad + l \frac{\partial u}{\partial x} \left(2\frac{\partial v}{\partial y} + \frac{\partial u}{\partial x}\right) + \frac{m}{2} \left(\frac{\partial u}{\partial y} + \frac{\partial v}{\partial x}\right)^2, \end{aligned} \tag{4.66}$$

$$\sigma_{12} = \left(\frac{\partial u}{\partial y} + \frac{\partial v}{\partial x}\right) \left(\mu + m\frac{\partial u}{\partial x} + m\frac{\partial v}{\partial y}\right). \tag{4.67}$$

4.2.2 Problem Formulation

The problem of wave propagation in an elastic half-space with quadratic nonlinearity, generated by a time-harmonic line load applied normal to the surface (compare Figure 4.1) is formulated by the displacement equations of motion (4.1) with the corresponding boundary conditions given in (4.2), where the stresses are determined by (4.65)

- (4.67). The half-space is again initially at rest and hence, the initial conditions are the same as in the linear case (4.3).

It is clear that this problem is described by a second order nonlinear system of partial differential equations. Thus, the solution cannot be obtained by integral transforms as it was the case for the Original Lamb's Problem in section 4.1, since these transforms base on linear assumptions. As it was mentioned earlier, as far as the author knows, there does not exist an analytical solution to this nonlinear problem at the present time. Hence, a numerical study is necessary to gain a solution to the problem of wave propagation in an elastic half-space with quadratic nonlinearity. The next chapter describes the implementation of the numerical schemes used in this research, thereafter follows a presentation of the results gained by numerical simulations.

CHAPTER V

IMPLEMENTATION AND EVALUATION

This chapter applies the theoretical concepts and numerical solution algorithms discussed in the previous chapters to wave propagation in an elastic half-space with linear and nonlinear responses. The first part of the chapter describes the transformation of the two-dimensional wave equation (4.1) into the form of a two-dimensional conservation law (2.37) and the implementation of the free surface boundary conditions (4.2) into the numerical simulation. In the second part of the chapter follows an evaluation of the numerical scheme. This is done by firstly simulating the propagation of a one-dimensional longitudinal wave in a linear medium. With the results of this simulation, the spatial grid size for the two-dimensional simulation of wave propagation in a linear and nonlinear elastic half-space is determined. Subsequently, the two-dimensional numerical scheme is evaluated by simulating the original Lamb's problem and compare the numerical solution to the analytical one obtained in Chapter 4.

Remark. *All numerical simulations in this research are performed on a DELL Precision 690 workstation equipped with a Intel Xeon Dual Core processor with 3.0GHz and 8GB RAM.*

5.1 Implementation

This section describes the implementation of the wave propagation problem in an elastic half-space with linear and nonlinear response. First, the transformation of the two-dimensional wave equation into the form of a conservation law is described. Afterwards, the implementation of the free surface boundary conditions used in this

research is described.

5.1.1 Solution Procedure

The solution procedure of the IBVP, given by the two-dimensional wave equation (4.1), the free surface boundary conditions (4.2) and the initial conditions (4.3), is based on the transformation of the two-dimensional wave equation into the conservative form - a schematic of this transformation is shown in Figure 5.1. Transforming the constitutive equations (4.65) - (4.67) according to the scheme shown in Figure 5.1 yields

$$\begin{aligned}\sigma_{11}\left(q^3,q^4,q^5\right) &= \left(\lambda+2\mu\right)q^3+\lambda q^4+\left(l+2m\right)\left(q^3\right)^2 \\ &\quad +lq^4\left(2q^3+q^4\right)+\frac{m}{2}\left(q^5\right)^2, \end{aligned} \tag{5.1}$$

$$\begin{aligned}\sigma_{22}\left(q^3,q^4,q^5\right) &= \lambda q^3+\left(\lambda+2\mu\right)q^4+\left(l+2m\right)\left(q^4\right)^2 \\ &\quad +lq^3\left(2q^4+q^3\right)+\frac{m}{2}\left(q^5\right)^2, \end{aligned} \tag{5.2}$$

$$\sigma_{12}\left(q^3,q^4,q^5\right) = q^5\left(\mu+mq^3+mq^4\right). \tag{5.3}$$

Together with (5.1) - (5.3) and the transformation depicted in Figure 5.1, the conservative form of the two-dimensional wave equation can be written as

$$\begin{bmatrix} q^1 \\ q^2 \\ q^3 \\ q^4 \\ q^5 \end{bmatrix}_{,t} + \begin{bmatrix} -\frac{1}{\rho}\sigma_{11}\left(q^3,q^4,q^5\right) \\ -\frac{1}{\rho}\sigma_{12}\left(q^3,q^4,q^5\right) \\ -q^1 \\ 0 \\ -q^2 \end{bmatrix}_{,x} + \begin{bmatrix} -\frac{1}{\rho}\sigma_{12}\left(q^3,q^4,q^5\right) \\ -\frac{1}{\rho}\sigma_{22}\left(q^3,q^4,q^5\right) \\ 0 \\ -q^2 \\ -q^1 \end{bmatrix}_{,y} = \mathbf{0}, \tag{5.4}$$

where $q^i = q^i\left(x,y,t\right)$. The constitutive equations given in (5.1) - (5.3) are the transformed equations for an elastic half-space with quadratic nonlinearity. The transformed constitutive equations for an elastic half-space with linear response can be obtained from these equations by setting $l=0$ and $m=0$. Therefore, the schematic

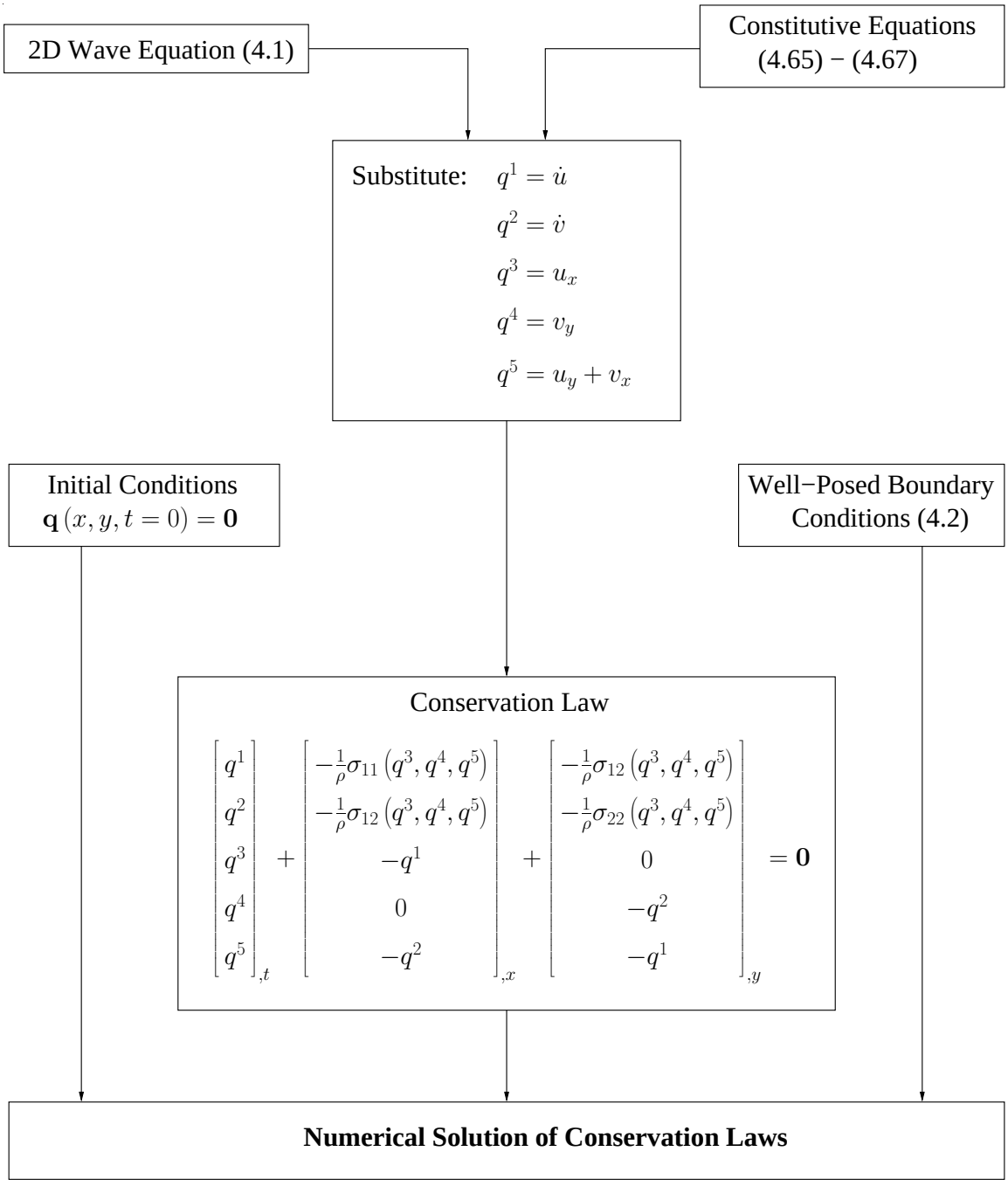

Figure 5.1: Solution procedure for the two-dimensional wave equation.

in Figure 5.1 holds for the linear and the nonlinear problem.

For the linear wave propagation problem ($l = 0$, $m = 0$), the Jacobian matrices $\frac{\partial \mathbf{f}}{\partial \mathbf{q}}$ and $\frac{\partial \mathbf{g}}{\partial \mathbf{q}}$ of the linear system of conservation laws (5.4) have both the same eigenvalues at $\nu_1 = 0$, $\nu_{2,3} = \pm c_l$ and $\nu_{4,5} = \pm c_t$. It can also be shown that all linear combinations of $\frac{\partial \mathbf{f}}{\partial \mathbf{q}}$ and $\frac{\partial \mathbf{g}}{\partial \mathbf{q}}$ have real eigenvalues. Hence, following Definition 2.2, the linear system of conservation laws (5.4) is hyperbolic.

In the nonlinear case, the hyperbolicity of (5.4) is not guaranteed in all regions, as there exist some regions, where the Jacobian matrices $\frac{\partial \mathbf{f}}{\partial \mathbf{q}}$ and $\frac{\partial \mathbf{g}}{\partial \mathbf{q}}$ have complex eigenvalues. But the numerical schemes introduced in Chapter 3 hold only for hyperbolic systems, thus it has to be guaranteed that the system stays in the hyperbolic region and does not converge to the regions where the eigenvalues are complex. Whether the eigenvalues are complex, depends only on q^3, q^4 and q^5 and thus on the spatial derivatives of $u(x, y, t)$ and $v(x, y, t)$. Hence, the hyperbolicity can be guaranteed by limiting the amplitude Q of the input. This is no constraint, since the geometrical nonlinearities are neglected, as described in Section 4.2.1, and therefore only small displacements are assumed.

5.1.2 Implementation of the Boundary Conditions

One key factor by numerical simulations of real physical boundary value problems is the right implementation of the boundary conditions, since they have an immense influence on the solution of the problem. In the case of wave propagation problems, the boundary conditions determine which type of waves will propagate in the domain under consideration. As it was seen in Chapter 4, the free surface boundary conditions of an elastic half-space force the propagation of four different types of waves - the longitudinal wave, the transverse wave, the head wave and the Rayleigh wave.

A numerical simulation requires not only the correct implementation of the physical boundary conditions, but also an implementation of so called numerical boundary

conditions. Numerical boundary conditions arise, since it is often not possible to simulate the whole physical domain. In the case of a half-space, it is clear that it is impossible to simulate the whole half-space, hence only a small region of the half-space is simulated. On the other hand, this means that there appear three other boundaries in the physical domain. Thus, the numerical scheme has to ensure that these artificial boundaries have no effect on the numerical solution.

5.1.2.1 Physical Boundary Conditions

The implementation of the physical boundary conditions in this research is done by the ghost-cell method [17]. This method bases on the extension of the physical domain by some ghost-cells, which have no physical meaning. These cells are used to force some boundary condition dependent values in the solution of the interior cells located in the physical domain. Therefore, the values of the ghost cells are set at the beginning of each time step in some manner that depends on the boundary conditions and perhaps the interior (physical) solution of the last time step.

Figure 5.2 shows the extension of the free surface at $y = 0$ of the elastic half-space. For the implementation of the ghost-cell method it is required that the numerical domain ends exactly at the physical boundary, thus the grid used for the numerical simulation in this research is

$$x_j = j\Delta x \quad \text{and} \quad y_k = \frac{\Delta y}{2} + k\Delta y, \quad j,k \in \mathbb{Z}. \tag{5.5}$$

This choice of the grid ensures also the correct implementation of the surface load for Lamb's problem.

As mentioned above, the values in the ghost-cells ($k = -1, -2$) have to ensure that the free surface boundary conditions (4.2) are satisfied. Since the particle velocities $q^1 = \dot{u}$ and $q^2 = \dot{v}$ are not influenced by the boundary, they are symmetrically

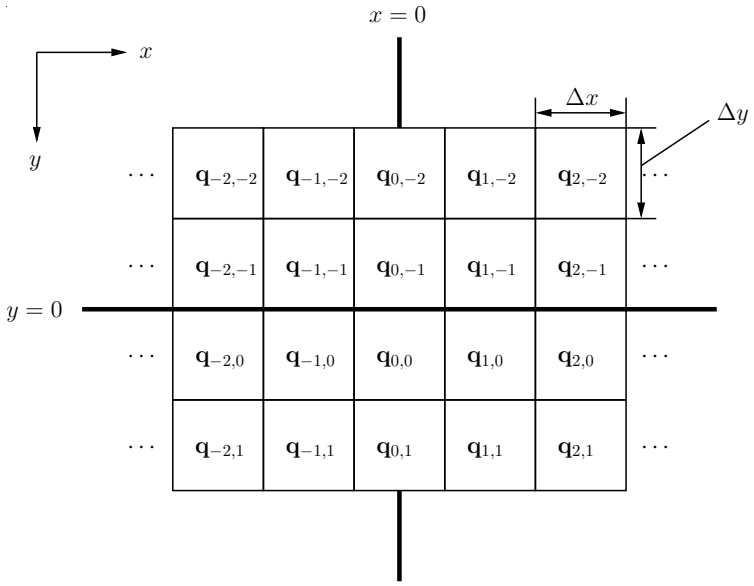

Figure 5.2: Extension of the physical half-space by ghost-cells at $y = 0$.

extrapolated to the ghost-cells, which yields

$$\begin{aligned} q^1_{j,-k} &= q^1_{j,k-1}, \\ q^2_{j,-k} &= q^2_{j,k-1}, \end{aligned} \tag{5.6}$$

where $j \in \mathbb{Z},\ k = 1, 2$. The same holds for the normal stress into the x-direction $\sigma_{11}\left(q^3, q^4, q^5\right)$. The normal stress into the y-direction $\sigma_{22}\left(q^3, q^4, q^5\right)$ and the transverse stress $\sigma_{12}\left(q^3, q^4, q^5\right)$ are influenced directly by the free surface boundary conditions (4.2), hence they have to be considered differently. Figure 5.2 shows that the values exactly on the physical boundary are given by linear interpolation between the ghost cells and the interior cells for $k = 0, 1$. Since the values on the physical boundary for $\sigma_{22}\left(q^3, q^4, q^5\right)$ and $\sigma_{12}\left(q^3, q^4, q^5\right)$ are given by the boundary conditions, the needed values for q^3, q^4 and q^5 can be obtained together with the symmetrical extrapolation of $\sigma_{11}\left(q^3, q^4, q^5\right)$ from a set of equations

$$\begin{aligned} \sigma_{11}\left(q^3_{j,-k}, q^4_{j,-k}, q^5_{j,-k}\right) - \sigma_{11}\left(q^3_{j,k-1}, q^4_{j,k-1}, q^5_{j,k-1}\right) &= 0, \\ \sigma_{22}\left(q^3_{j,-k}, q^4_{j,-k}, q^5_{j,-k}\right) + \sigma_{22}\left(q^3_{j,k-1}, q^4_{j,k-1}, q^5_{j,k-1}\right) &= 2QF\left(t\right)\delta\left(x_j\right), \\ \sigma_{12}\left(q^3_{j,-k}, q^4_{j,-k}, q^5_{j,-k}\right) + \sigma_{12}\left(q^3_{j,k-1}, q^4_{j,k-1}, q^5_{j,k-1}\right) &= 0, \end{aligned} \tag{5.7}$$

with $j \in \mathbb{Z}$ and $k = 1, 2$, where σ_{11}, σ_{22} and σ_{12} are given by equation (5.1) - (5.3). Since the numerical schemes used in this research are a semi-discrete schemes, it always holds $q^i_{j,k} = q^i_{j,k}(t)$.

For a linear elastic half-space ($l = 0$, $m = 0$), the solution to the set of equations (5.7) can be obtained easily and is given by

$$\begin{aligned} q^3_{j,-k} &= \frac{(\lambda + 2\mu)\,\sigma_{11}(j, k-1) + \lambda\,(\sigma_{22}(j, -k) - 2QF(t)\,\delta(x_j))}{4\mu(\lambda + \mu)}, \\ q^4_{j,-k} &= -\frac{\lambda\sigma_{11}(j, k-1) + (\lambda + 2\mu)\,(\sigma_{22}(j, k-1) - 2QF(t)\,\delta(x_j))}{4\mu(\lambda + \mu)}, \\ q^5_{j,-k} &= -\frac{\sigma_{12}(j, k-1)}{\mu}, \end{aligned} \tag{5.8}$$

with $j \in \mathbb{Z}$ and $k = 1, 2$; where $\sigma_{mn}(j, k) = \sigma_{mn}\left(q^3_{j,k}, q^4_{j,k}, q^5_{j,k}\right)$.

For a nonlinear elastic half-space ($l \neq 0$, $m \neq 0$) the set of equations (5.7) is a nonlinear system of equations, therefore it cannot be solved as easy as in the linear case. In this research, the solution to this nonlinear system of equations is obtained iteratively using the Newton-Raphson method [5]. The convergence of the Newton-Raphson method to the right physical solution depends highly on the initial guess, hence a good initial guess is required to ensure that the right solution is obtained.

It is known that the solution in a nonlinear elastic half-space is mostly driven by the linear parts [28], thus the initial guess for solving the nonlinear system of equations (5.7) using the Newton-Raphson method can be obtained from the solution to the linear system of equations (5.8).

The Dirac delta impulse in equation (5.7) is implemented by

$$\delta(x_j) = \begin{cases} \frac{1}{\Delta x} & \text{, if } j = 0 \\ 0 & \text{else.} \end{cases} \tag{5.9}$$

5.1.2.2 Numerical Boundary Conditions

There are basically two possibilities to implement the numerical boundaries of a half-space. One way is, to choose the size of the simulation domain in such a way that the propagating wave fronts do not reach the numerical boundaries in the entire simulation. Since this method requires normally a large simulation domain, it is very costly in the sense of computational time. The other approach to implement the numerical boundary conditions is to ensure that the waves can leave the simulation domain without reflection. This approach is chosen in this research and is realized again through the ghost-cell method; the values in the ghost-cells are calculated by zero-order extrapolation.

The numerical boundaries for the two-dimensional half-space under consideration are at $x = \pm\tilde{x} = \pm J\Delta x \pm \frac{\Delta x}{2}$ and $y = \tilde{y} = (K+1)\Delta y$. Hence, the zero-order extrapolation at the different numerical boundaries yields

$$\begin{aligned} q^i_{j,K+k} &= q^i_{j,K}\,, \qquad j \in \mathbb{Z},\ k = 1, 2, \\ q^i_{\pm J \pm j,k} &= q^i_{\pm J,k}\,, \qquad j = 1, 2\ k \in \mathbb{Z}, \end{aligned} \tag{5.10}$$

where $i = 1, \ldots, 5$.

5.2 Evaluation

The following section shows the convergence of the numerical solution to the analytical one of wave propagation in a linear elastic half-space. Therefore, first the propagation of a plane wave in an one-dimensional linear elastic half-space is considered to determine the optimal spatial grid size for the two-dimensional simulations.

5.2.1 Benchmark with a One-Dimensional Wave Propagation Problem

For one-dimensional wave propagation problems with the spatial variable y, equation (4.1) reduces to

$$\frac{\partial \sigma_{22}}{\partial y} = \rho \frac{\partial^2 v}{\partial t^2}, \tag{5.11}$$

with $\sigma_{22} = \sigma_{22}(y,t)$ and $v = v(y,t)$. The constitutive equation for the normal stress in y-direction (in linear elastic material) can be written as

$$\sigma_{22} = (\lambda + 2\mu) \frac{\partial v}{\partial y}. \tag{5.12}$$

To determine the spatial grid size for the simulation of an elastic half-space with two dimensions, the propagation of a plane wave in an one-dimensional half-space ($y \geq 0$) with excitation at one boundary is considered. Hence the boundary condition is given by

$$\sigma_{22}(0,t) = -QF(t). \tag{5.13}$$

It is assumed that the domain is initially at rest, which yields

$$v(y,0) = 0. \tag{5.14}$$

The transformation of equation (5.11) together with the constitutive equation (5.12), the initial condition (5.14) and the boundary condition (5.13) into a conservation law

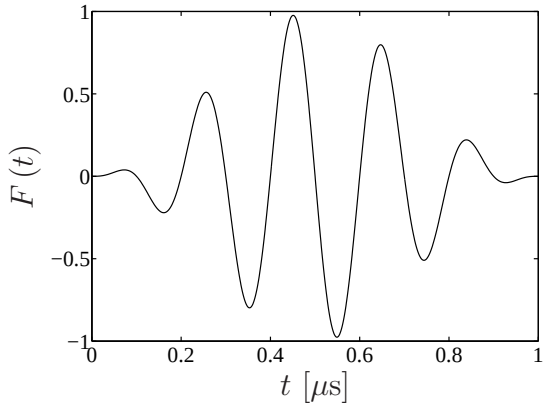

Figure 5.3: Excitation signal $F(t)$ at $y = 0$.

Table 5.1: Parameters for the simulation of a plane wave in linear elastic media.

ρ $\left[\frac{\text{kg}}{\text{m}^3}\right]$	$\lambda \times 10^{-10}$ $\left[\frac{\text{N}}{\text{m}^2}\right]$	$\mu \times 10^{-10}$ $\left[\frac{\text{N}}{\text{m}^2}\right]$	f_f [MHz]	t_f [μs]	$Q \times 10^{-6}$ $\left[\frac{\text{N}}{\text{m}^2}\right]$
2719	4.91	2.6	5	1	20

is similar to the one in two dimensions and can be found in the literature [19]. The result is given without derivation and can be written as

$$\begin{bmatrix} q^1 \\ q^2 \end{bmatrix}_{,t} + \begin{bmatrix} -\frac{1}{\rho}\sigma_{22}\left(q^2\right) \\ -q^1 \end{bmatrix}_{,y} = \mathbf{0}, \tag{5.15}$$

with

$$\sigma_{22}\left(q^1\right) = \left(\lambda + 2\mu\right) q^2, \tag{5.16}$$

where $q^i = q^i(y,t)$. The excitation signal $F(t)$ for the one-dimensional simulation of a propagating plane wave in an elastic material and for all following simulations is

$$F(t) = \frac{1}{2}\sin\left(2\pi f_f t\right)\left(1 - \cos\left(2\pi\left(\frac{t}{t_f}\right)\right)\right), \tag{5.17}$$

which is shown in Figure 5.3. The implementation of the boundary condition and the numerical grid is generally the same as for the two-dimensional case.

Table 5.1 shows the parameters used for the simulation of a plane wave in linear elastic media. The density and the second-order elastic constants are real material

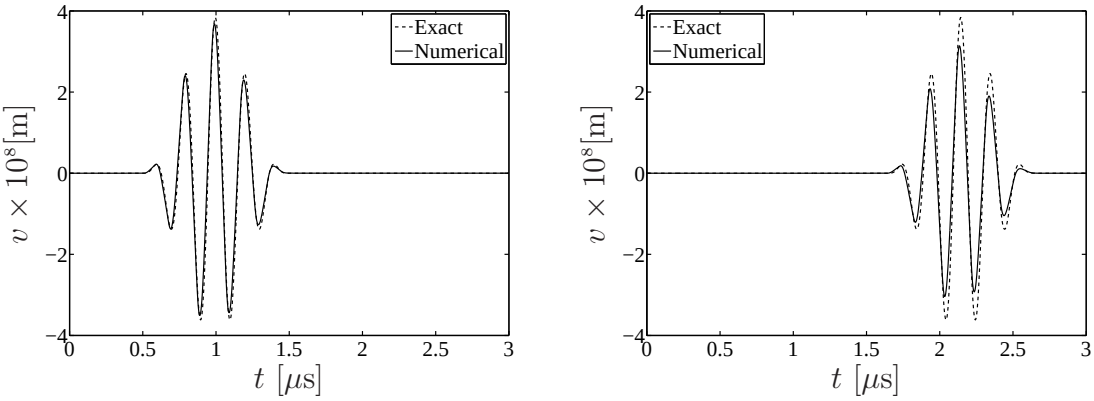

(a) Displacement v at $y_1 = 3$mm (b) Displacement v at $y_2 = 10$mm

Figure 5.4: Numerical solution for a propagating plane wave with a spatial discretization of 30 grids per wavelength and exact solution.

values and correspond to Aluminum D54S [23]. The numerical boundary is located at $\tilde{y} = 20$mm and the simulation time is set to $t_{\text{sim}} = 5\mu$s.

For a fine spatial resolution of the numerical solution, the spatial discretization has to be chosen in dependence to the smallest appearing wavelength [16], [28]. For this one-dimensional problem, the smallest wavelength is the one of the propagating longitudinal wave, as this is the only occurring wave.

To obtain an optimal spatial discretization, the one-dimensional wave propagation problem is solved numerically with different discretization values Δy and compared to the exact analytical solution. The derivation of the analytical solution for this linear plane wave problem is given in Appendix B. Figure 5.4 compares the numerical results at two fixed spatial points ($y_1 = 3$mm and $y_2 = 10$mm) with the exact analytical solution over the time for a discretization of 30 grids per wavelength, corresponding to $\Delta y = 4 \times 10^{-5}$m. It shows a noticeable numerical error, especially at $y = y_2$. It is expected that the numerical error decreases with a finer discretization. Using a spatial discretization of 60 grids per wavelength, yields the results shown in Figure 5.5. These results show clearly the expected decrease of the numerical error, as the numerical solution converges to the analytical one.

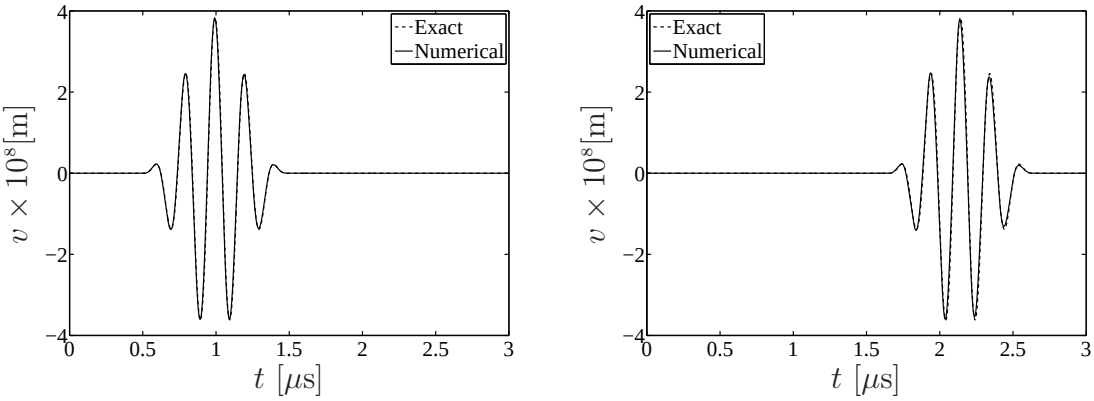

(a) Displacement v at $y_1 = 3$mm (b) Displacement v at $y_2 = 10$mm

Figure 5.5: Numerical solution for a propagating plane wave with a spatial discretization of 60 grids per wavelength and exact solution.

A better analysis of harmonic signals can be made using the FFT [21], since these transform allows an evaluation in the frequency domain. Since the problem considered in this section is a linear wave propagation problem, theoretically only the fundamental frequency f_f of the excitation signal $F(t)$ occurs in the solution. Because the displacement in the numerical solution is obtained from the particle velocity by numerical integration, the FFT is carried out with the particle velocity in order to get the most undisturbed signal.

Figures 5.6 and 5.7 show the FFT of $\dot{v}$ for a spatial discretization of 30 and 60 grids per wavelength, respectively. In both figures unexpected odd harmonics of the fundamental frequency f_f of the excitation signal occur. On the other hand, it can be seen that the magnitude A_3 and A_5, where $A_i = A(if_f)$, in comparison to the magnitude of the fundamental frequency A_1 in Figure 5.7 is smaller than in Figure 5.6. Hence it is expected, that these occurrence of the odd harmonics is vanishing through a refinement of the spatial grid size.

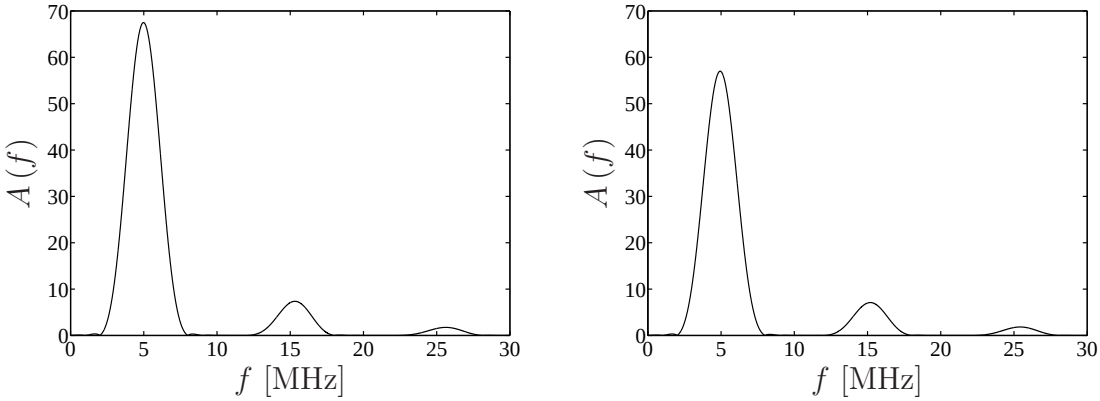

(a) FFT of $\dot{v}$ at $y_1 = 3\text{mm}$ (b) FFT of $\dot{v}$ at $y_2 = 10\text{mm}$

Figure 5.6: FFT of particle velocity $\dot{v}$ of the numerical solution for a spatial discretization of 30 grids per wavelength.

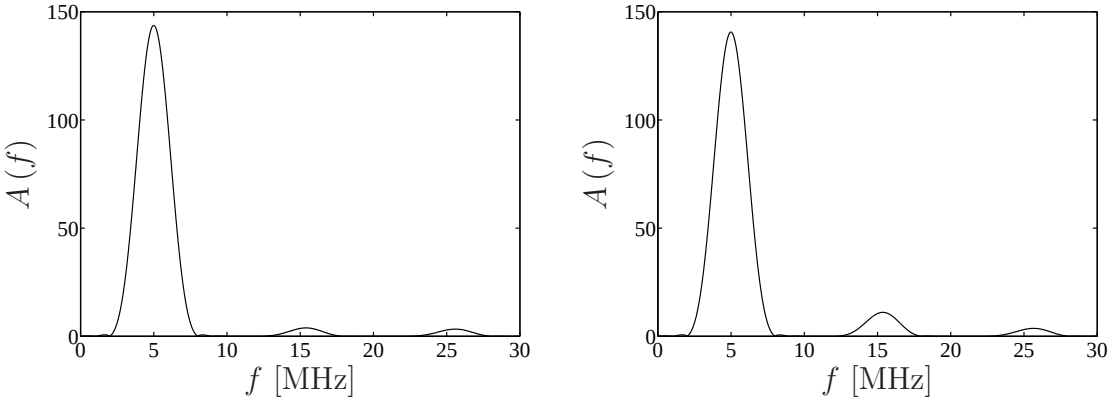

(a) FFT of $\dot{v}$ at $y_1 = 3\text{mm}$ (b) FFT of $\dot{v}$ at $y_2 = 10\text{mm}$

Figure 5.7: FFT of particle velocity $\dot{v}$ of the numerical solution for a spatial discretization of 60 grids per wavelength.

Figure 5.8 shows the displacement over the time obtained from a numerical simulation with a discretization of approximately 3000 grids per wavelength, which corresponds to $\Delta y = 4 \times 10^{-7}\text{m}$. It shows obviously the convergence of the numerical solution to the exact analytical one. Furthermore, the corresponding FFT of the particle velocity in Figure 5.9 indicates the expected vanishing of the odd harmonics in comparison to the fundamental frequency.

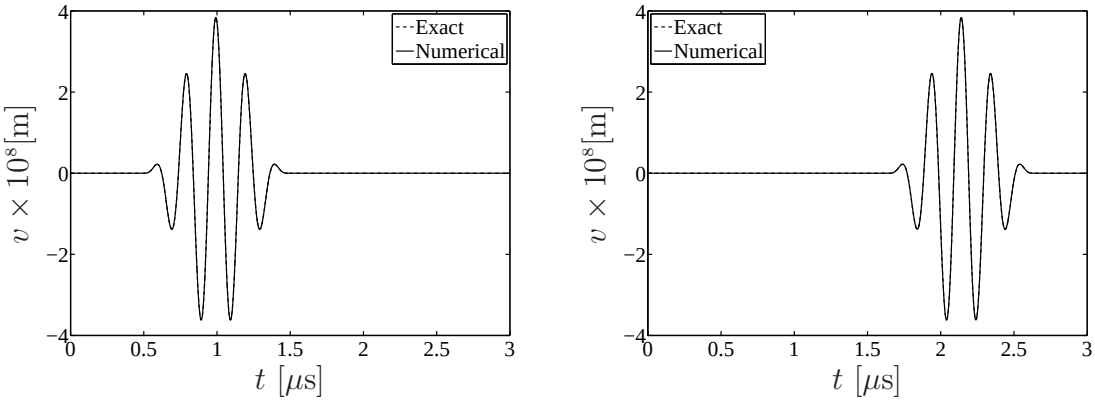

(a) Displacement v at $y_1 = 3$mm (b) Displacement v at $y_2 = 10$mm

Figure 5.8: Numerical solution for a propagating plane wave with a spatial discretization of 3000 grids per wavelength and exact solution.

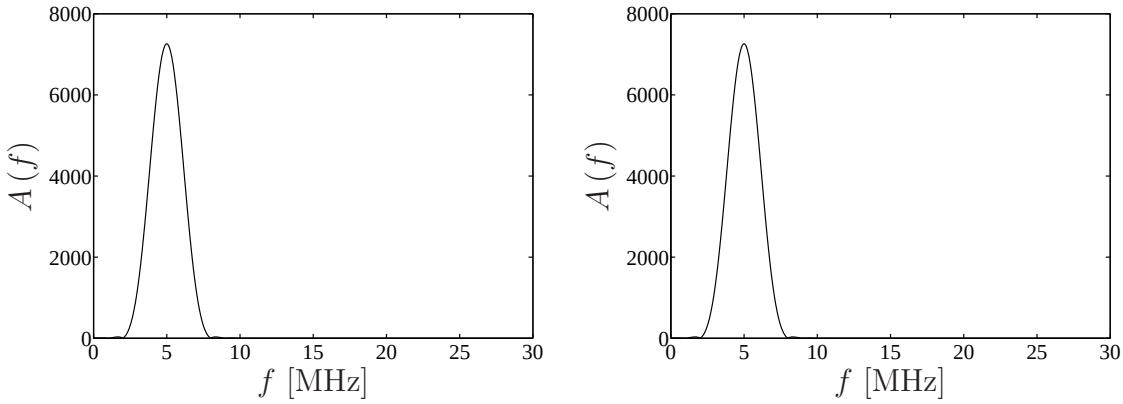

(a) FFT of $\dot{v}$ at $y_1 = 3$mm (b) FFT of $\dot{v}$ at $y_2 = 10$mm

Figure 5.9: FFT of particle velocity $\dot{v}$ of the numerical solution for a spatial discretization of 3000 grids per wavelength.

To summarize, Figures 5.10 and 5.11 illustrate the decreasing of the undesirable odd harmonics with declining spatial grid size in comparison to the amplitude of the fundamental frequency f_f at $y = y_1$ and $y = y_2$, respectively.

On the one hand, the numerical error decreases with a finer spatial discretization, but on the other hand it is clear that the computational time increases. Especially, when simulating a two-dimensional half-space, the spatial discretization has an enormous

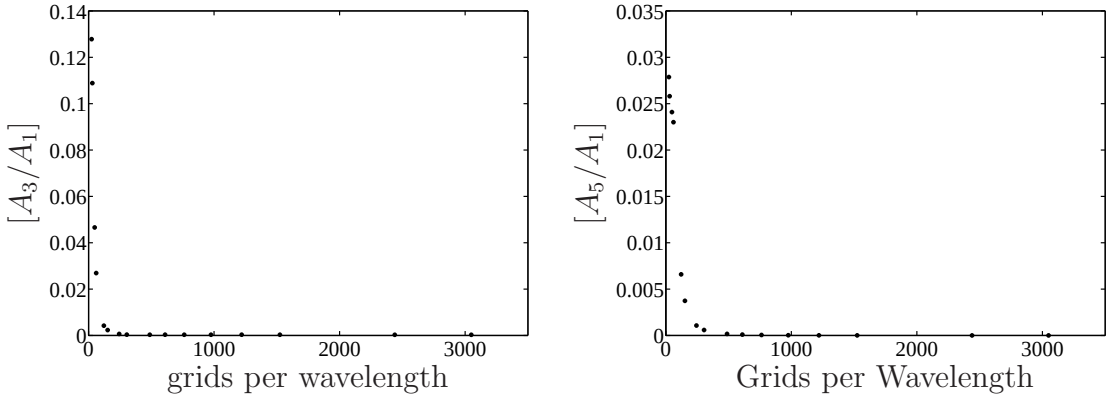

(a) Amplitude of third harmonic (b) Amplitude of fifth harmonic

Figure 5.10: Value of A_3/A_1 and A_5/A_1 at $y_1 = 3$mm over grids per wavelength.

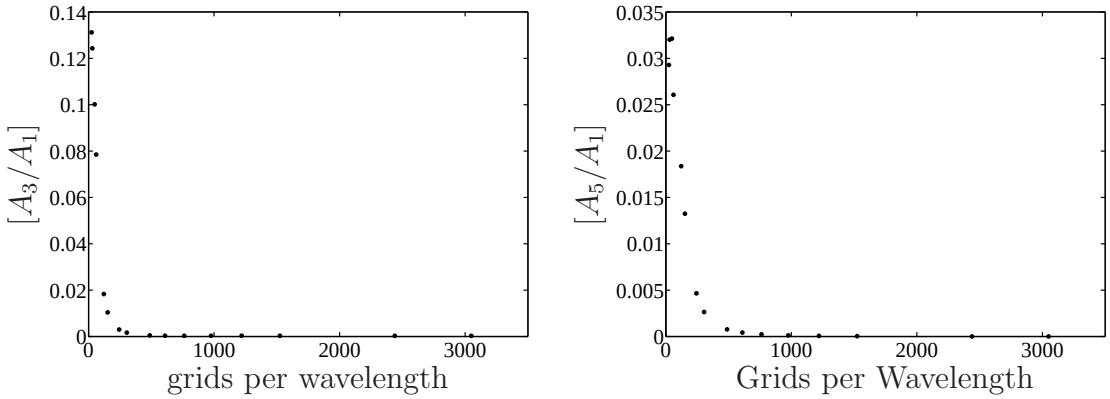

(a) Amplitude of third harmonic (b) Amplitude of fifth harmonic

Figure 5.11: Value of A_3/A_1 and A_5/A_1 at $y_2 = 10$mm over grids per wavelength.

influence on the computational time. Moreover, according to the CFL condition (3.27) the time step Δt has to decrease also with the spatial step and therefore the computational effort increases additionally. Hence, one has to make a compromise between the numerical error and the computational effort.

From the results above it can be assumed that 60 grids per smallest occurring wavelength yields a resolution which is high enough. Using this discretization, the computational effort is still realizable.

Table 5.2: Parameters for the simulation of the original Lamb's problem.

$\rho \left[\frac{\text{kg}}{\text{m}^3}\right]$	$\lambda \times 10^{-10} \left[\frac{\text{N}}{\text{m}^2}\right]$	$\mu \times 10^{-10} \left[\frac{\text{N}}{\text{m}^2}\right]$	f_f [MHz]	t_f [μs]	$Q \times 10^{-4} \left[\frac{\text{N}}{\text{m}}\right]$
2719	4.91	2.6	5	1	1

5.2.2 Benchmark with the Original Linear Lamb's Problem

This part presents the numerical results to the original Lamb's problem and compare them to the exact analytical solution obtained in Chapter 4. The excitation signal $F(t)$ at $x = 0$, $y = 0$ (see Figure 4.8) is the same as in the previous section and given in Figure 5.3. Besides the load Q, the simulation parameters are the same as in the one-dimensional simulation and shown in Table 5.2. According to the results given above, the (x, y)-domain is discretized in x- and y-direction with approximately 60 grids per smallest occurring wavelength, which depends in the two-dimensional case to the transverse wave[1] and is therefore given by $\Delta x = \Delta y = 9 \times 10^{-6}$m. The numerical boundaries are located at $\tilde{x} = \pm 11.25$mm and $\tilde{y} = 11.25$mm, thus the simulation domain (-11.25mm $\leq x \leq$ 11.25mm and $0 \leq y \leq$ 11.25mm) is discretized into 2501×1250 grids. The simulation time is set to $t_{\text{sim}} = 2.8\mu$s.

The results are presented in a way that the numerical solution is compared to the analytical one at different fixed points in the half-space, which are expressed in Polar coordinates (see Figure 4.2). Hence the time-signal of the displacements in the x- and y-direction are evaluated for three different radii, $r = 2$mm, 4mm, 5.2mm and four different angles $\theta = 0°$, $30°$, $60°$, $89.5°$[2].

Figures 5.12, 5.13, 5.14 and 5.15 show the obtained results at $r = 2$mm for $\theta = 0°$, $30°$, $60°$, $89.5°$, respectively.

[1] The wave with the smallest wavelength is actually the Rayleigh wave, but this wave occurs only on the surface. Thus the transverse wave is taken to determine the grid size

[2] The results are not presented at $\theta = 90°$, since the implementation of the numerical grid (5.5) only gives a solution at $\theta = 89.5°$

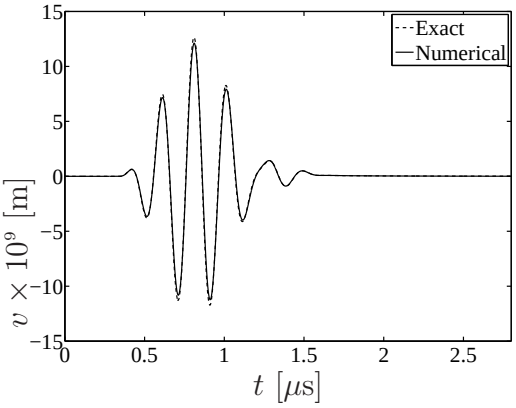

Figure 5.12: Numerical solution of displacement v at $r = 2$mm and $\theta = 0°$ and exact solution.

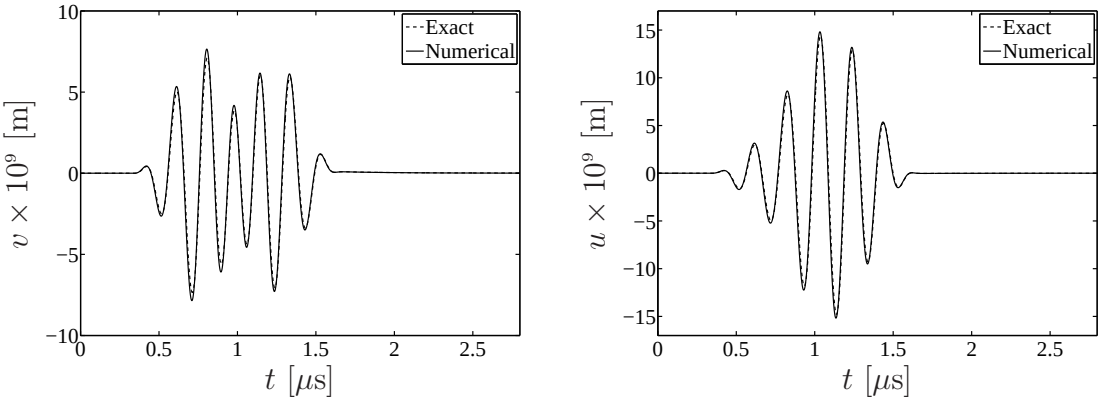

(a) Displacement v (b) Displacement u

Figure 5.13: Numerical solution of displacements at $r = 2$mm and $\theta = 30°$ and exact solution.

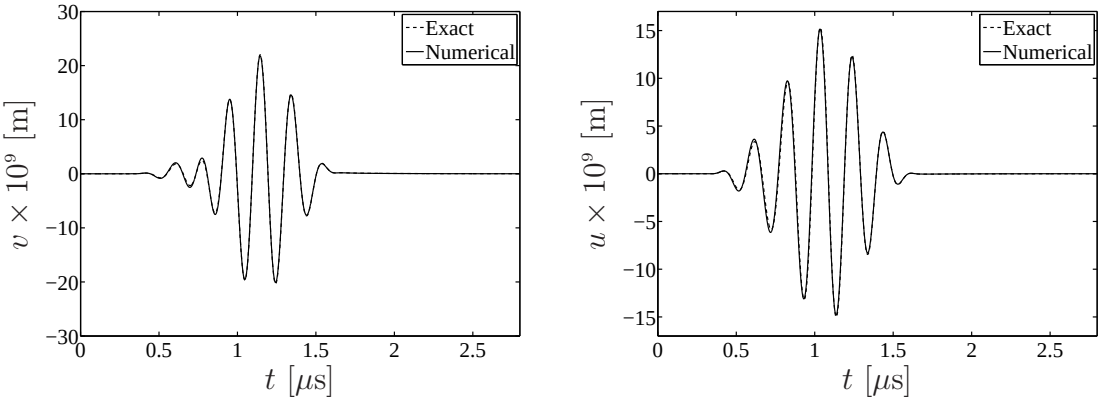

(a) Displacement v (b) Displacement u

Figure 5.14: Numerical solution of displacements at $r = 2$mm and $\theta = 60°$ and exact solution.

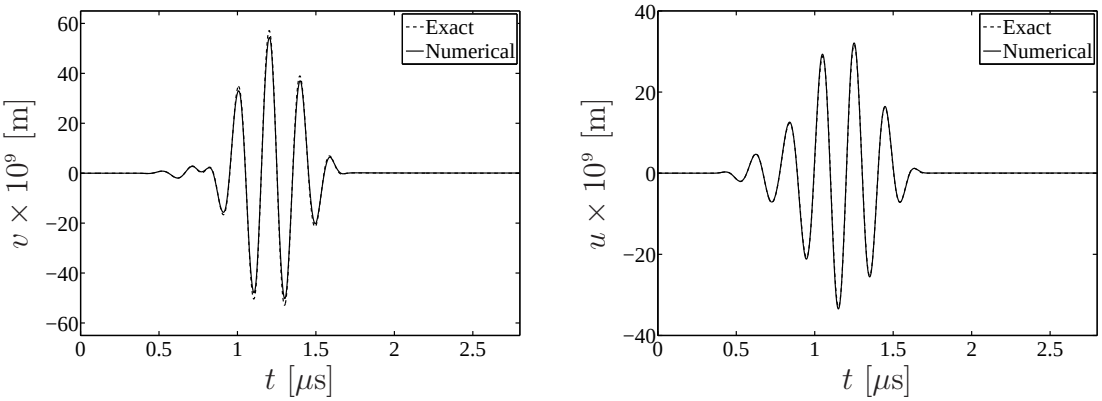

(a) Displacement v (b) Displacement u

Figure 5.15: Numerical solution of displacements at $r = 2$mm and $\theta = 89.5°$ and exact solution.

These figures illustrate that the longitudinal wave and transverse wave are not separated from each other at $r = 2$mm. Furthermore, they clarify that the numerical solution converges to the exact analytical solution.

Figures 5.16, 5.17, 5.18 and 5.19 give the obtained numerical results in comparison to the analytical solution at $r = 4$mm for $\theta = 0°$, $30°$, $60°$, $89.5°$, respectively. The longitudinal wave and the transverse wave are still not completely separated from each other.

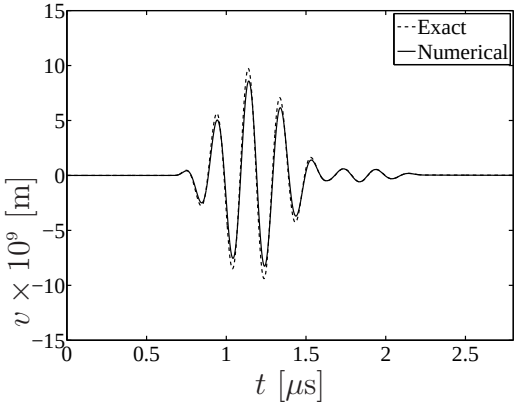

Figure 5.16: Numerical solution of displacement v at $r = 4$mm and $\theta = 0°$ and exact solution.

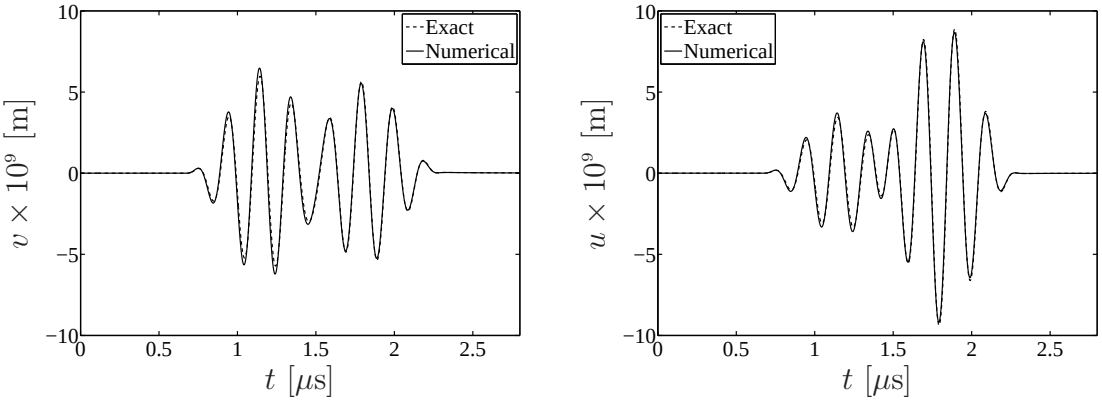

(a) Displacement v (b) Displacement u

Figure 5.17: Numerical solution of displacements at $r = 4$mm and $\theta = 30°$ and exact solution.

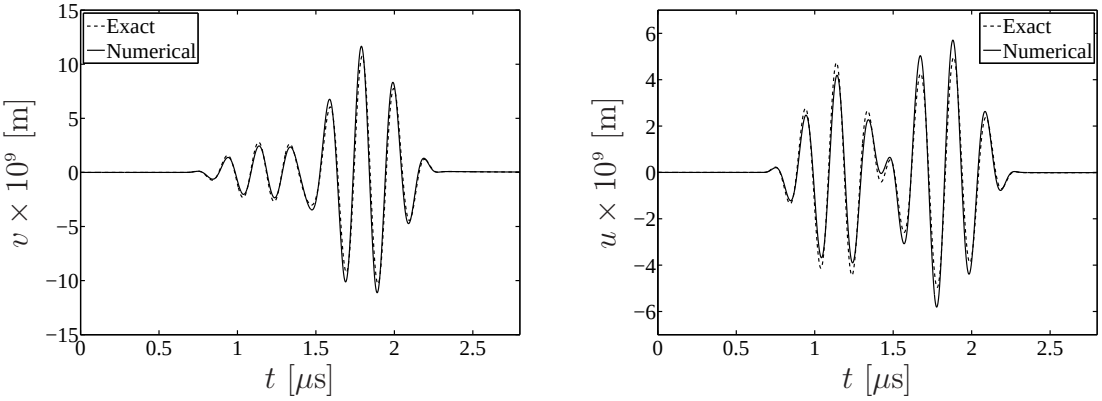

(a) Displacement v (b) Displacement u

Figure 5.18: Numerical solution of displacements at $r = 4$mm and $\theta = 60°$ and exact solution.

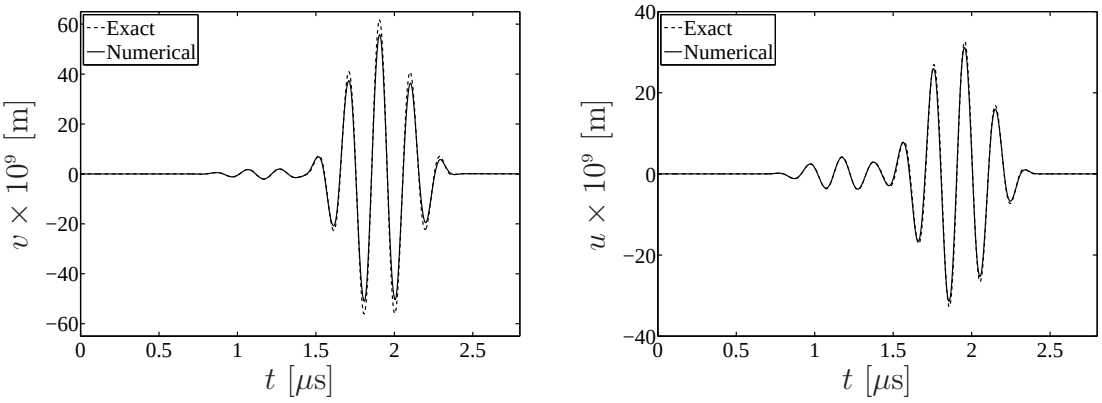

(a) Displacement v (b) Displacement u

Figure 5.19: Numerical solution of displacements at $r = 4$mm and $\theta = 89.5°$ and exact solution.

It figures out that the numerical error is increasing for $\theta = 60°$ and $89.5°$, especially in the transverse wave part. This can be referred to the fact that in this region the head wave occurs. The head wave has the wavelength of the transverse wave and therefore it is sampled with 60 grids per wavelength, contrary to the longitudinal wave, which is sampled with approximately 120 grids per wavelength. Hence, it is clear that the numerical error in the parts of the solution, which are dominated by the transverse wave parts, is higher than in the parts where the longitudinal wave dominates.

Figures 5.20, 5.21, 5.22 and 5.23 illustrates the numerical solution at $r = 5.2$mm for $\theta = 0°$, $30°$, $60°$, $89.5°$, respectively.

Now, the longitudinal wave is almost separated from the transverse wave. Again, Figure 5.22 and 5.23 indicate the phenomenon that the numerical error in the transverse wave part is higher than in the longitudinal wave part.

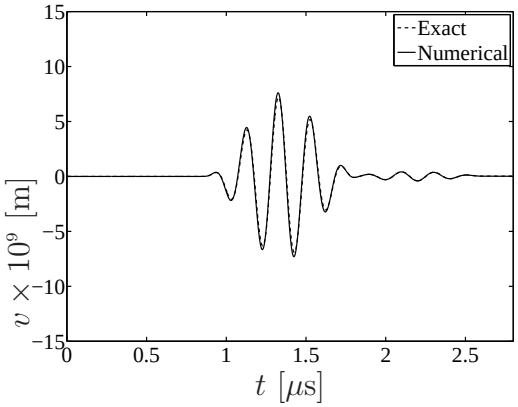

Figure 5.20: Numerical solution of displacement v at $r = 5.2$mm and $\theta = 0°$ and exact solution.

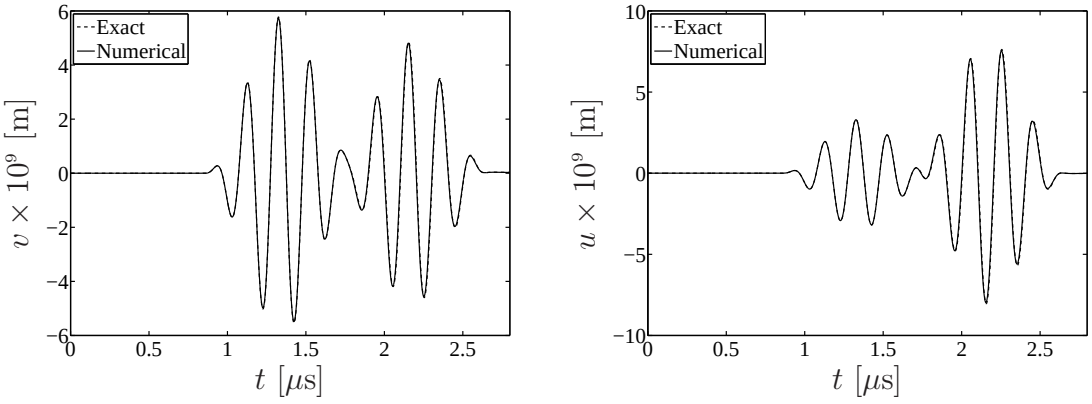

(a) Displacement v (b) Displacement u

Figure 5.21: Numerical solution of displacements at $r = 5.2$mm and $\theta = 30°$ and exact solution.

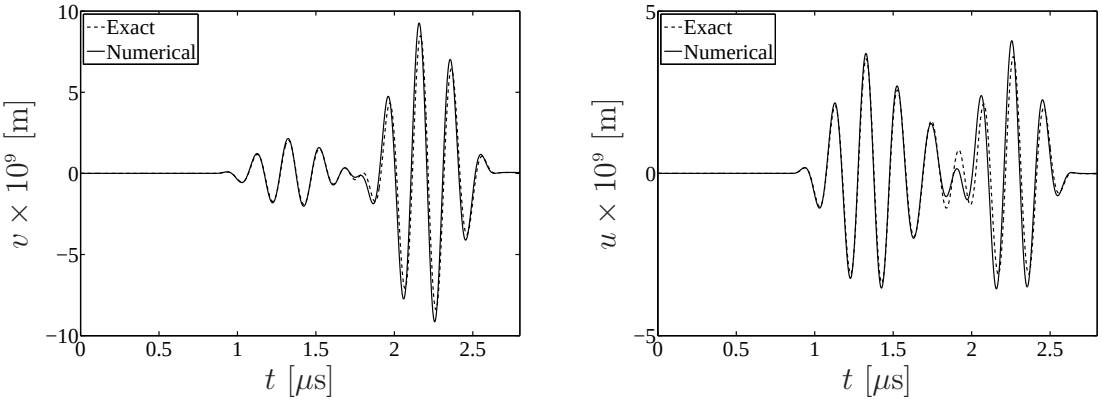

(a) Displacement v (b) Displacement u

Figure 5.22: Numerical solution of displacements at $r = 5.2$mm and $\theta = 60°$ and exact solution.

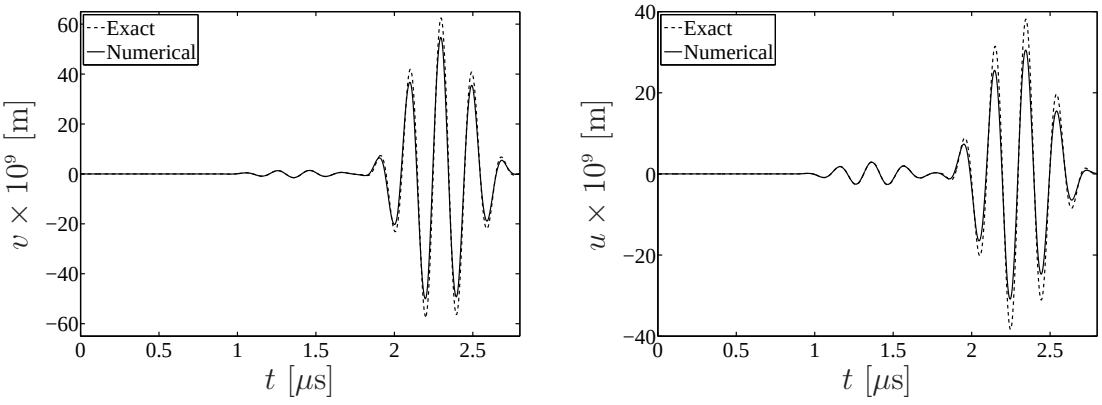

(a) Displacement v (b) Displacement u

Figure 5.23: Numerical solution of displacements at $r = 5.2$mm and $\theta = 89.5°$ and exact solution.

5.3 Summary

This section presents the numerical results of linear one- and two-dimensional wave propagation problems in comparison to the exact analytical solution. It points out that the numerical error highly depends on the spatial discretization. But on the other hand, one has always to consider the computational cost in the sense of computational time.

The numerical results of the original Lamb's problem illustrate that the numerical solution is in good agreement with the exact analytical solution; especially in the region where the longitudinal wave dominates. Furthermore, the computational effort is still affordable, but a noticeable refinement of the grid showed that the computational time blows up. Thus, the grid size, the simulation domain and the simulation time used in Section 5.2.2 hold for all following simulations presented in the next chapter.

CHAPTER VI

RESULTS

In the following chapter, the results of the numerical simulation of propagating waves in an elastic half-space with quadratic nonlinearity are presented. The numerical schemes used for these simulations are introduced in Chapter 3, the problem formulation is given in Chapter 4. The results are presented in a way that first only the time domain is considered. In this section follows an evaluation of the compliance of the free surface boundary conditions and the obtained results are compared to the results of the linear wave propagation problem presented in the last chapter. In the second part of the chapter, the solution is presented in the frequency domain. Thus, the propagation of an one-dimensional plane wave in an elastic medium with quadratic nonlinearity is firstly considered to introduce the acoustical nonlinearity parameter β. Afterwards, it is verified that such a parameter can be also defined for cylindrical waves and how this parameter depends on different locations in the half-space as well as on different material properties.

The excitation signal $F(t)$ is for all following simulations the same as in the last chapter and specified by (5.17). The simulation parameters used in the two-dimensional nonlinear simulations are given in Table 6.1, the material and input parameters are shown in Table 6.2.

Table 6.1: Simulation Parameters.

t_{sim} [μs]	$\Delta x \times 10^6$ [m]	$\Delta y \times 10^6$ [m]	J	K	$\tilde{x}$ [mm]	$\tilde{y}$ [mm]
2.8	9	9	1250	1250	$\pm$ 11.25	11.25

Table 6.2: Parameters for wave propagation in a nonlinear elastic half-space.

ρ $\left[\frac{\text{kg}}{\text{m}^3}\right]$	$\lambda \times 10^{-10}$ $\left[\frac{\text{N}}{\text{m}^2}\right]$	$\mu \times 10^{-10}$ $\left[\frac{\text{N}}{\text{m}^2}\right]$	$l \times 10^{-10}$ $\left[\frac{\text{N}}{\text{m}^2}\right]$	$m \times 10^{-10}$ $\left[\frac{\text{N}}{\text{m}^2}\right]$	f_f [MHz]	t_f [μs]	$Q \times 10^{-4}$ $\left[\frac{\text{N}}{\text{m}}\right]$
2719	4.91	2.6	-38.75	-35.8	5	1	1

The density ρ and the second- and third-order elastic constants are again real material values and correspond to Aluminum D54S [23].

6.1 Time-Domain

As mentioned in the last chapter, the right implementation of the boundary conditions is a very important factor when simulating BVP. Especially in this nonlinear wave propagation problem, as described in Chapter 5, the implementation of the boundary conditions is not straightforward. Hence, the compliance of the physical boundary conditions is evaluated in the following. Figure 6.1 and 6.2 show exemplary the values of σ_{22} and σ_{12} at $|x| \leq \tilde{x}$ and $y = 0$ for $t = 1.26\mu$s and $t = 2.52\mu$s, respectively. These values are calculated using linear interpolation between the cells at $k = 0$ and $k = -1$ (first ghost-cells).

Besides a small numerical error, the results satisfy the free surface boundary conditions (4.2). The spatial regions, in which the numerical error of σ_{22} increases depends to the propagating Rayleigh wave. In Figure 6.2, the longitudinal wave part has already left the simulation domain, hence there is no numerical error in front of the Rayleigh wave, as it can be seen in Figure 6.1, where the longitudinal wave part is not completely apart from the transverse and Rayleigh part. How small the numerical error is, can be seen by comparing the numerical error of σ_{22} at $y = 0$ to the input signal $\sigma_{22}(0, 0, t) = \frac{QF(t)}{\Delta x}$ at $x = 0$, shown in Figure 6.3. Figure 6.1 and 6.2 show that the maximum of the numerical error of σ_{22} is $|\sigma_{22}| \approx 2 \times 10^{-9}$ and Figure 6.3

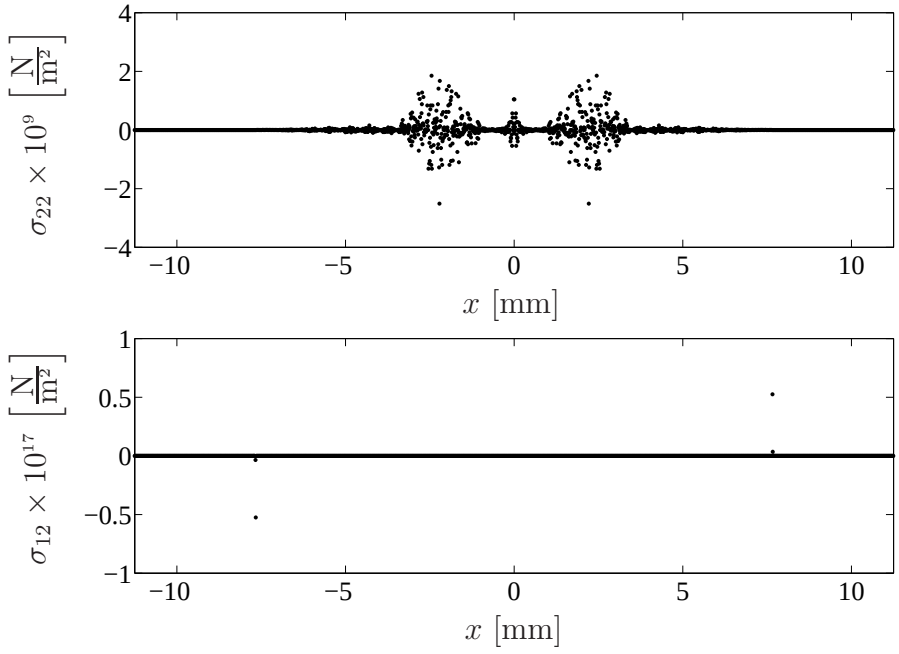

Figure 6.1: Evaluation of the compliance of the boundary condition of σ_{22} (top) and σ_{12} (bottom) at $t = 1.26\mu$s.

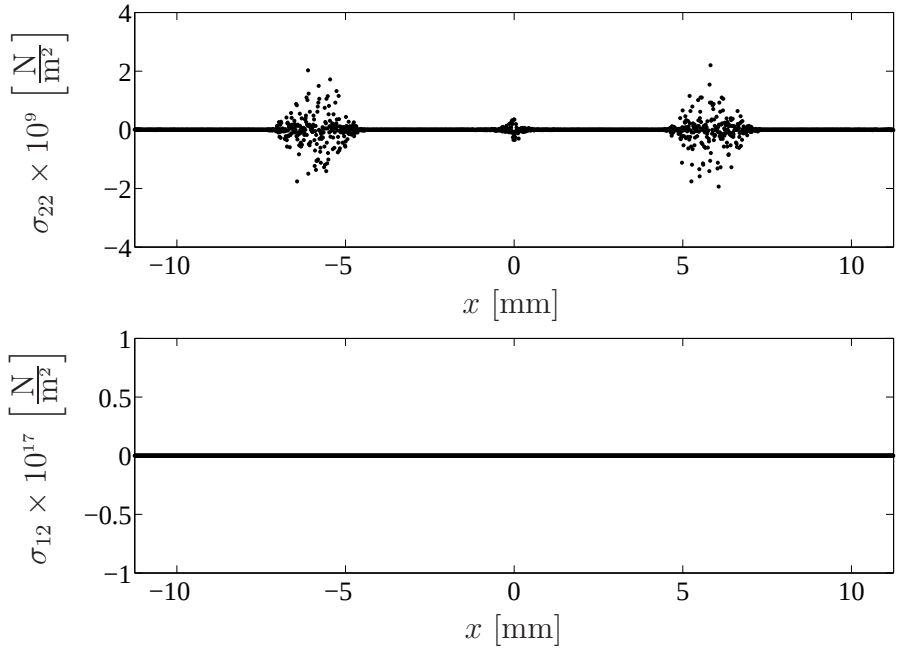

Figure 6.2: Evaluation of the compliance of the boundary condition of σ_{22} (top) and σ_{12} (bottom) at $t = 2.52\mu$s.

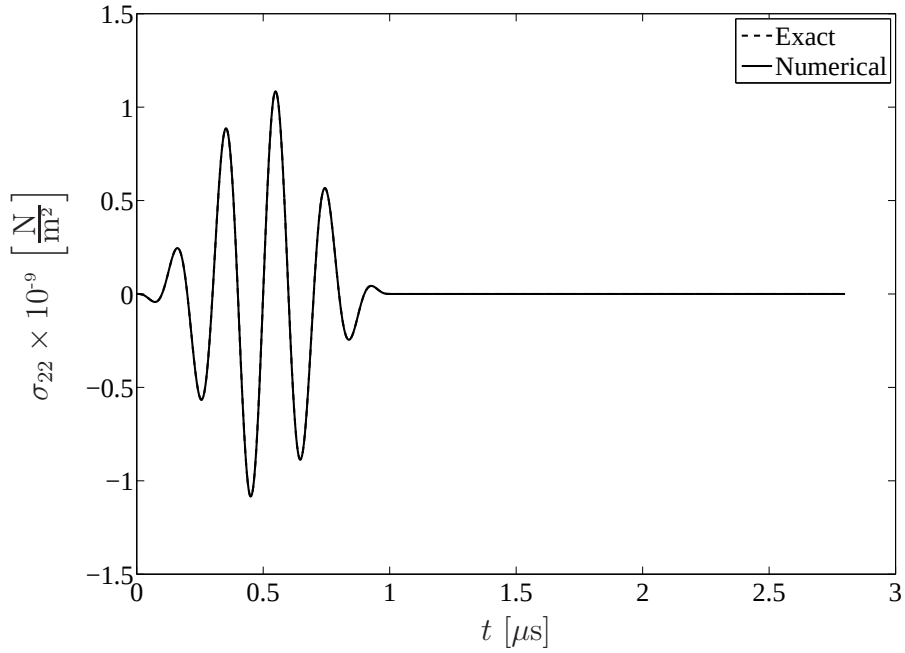

Figure 6.3: Numerical solution of $\sigma_{22}(0, 0, t)$ and exact input signal.

illustrates that the input signal has an amplitude of $Q = 1.1 \times 10^9$; thus it is clear that the numerical error is about 10^{18} times smaller as the input signal. Furthermore, Figure 6.3 shows the desired input signal in comparison to the simulated signal at $x = 0$ and $y = 0$. The exact signal and the numerical one are in good agreement.

As mentioned earlier, the numerical solution of the nonlinear half-space cannot be compared to an exact solution, since there exists no analytical solution at the present. But it is known, that the nonlinear solution does not differ very much from the linear solution [28] in the time domain. To illustrate this, the numerical solution of the particle velocities of propagating waves in an elastic half-space with linear and nonlinear response are compared. Figure 6.4 shows the particle velocity $\dot{v}(t)$ at $r = 5.2$mm and $\theta = 0°$. From the previous chapters it is clear that the particle velocity $\dot{u}$ is zero under the angle $\theta = 0°$.

The small amplitude wave right after the longitudinal wave part in Figure 6.4, depends to a wave propagating with the transverse wave speed. But this wave cannot be viewed

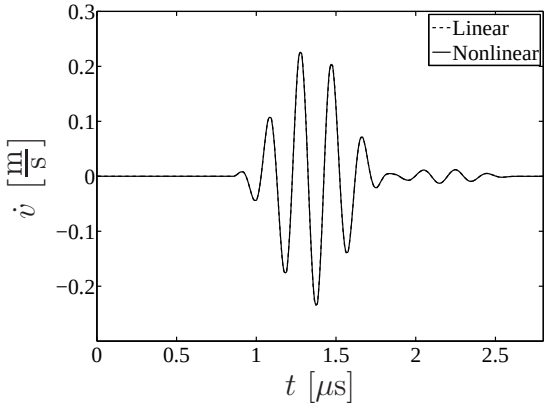

Figure 6.4: Numerical solution of the particle velocity $\dot{v}$ in linear and nonlinear media at $r = 5.2$mm and $\theta = 0°$.

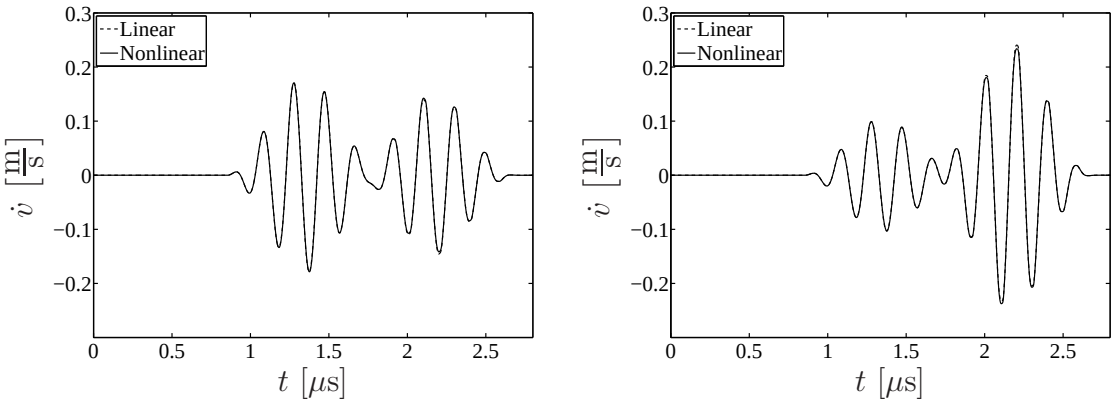

(a) Particle velocity $\dot{v}$ (b) Particle velocity $\dot{u}$

Figure 6.5: Numerical solution of the particle velocities in linear and nonlinear media at $r = 5.2$mm and $\theta = 30°$.

as a classical shear wave, since the particle movement is into the y-direction and thus into the propagation direction. It is rather due to reflections from the boundary, which can be viewed as a second source. This effect can be also observed in the analytical solution (see Figure 4.9). Nevertheless, this wave part is treated in the following as a transverse wave.

In Figures 6.5, 6.6 and 6.7 the particle velocities $\dot{v}$ and $\dot{u}$ for linear and nonlinear media are compared at $r = 5.2$mm and $\theta = 30°$, $60°$ and $89.5°$, respectively. Figures 6.4 - 6.7 show obviously that there can be rarely seen any difference between the time signals of the particle velocities in nonlinear and linear media; the same holds for the

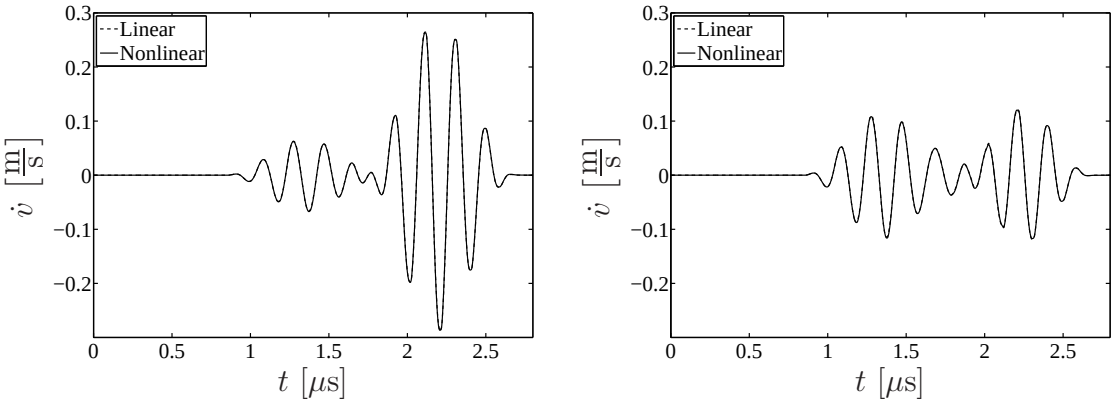

(a) Particle velocity $\dot{v}$ (b) Particle velocity $\dot{u}$

Figure 6.6: Numerical solution of the particle velocities in linear and nonlinear media at $r = 5.2$mm and $\theta = 60°$.

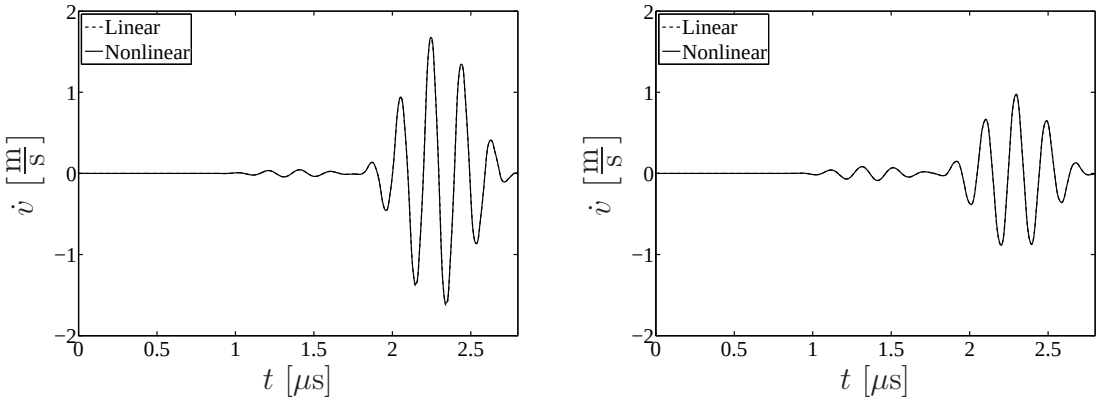

(a) Particle velocity $\dot{v}$ (b) Particle velocity $\dot{u}$

Figure 6.7: Numerical solution of the particle velocities in linear and nonlinear media at $r = 5.2$mm and $\theta = 89.5°$.

displacements and the stresses.

A view of the (x, y) simulation domain is given in Figure 6.8, wherein the propagating wave fronts of σ_{22} are illustrated at four different times, similar results are obtained for all other signals. At $t = t_1$ the excitation $F(t)$ is unequal zero, what can be clearly seen in the first subfigure. In all other subfigures, the excitation from the boundary is zero, so the dying out of the waves can be observed. The separation of the longitudinal and transverse wave parts has already taken place for $t = t_3$ and $t = t_4$. Moreover, the formation of the head wave can be followed in all subfigures.

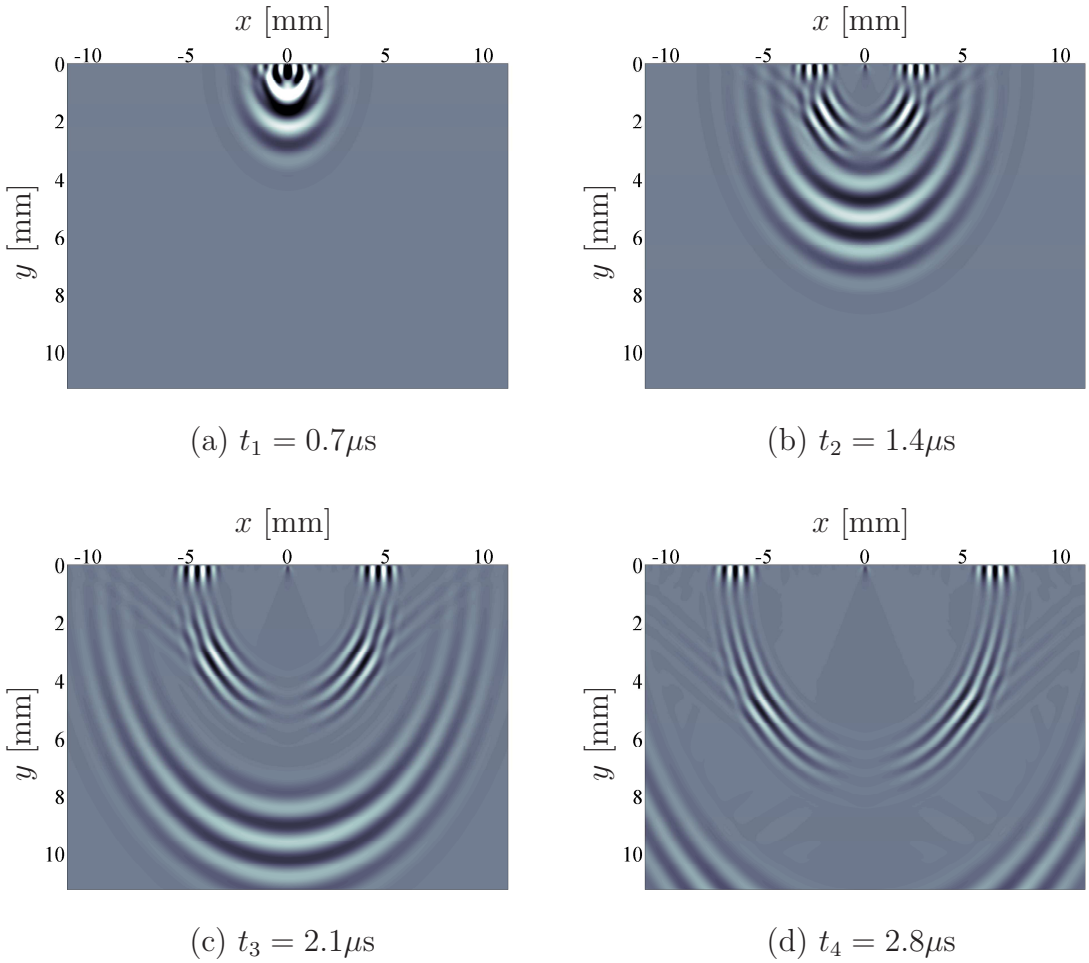

(a) $t_1 = 0.7\mu$s (b) $t_2 = 1.4\mu$s

(c) $t_3 = 2.1\mu$s (d) $t_4 = 2.8\mu$s

Figure 6.8: Propagating wave fronts of σ_{22} in a nonlinear elastic half-space at different fixed times.

Thus all expected waves - the longitudinal wave, the transverse wave, the head wave and the Rayleigh wave, which can be slightly seen at the free surface - occur in the half-space. The symmetry to the y-axis can be also observed, hence only the part for $x \geq 0$ is treated in the following.

The last subfigure shows additionally that the numerical boundaries have no effect on the simulation, since the longitudinal wave can leave the simulation domain without any impact.

6.2 Frequency-Domain

As described in Chapter 5, the FFT enables a better interpretation of time-harmonic signals in the frequency domain. Since the excitation signal used in this research is

a sinusoidal signal, the next section presents the obtained results in the frequency domain in order to get a better understanding of nonlinear wave propagation in an elastic half-space. First, the propagation of an one-dimensional plane wave, as introduced in Section 5.2.1, in quadratic nonlinear material is treated to introduce the acoustical nonlinearity parameter β. Subsequently, the achieved simulation results in two dimensions are investigated in the frequency domain. As it was already done in the last chapter, the FFT is always obtained by the particle velocities, since they offer the most undisturbed signals.

It has to be mentioned that the spatial discretization given in Table 6.1 allows only a fine resolution up to the second harmonic of the fundamental frequency $f_f = 5\text{MHz}$. The reason for this is that approximately 60 grids per wavelength are required to get a fine resolution in the frequency domain, as shown in Chapter 5. The spatial discretization, used in the following simulations, samples the fundamental frequency of the longitudinal wave with approximately 120 grids per wavelength and thus the second harmonic frequency with 60 grids per wavelength - the required minimum. The other higher harmonic frequencies are sampled with even less grids, therefore a fine resolution for these higher harmonic frequencies is not possible with this discretization. As shown in the last chapter, a fine resolution to higher frequencies can be reached by using a finer discretization, what results on the other hand in higher computational times. To avoid these higher computational times, only a frequency range of $0\text{MHz} \leq f \leq 12.5\text{MHz}$ is considered in the following. This is not a too strong limitation, since in practical applications of nonlinear wave propagation, for example in the NDE, most of the times only the signal intensity of the second harmonic frequency is compared to the signal intensity of the fundamental frequency to obtain important information about the material. The acoustical nonlinearity parameter β, introduced in the next section, depends also only on the signal intensity of the second harmonic and the fundamental frequency.

To get precise information from the analysis in the frequency domain, the longitudinal wave parts are extracted from the rest of the signals to avoid interferences between different waves in the two-dimensional simulations. Figure 6.8 shows that this is only possible after a certain propagation distance and for certain angles. The region in which this is possible are angles smaller than $\theta \approx 60°$, but the propagation distance still matters. The extraction of the longitudinal wave part is done by applying a Hanning window [21] over the desired part of the signal. The beginning and the end of the window for different propagation distances can be easily obtained using the longitudinal wave velocity. Hence, in the following only the longitudinal wave parts are considered. The transverse wave parts are not considered in the following, as the fundamental frequency of the transverse waves is only sampled with 60 grids per wavelength. A fine resolution in the interesting region of the second harmonic frequency would require a smaller spatial discretization.

6.2.1 One-Dimensional Wave Propagation

The governing equations of the one-dimensional plane wave propagation in linear media are given in Section 5.2.1. As in the case of two-dimensional wave propagation, the equations are basically the same, only the constitutive equation changes. The constitutive equation to model the quadratic nonlinear material in this section can be written as

$$\sigma_{22} \;=\; (\lambda + 2\mu)\,\frac{\partial v}{\partial y} + (l + 2m)\left(\frac{\partial v}{\partial y}\right)^2, \tag{6.1}$$

where $\sigma_{22} = \sigma_{22}\,(y,t)$. The simulation parameters are the same as for the nonlinear two-dimensional simulations and shown in Table 6.1 and 6.2. Only the amplitude Q of the input signal is different and given by $Q = 20 \times 10^6$, in order to compare the results to the linear one presented in the last chapter.

Figure 6.9 compares the FFT of the particle velocity $\dot{v}$ in a nonlinear material to the one in a linear material at $y = 10$mm.

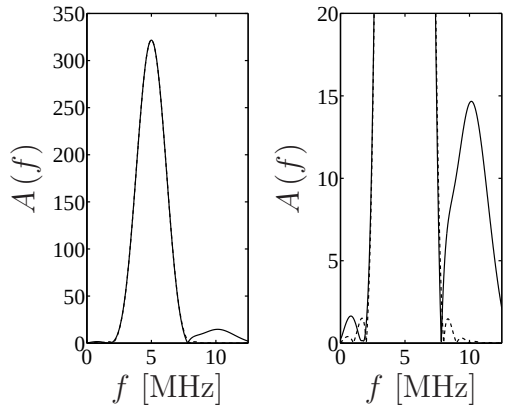

Figure 6.9: FFT of the particle velocity in nonlinear (solid) and linear (dashed) media at $y = 10$mm with zoom.

As expected, the magnitude at the fundamental frequency A_1 is in both cases approximately the same. In nonlinear material appears also a signal at the second harmonic frequency, which leads to a significant difference between wave propagation in linear and nonlinear materials as this is a pure nonlinear effect. The acoustical nonlinearity parameter β is defined by using this nonlinear phenomenon. Cantrell showed [6] that the factor of $\frac{A_2}{A_1^2}$ increases linearly with the propagation distance and thus

$$\frac{A_2}{A_1^2} \quad \propto \quad \beta y. \tag{6.2}$$

Furthermore β is a parameter which express the amount of nonlinearity in a material. In practical applications, it is often only possible to measure a relative β' [4], since the absolute value cannot be determined. Figure 6.10 shows the factor of $\frac{A_2}{A_1^2}$ of the particle velocity vs. the propagation distance from the simulation of a plane wave in nonlinear material, furthermore it clarifies the linear increase. The slope of this line can be used together with another material to calculate a relative β'.

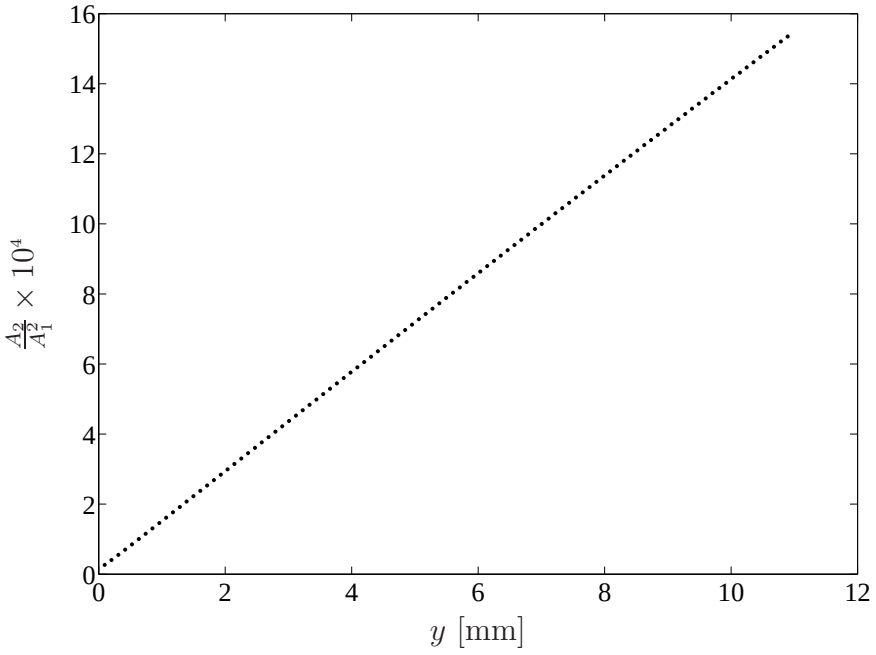

Figure 6.10: A_2/A_1^2 of the FFT of $\dot{v}$ over the propagation distance y.

6.2.2 Two-Dimensional Wave Propagation

In the following, the results of the numerical simulations of propagating waves in an elastic half-space with quadratic nonlinearity are presented in the frequency domain. As already noted, the signals in the frequency domain are obtained by the FFT of the particle velocities. In contrast to one-dimensional problems, two-dimensional problems require an analysis into the x- and y-direction in order to get all effects in the frequency domain. Thus, the particle velocities into the x- and y-direction, $\dot{u}$ and $\dot{v}$, are analyzed in the frequency domain. First the pure FFT signals are investigated, afterwards the dependency of $\frac{A_2}{A_1^2}$ to the propagation distance and the angle θ is studied in the x- and y-direction. At the end of the chapter, a parameter similar to the acoustical nonlinearity parameter β is introduced in order to analyze some material properties.

To show the differences in the frequency domain between propagating waves in linear

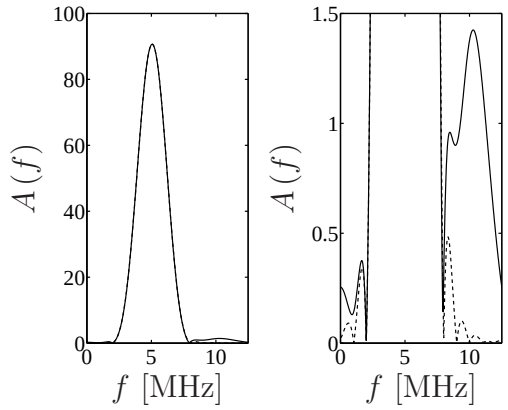

Figure 6.11: FFT of the particle velocity $\dot{v}$ in nonlinear (solid) and linear (dashed) material at $r = 5.2$mm and $\theta = 0°$ with zoom.

and nonlinear media, the FFT signals for different angles at a fixed radius are presented below. Figure 6.11 shows the FFT of the particle velocity $\dot{v}$ at $r = 5.2$mm and $\theta = 0°$.

As in the one-dimensional case, there can be rarely seen any difference in A_1, the magnitude of the signal at the fundamental frequency. The difference appears in A_2, the magnitude of the signal at the second harmonic frequency, where a peak in the signal of the nonlinear material arises. As mentioned in the last section, this is a pure nonlinear effect. The bifurcation in the second peak is due to a phase difference between the overlying wave parts [30], as they are not completely apart from each other at this propagation distance (see Figure 6.4).

Figure 6.12, 6.13 and 6.14 show the FFT of the particle velocities in x- and y-direction for $r = 5.2$mm and $\theta = 30°$, $60°$ and $89.5°$, respectively.

Again, in all figures the pure nonlinear effect of the appearance of a peak at the second harmonic frequency can be clearly seen. The bifurcations of the signal at the second harmonic frequency in Figure 6.12 and 6.13 are again due to the phase difference between the longitudinal and transverse wave parts. Moreover, a change in the signal intensity of the fundamental frequency, and in the nonlinear case also in the signal intensity of the second harmonic frequency, can be observed. The signal at $f = 0$MHz

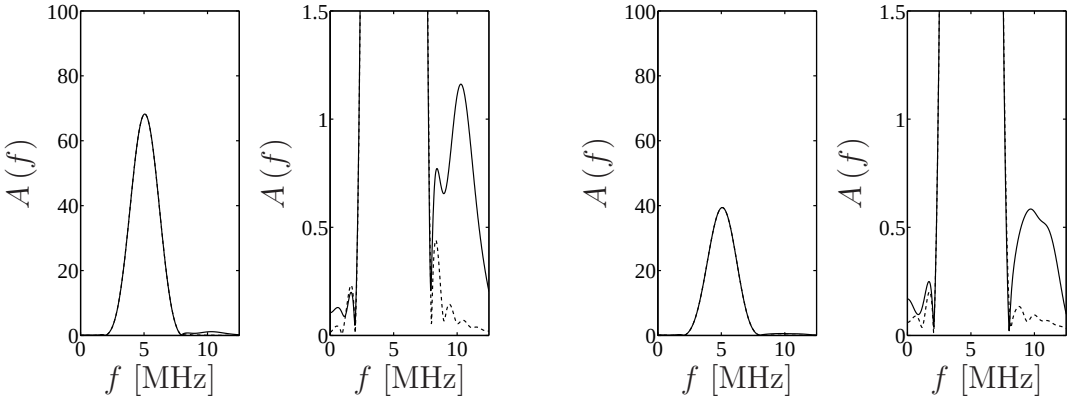

(a) FFT of $\dot{v}$ (b) FFT of $\dot{u}$

Figure 6.12: FFT of the particle velocities in nonlinear (solid) and linear (dashed) media at $r = 5.2$mm and $\theta = 30°$ with zoom.

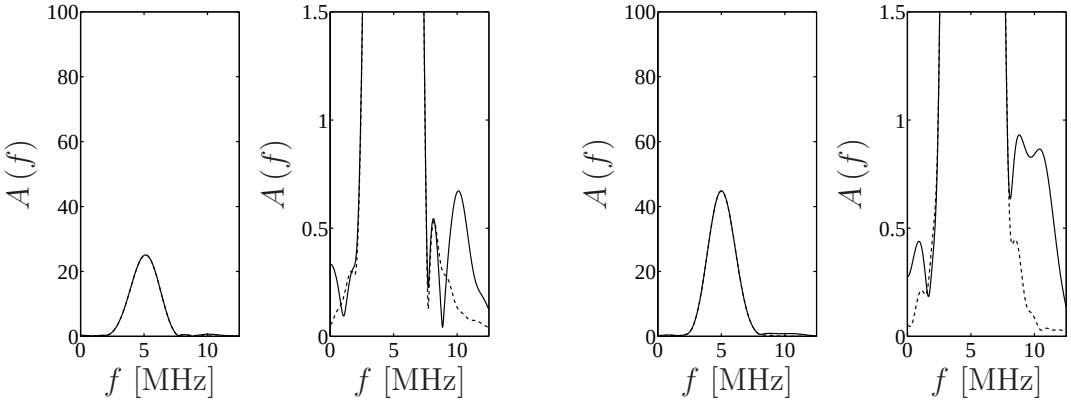

(a) FFT of $\dot{v}$ (b) FFT of $\dot{u}$

Figure 6.13: FFT of the particle velocities in nonlinear (solid) and linear (dashed) media at $r = 5.2$mm and $\theta = 60°$ with zoom.

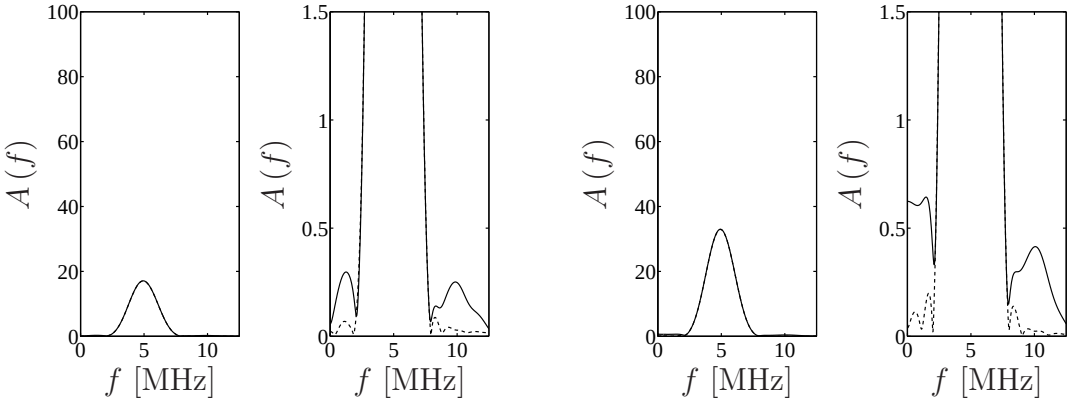

(a) FFT of $\dot{v}$ (b) FFT of $\dot{u}$

Figure 6.14: FFT of the particle velocities in nonlinear (solid) and linear (dashed) media at $r = 5.2$mm and $\theta = 89.5°$ with zoom.

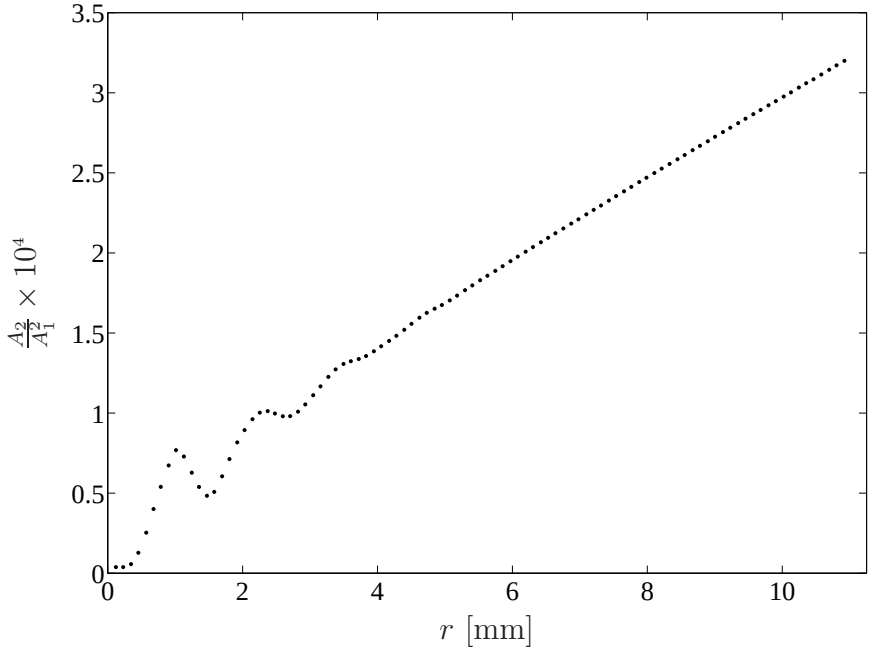

Figure 6.15: A_2/A_1^2 of the FFT of $\dot{v}$ over the propagation distance r at $\theta = 0°$.

in Figure 6.14 is attributed to the higher numerical error in the Rayleigh wave part (see Figure 5.23), as this numerical error is probably higher in the nonlinear case.

In [13] it is shown that the factor of $\frac{A_2}{A_1^2}$ also increases linearly under the consideration of spreading in the case of cylindrical acoustical waves, where only a longitudinal wave occurs. Hence, in the case of elastic waves, the factor $\frac{A_2}{A_1^2}$ is also supposed to changes linearly with propagation distance in regions, where the longitudinal wave part can be extracted completely from the transverse wave part.

This linear increase of $\frac{A_2}{A_1^2}$ in the case of two-dimensional elastic waves is illustrated in Figure 6.15, showing $\frac{A_2}{A_1^2}$ of the numerical solution of $\dot{v}$ at $\theta = 0°$ over the propagation distance r. Especially at this angle, the problem is almost the same as for acoustical waves, as there occurs only a low amplitude transverse wave part.

The small ripples for a propagation distance of $r \leq 6$mm are due to the fact that the longitudinal wave part is not completely apart from the transverse wave part. Thus, there cannot be said anything about the behavior of $\frac{A_2}{A_1^2}$. But in the region, where

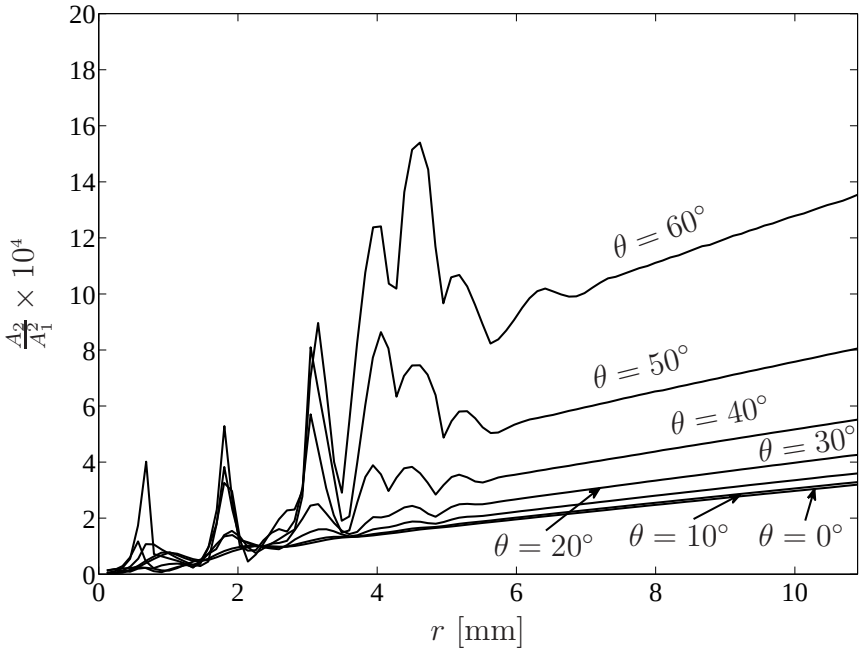

Figure 6.16: A_2/A_1^2 of the FFT of $\dot{v}$ over the propagation distance r for different θ.

the longitudinal wave can be extracted from the transverse wave, the expected linear increase in Figure 6.15 is obvious. Figure 6.16 shows the dependency of $\frac{A_2}{A_1^2}$ of $\dot{v}$ vs. the propagation distance from the angle θ. Only the region of $\theta \leq 60°$ is considered, since the longitudinal wave and the head wave are overlying for higher angles (see Figure 6.8) and thus an extraction of the longitudinal wave part is not possible.

It shows clearly the angular dependency of $\frac{A_2}{A_1^2}$ vs. the propagation distance. Not only the absolute value of the curves are different, but also the slopes of the curve in the part of linear increase differ. The region in which a linear increase occurs depends also on the angle, this is due to the fact that the influence of the transverse wave part differs with the angle. The same phenomenon can be observed for the particle velocity $\dot{u}$ into the x-direction, shown in Figure 6.17. In this figure, only angles for $10° \leq \theta \leq 60°$ are considered, as for angles below that range, the occurrence of a displacement in x-direction is so small that it can be neglected; for angles above this range, the transverse wave part dominates as discussed previously.

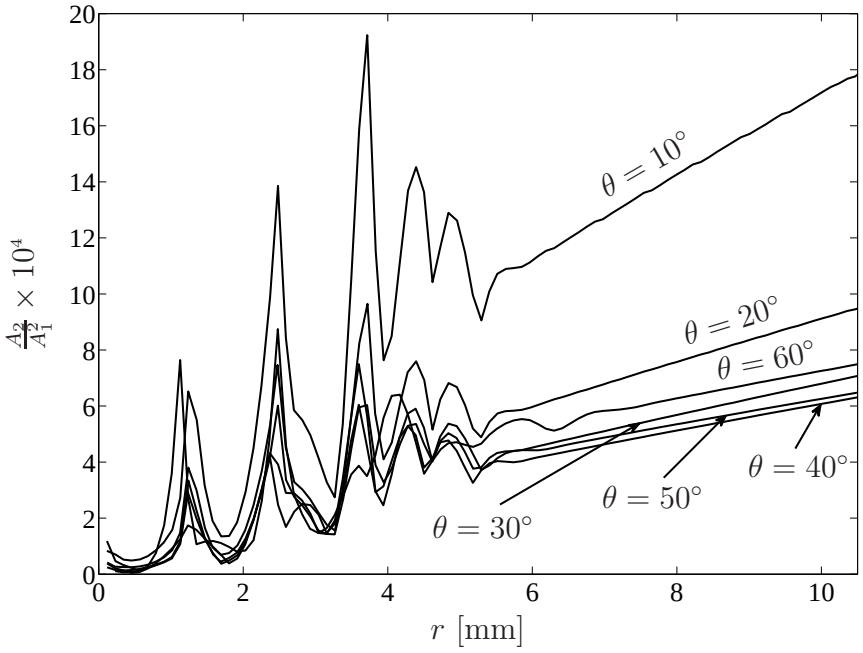

Figure 6.17: A_2/A_1^2 of the FFT of $\dot{u}$ over the propagation distance r for different θ.

Herein, the slopes of the curves differ also with the angle. Comparing Figure 6.17 with Figure 6.16 visualizes that the slopes of the linear parts for a certain angle differ in both figures. This is clear, as the longitudinal wave part depends differently on $\dot{v}$ and $\dot{u}$ at different angles. To compare different materials, it is from high interest, how the slopes in Figure 6.16 and Figure 6.17 changes with the angle and also with the material. Thus, two parameters κ_y and κ_x, which are similar to the acoustical nonlinearity parameter β (6.2), are introduced. Let κ_y and κ_x be the slopes in the linear increasing part of the curves determined by $\frac{A_2}{A_1^2}$ vs. the propagation distance for the particle velocity $\dot{v}$ and $\dot{u}$, respectively. Hence, these parameters are defined as

$$\begin{aligned} \kappa_y r &= \tfrac{A_2}{A_1^2} \quad \text{with } A_1 \text{ and } A_2 \text{ from the FFT of } \dot{v}, \\ \kappa_x r &= \tfrac{A_2}{A_1^2} \quad \text{with } A_1 \text{ and } A_2 \text{ from the FFT of } \dot{u}, \end{aligned} \tag{6.3}$$

where the factor $\frac{A_2}{A_1^2}$ is only considered in the region where the longitudinal wave can be completely extracted from the transverse part and therefore a linear increase takes place.

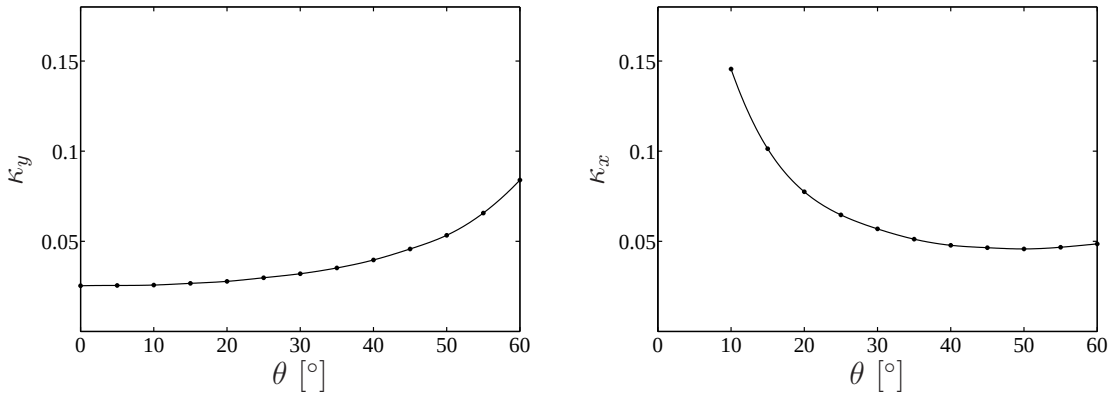

(a) κ_y (b) κ_x

Figure 6.18: κ_y and κ_x over the angle θ together with a best fit curve.

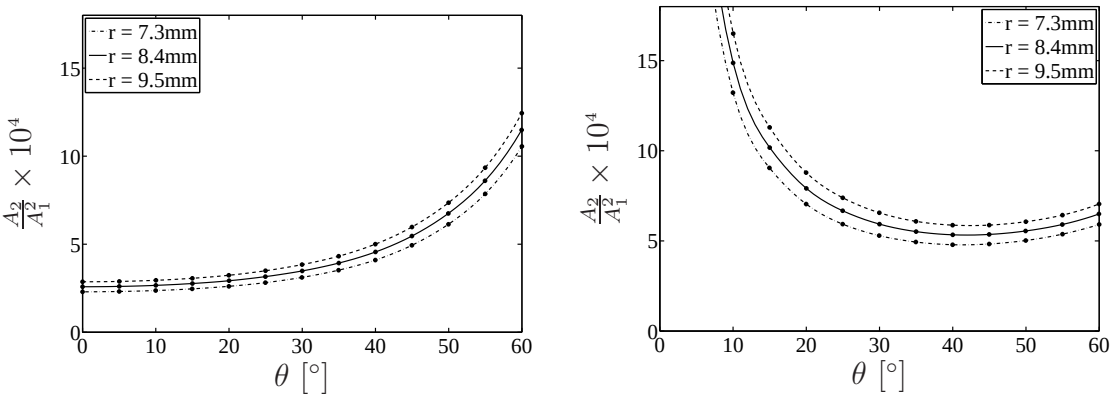

(a) Particle velocity $\dot{v}$ (b) Particle velocity $\dot{u}$

Figure 6.19: A_2/A_1^2 of the FFT of the particle velocities over the angle θ for different r.

Figure 6.18 shows the values of κ_y and κ_x over the angle θ. Again, only angles of $\theta \leq 60°$ are considered.

Both curves show the angular dependency of κ_y and κ_x. For κ_y a significant change arises not until $\theta \approx 20°$, in contrast to that, κ_x is more sensitive for low angles and less sensitive for higher angles.

Another point of interest is how the values of $\frac{A_2}{A_1^2}$ changes over the angle θ for a fixed radius. Figure 6.19 illustrates this relationship, the shape of these curves is the same as in Figure 6.18, which is clear from equation (6.3).

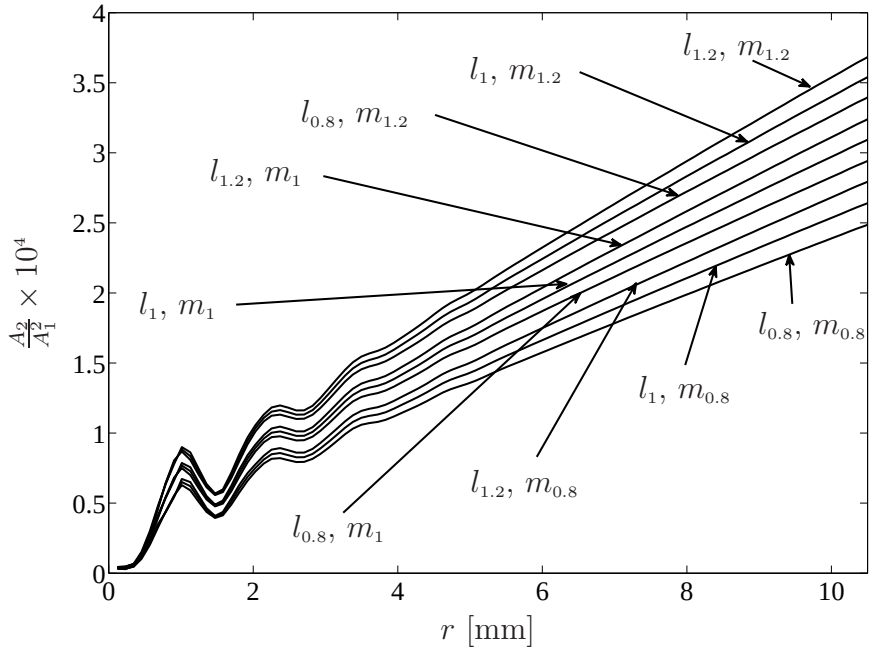

Figure 6.20: A_2/A_1^2 of the FFT of $\dot{v}$ over r at $\theta = 0°$ for different l and m.

The fact that the curves in Figure 6.18 and 6.19 are increasing for κ_y and accordingly for $\dot{v}$ while decreasing for κ_x and $\dot{u}$, reflects the inversely proportional participation to the longitudinal wave part over the angle θ.

To investigate how the parameters κ_x and κ_y change with different material properties, the third-order elastic constants l and m are varied in the following simulations. The values of l and m used to study the material properties are in the range of $0.8l_{\mathrm{Al}} \leq l \leq 1.2l_{\mathrm{Al}}$ and $0.8m_{\mathrm{Al}} \leq m \leq 1.2m_{\mathrm{Al}}$, where l_{Al} and m_{Al} are the values of Aluminum D54S given in Table 6.2. In the following, the different third-order elastic constants are denoted by l_{a} and m_{b}, where $l_{\mathrm{a}} = \mathrm{a}l_{\mathrm{Al}}$ and $m_{\mathrm{b}} = \mathrm{b}m_{\mathrm{Al}}$.

Figure 6.20, 6.21 and 6.22 show the factor $\frac{A_2}{A_1^2}$ of $\dot{v}$ vs. the propagation distance for $\theta = 0°$, $30°$ and $60°$, respectively. All the figures show obviously the influence of the third-order elastic constants on the behavior of $\frac{A_2}{A_1^2}$ vs. the propagation distance. For $\theta = 0°$ and $30°$, the parameter m has a stronger influence on the results than l, as

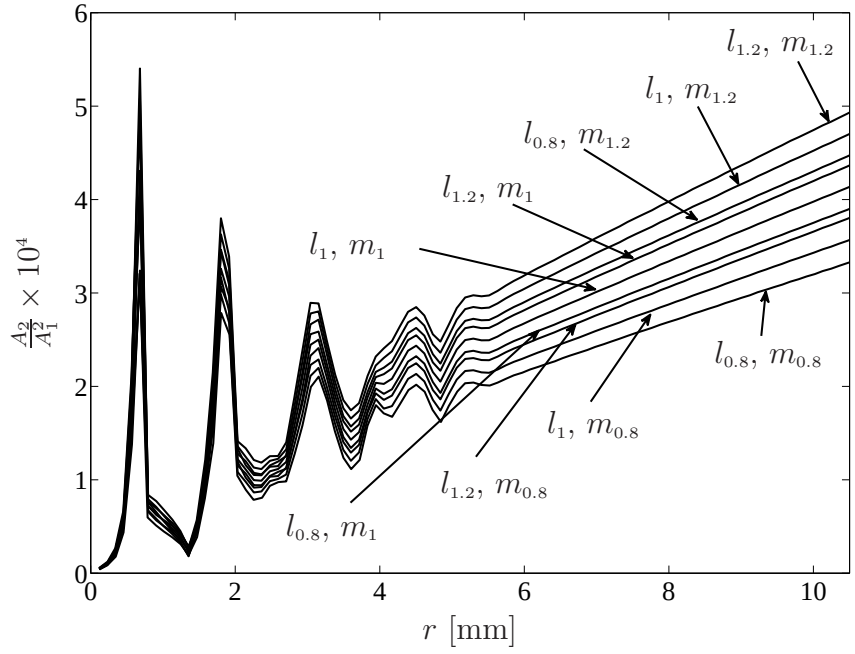

Figure 6.21: A_2/A_1^2 of the FFT of $\dot{v}$ over r at $\theta = 30°$ for different l and m.

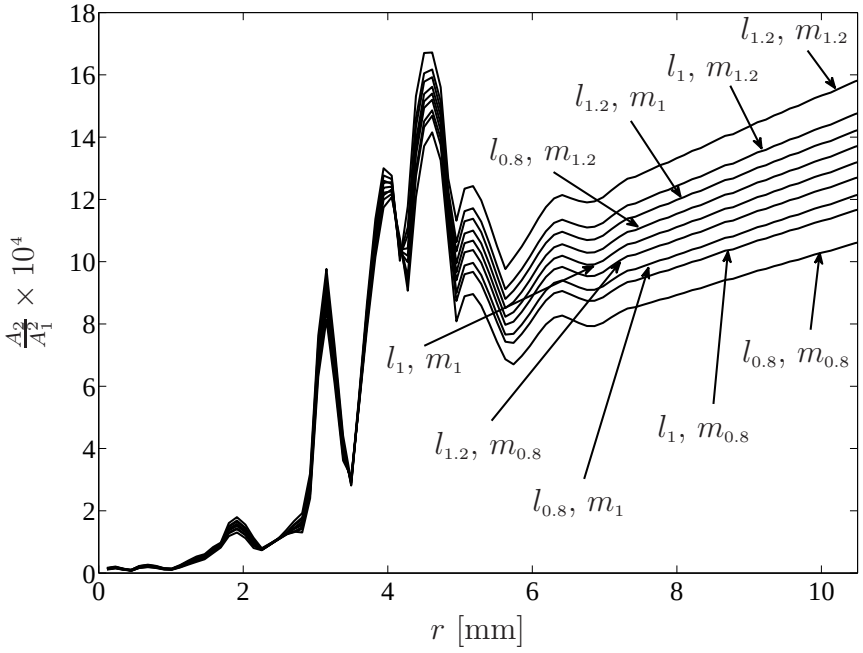

Figure 6.22: A_2/A_1^2 of the FFT of $\dot{v}$ over r at $\theta = 60°$ for different l and m.

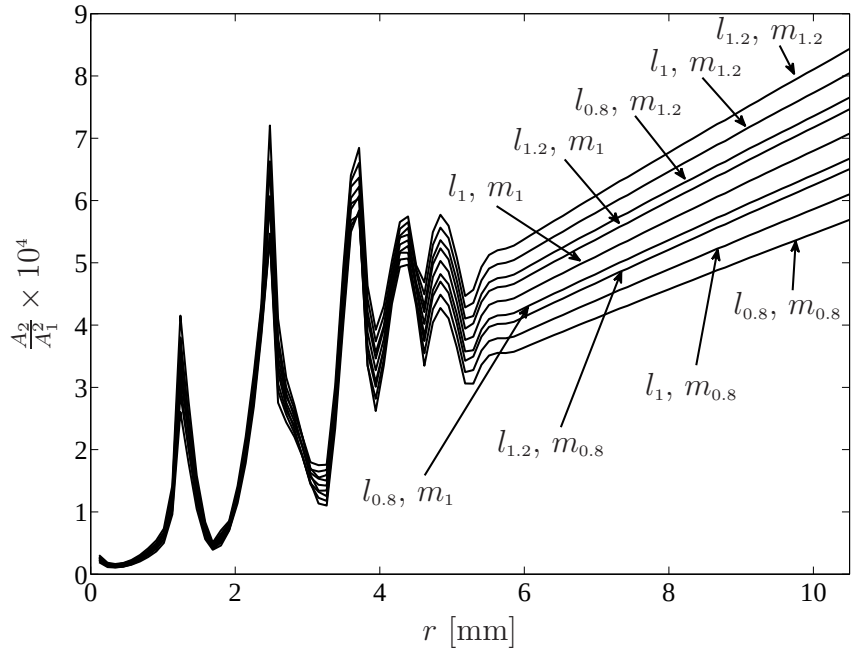

Figure 6.23: A_2/A_1^2 of the FFT of $\dot{u}$ over r at $\theta = 30°$ for different l and m.

this parameter determines mostly which curve has a bigger slope (in the linear part). In Figure 6.21 the influence of m is decreasing and the one of l is increasing, because the curves of $l_{0.8}, m_{1.2}$ and $l_{1.2}, m_1$ as well as $l_{0.8}, m_1$ and $l_{1.2}, m_{0.8}$ are moving closer to each other. For $\theta = 60°$, the influence of l is higher than the one of m, as the curves of $l_{0.8}, m_{1.2}$ and $l_{1.2}, m_1$ as well as $l_{0.8}, m_1$ and $l_{1.2}, m_{0.8}$ in Figure 6.22 changed their position in comparison to Figure 6.20 and 6.21.

The same behavior can be observed for $\frac{A_2}{A_1^2}$ of $\dot{u}$ vs. the propagation distance as given in Figure 6.23 and 6.24, showing the results for $\theta = 30°$ and $60°$, respectively.

The angular dependency of the influence of l and m is illustrated in Figure 6.25 and 6.26, giving $\frac{A_2}{A_1^2}$ of $\dot{v}$ and $\dot{u}$ vs. θ at $r = 8.4$mm, respectively. In both figures it can be seen that the curves of $l_{0.8}, m_{1.2}$ and $l_{1.2}, m_1$ as well as $l_{0.8}, m_1$ and $l_{1.2}, m_{0.8}$, cross each other at $\theta \approx 40°$. Thus the influence of m on the longitudinal wave is higher than the one of l for $0° \leq \theta \leq 40°$ and for $40° \leq \theta \leq 90°$ it is vice versa.

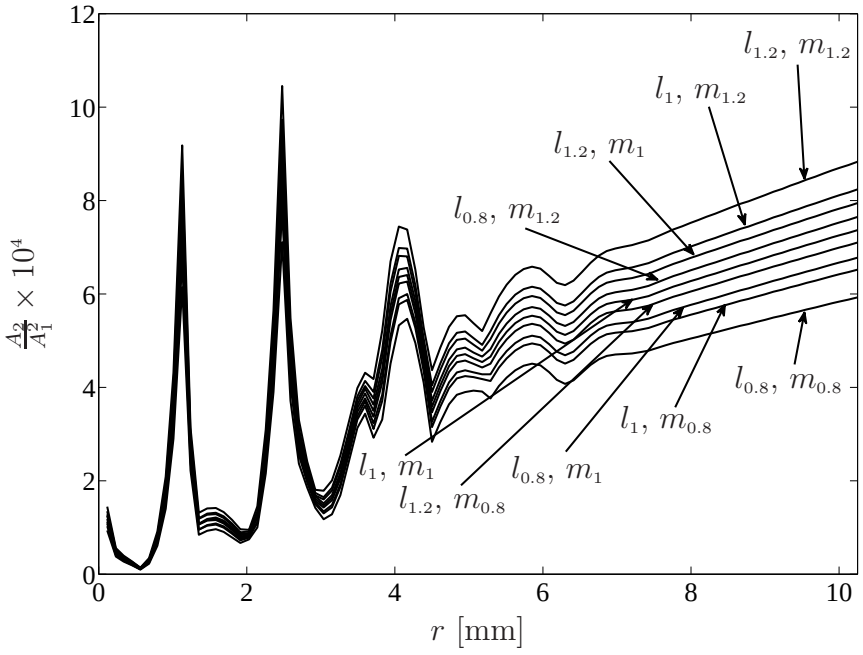

Figure 6.24: A_2/A_1^2 of the FFT of $\dot{u}$ over r at $\theta = 60°$ for different l and m.

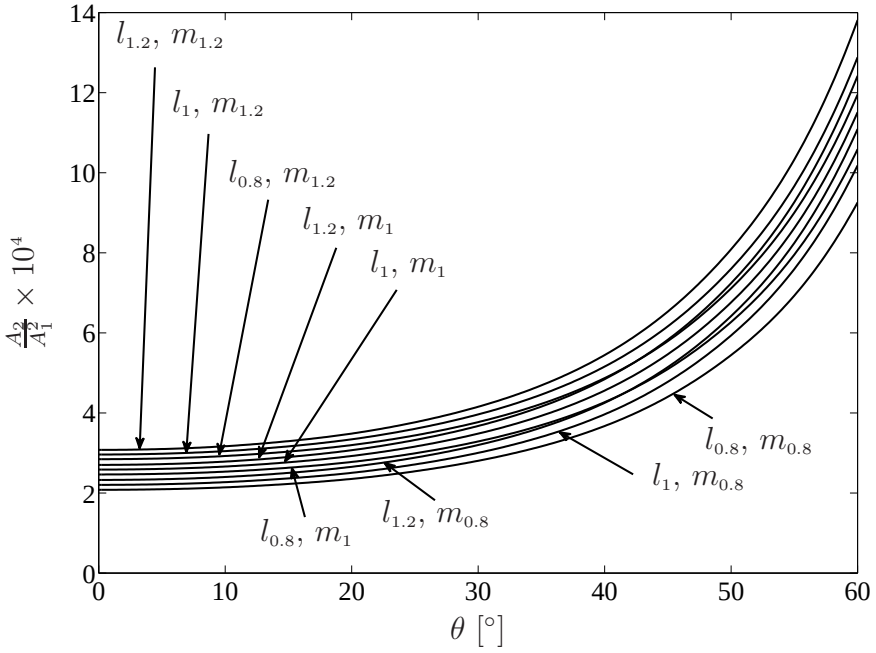

Figure 6.25: A_2/A_1^2 of the FFT of $\dot{v}$ over θ at $r = 8.4$mm for different l and m.

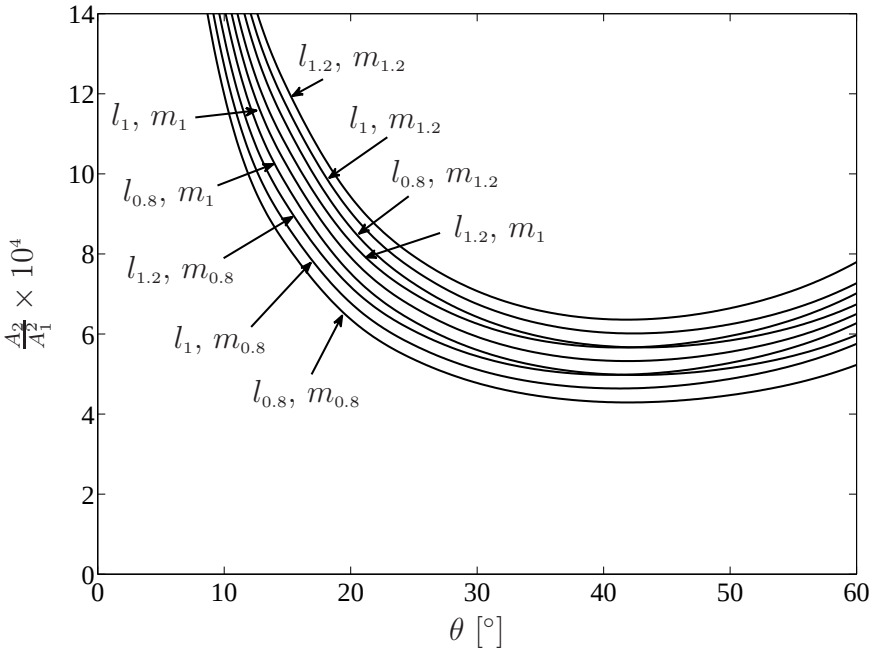

Figure 6.26: A_2/A_1^2 of the FFT of $\dot{u}$ over θ at $r = 8.4$mm for different l and m.

A more precise look on the influence of the third-order elastic constants is possible by using the parameters κ_x and κ_y. To compare the effects on κ_x and κ_y to the variation of the third-order elastic constants a relative parameters $\kappa_x^{'}$ and $\kappa_y^{'}$ are introduced, thus

$$\begin{aligned} \kappa_x^{'} &= \frac{\kappa_x}{\kappa_{x(\mathrm{Al})}}, \\ \kappa_y^{'} &= \frac{\kappa_y}{\kappa_{y(\mathrm{Al})}}, \end{aligned} \tag{6.4}$$

where $\kappa_{x(\mathrm{Al})}$ and $\kappa_{y(\mathrm{Al})}$ are the values of Aluminum D54S, given in Figure 6.18. Figure 6.27 and 6.28 represent the angular dependency of $\kappa_y^{'}$ and $\kappa_x^{'}$, respectively. Both figures show clearly that the influence of m on the longitudinal wave part is higher than the one for l for $\theta < 40°$ and vice versa for $\theta > 40°$. Furthermore both figures feature a symmetry to $\kappa^{'} = 1$, hence the values of $\kappa_x^{'}$ and $\kappa_y^{'}$ (and therefore also the values of κ_x and κ_y) form for a fixed angle θ a plate in the (l, m)-domain. Figure 6.29 depicts such a plate exemplary for $\kappa_y^{'}$ at $\theta = 0°$.

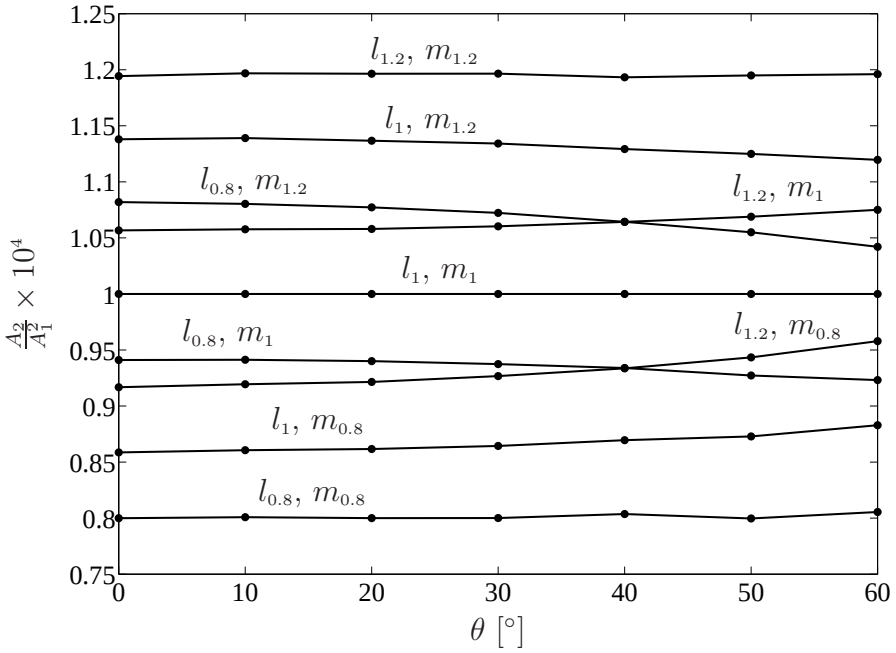

Figure 6.27: $\kappa_y^{'}$ over the angle θ for different l and m.

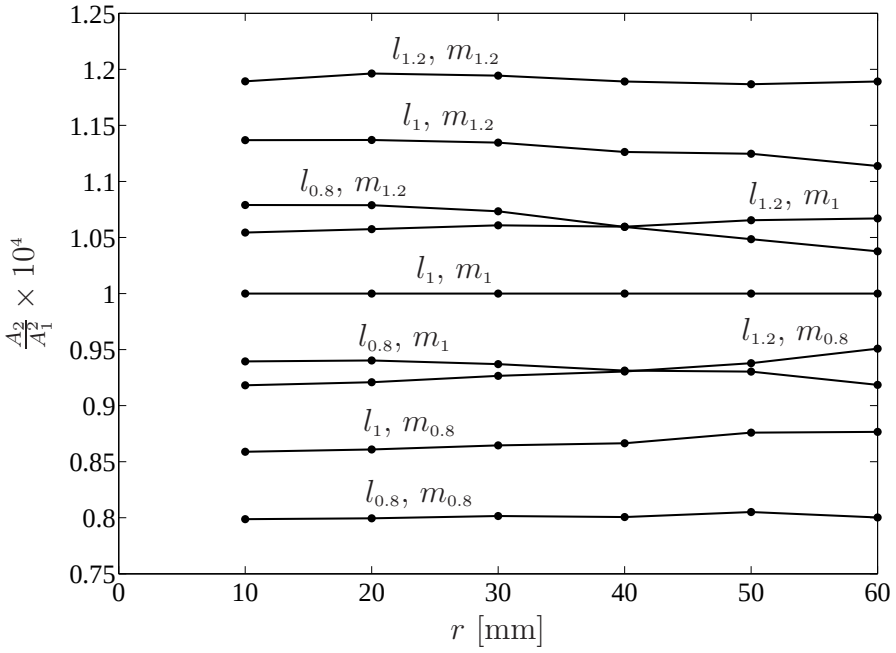

Figure 6.28: $\kappa_y^{'}$ over the angle θ for different l and m.

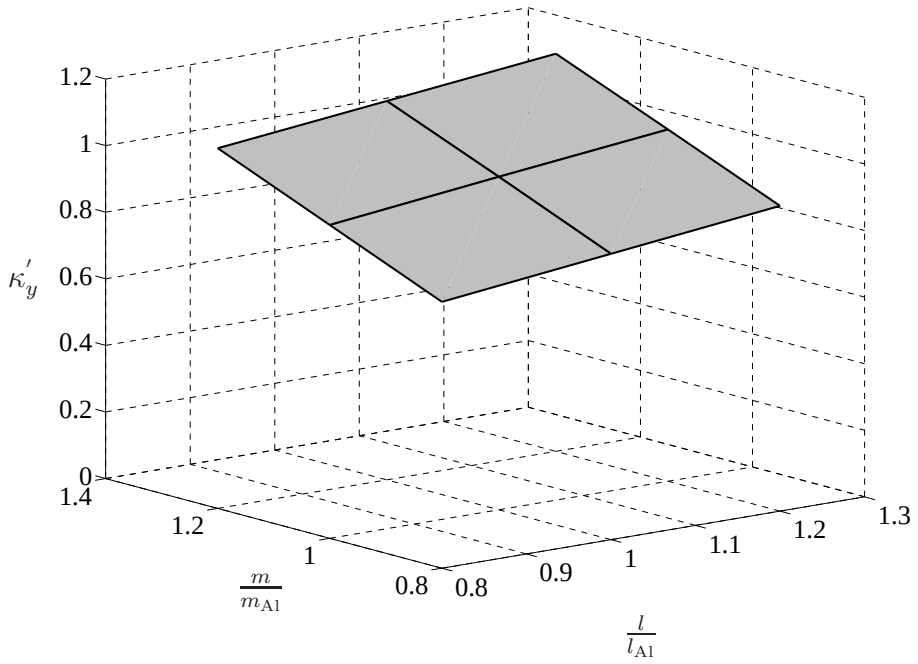

Figure 6.29: κ_y' in dependence on different l and m at $\theta = 0°$.

To sum up, the obtained results of the numerical simulation of propagating waves in an elastic half-space with quadratic nonlinearity can be used to get more understanding about two-dimensional wave propagation in nonlinear materials. It was shown that the signals in the time-domain do not differ very much from the one obtained from simulating wave propagation in linear material. But the frequency domain allows to see the differences between linear and nonlinear material. Hence, the frequency domain can be used to investigate the dependents of the nonlinearity in the signals on the location in the half-space as well on the material properties.

CHAPTER VII

CONCLUSION AND OUTLOOK

This research demonstrates the effectiveness of using a numerical solution approximation with a central scheme approach to analyze wave propagation in an elastic half-space with quadratic nonlinearity. Specifically, this research uses an efficient numerical solver to analyze nonlinear effects that appear in harmonic waves propagating in nonlinear media.

The solver implemented in this study is independent of the eigenstructure of the system under consideration, so it can be used for different linear and nonlinear systems. Moreover, the solution approximation to the original Lamb's problem obtained by the solver is in good agreement with the exact analytical solution. Furthermore, the numerical solver provides a high resolution of the nonlinear effects that evolve during wave propagation in nonlinear media. It has been shown that the signal intensity of the second higher harmonic frequency in comparison to the signal intensity of the fundamental frequency can be exploited to characterize the amount of nonlinearity in the material. Additionally, it is presented that in the two-dimensional case the nonlinear effects in the material depend on the location of the received signal in the elastic half-space. There is also a difference in the nonlinearity between the wave velocities in x- and y-direction, which depends as well on the location in the half-space. To quantify these dependency, two parameters κ_x and κ_y are introduced, which are similar to the acoustical nonlinearity parameter β, as they depend on the behavior of $\frac{A_2}{A_1^2}$ of the FFT of a signal over the propagation distance. These parameters are also used to compare different material properties and to investigate how the nonlinear effects change with the third-order elastic constants. In connection with this

investigation it is shown that the different third-order elastic constants have stronger and weaker influence on the nonlinear effects in different regions inside the half-space. These regions depend mainly on the angle θ.

All studies on nonlinear effects in the elastic half-space with quadratic nonlinearity are based on the evaluation of the longitudinal wave parts, therefore these parts are extracted from the other wave parts. One reason for this procedure is that a finer spatial discretization is required to investigate the transverse waves in the regions of the second harmonic. The study of the transverse wave parts is a subject for further research in order to gain more information about the behavior of propagating waves in nonlinear elastic media.

In this research constant material properties in the whole half-space are assumed. But in many practical applications the material properties are not constant in the whole specimen. In the NDE, for example, cracks and microdamages exhibit different properties than undamaged parts of the material. Hence, it is from great interest how the propagating waves are influenced when traveling through cracks or microdamages. A numerical study of these effects arising from cracks and microdamages in materials is also a topic of further research.

Because this research is a pure numerical study, an experimental study of propagating waves in an elastic half-space with quadratic nonlinearity has to be done in order to confirm the obtained results for practical use. This is also of interest, as the used mathematical model neglects some real physical effects, such as attenuation. To investigate this attenuation effects a detailed experimental and numerical study is necessary.

APPENDIX A

DISPLACEMENT POTENTIALS

The displacement potentials are derived in the following. First, the general three-dimensional case is treated, thereafter the equations are simplified to get the two-dimensional case used in Chapter 4.

A.1 In Three-Dimensions

In the absence of body forces, the general three-dimensional displacement equations of motion can be written [2] as

$$\sigma_{ij,j} = \rho\ddot{u}_i, \tag{A.1}$$

where the summation convention is implied, as usual. The linear constitutive equations in the general three-dimensional case are given by

$$\sigma_{ij} = \lambda\varepsilon_{kk}\delta_{ij} + 2\mu\varepsilon_{ij}, \tag{A.2}$$

where δ_{ij} denotes the Kronecker delta symbol and ε the strain-tensor

$$\varepsilon_{ij} = \frac{1}{2}\left(u_{i,j} + u_{j,i}\right). \tag{A.3}$$

Together with (A.2) and (A.3), the displacement equations of motion (A.1) can be written as

$$\mu u_{i,jj} + (\lambda + \mu)\, u_{j,ji} = \rho\ddot{u}_i. \tag{A.4}$$

In vector notation the displacement equations of motion (A.4) can be expressed as

$$\mu\nabla^2\mathbf{u} + (\lambda + \mu)\,\nabla\nabla\cdot\mathbf{u} = \rho\ddot{\mathbf{u}}, \tag{A.5}$$

where

$$\begin{aligned} \nabla \mathbf{f} &= f_{i,i} \qquad \text{(divergence)}, \\ \nabla f &= f_{,i}\vec{e}_i \qquad \text{(gradient)}, \\ \nabla^2 \mathbf{f} &= f_{i,jj}\vec{e}_i \qquad \text{(Laplace operator)}. \end{aligned}$$

Considering a decomposition of the displacement vector of the form

$$\mathbf{u} = \nabla\phi + \nabla \wedge \boldsymbol{\psi}, \tag{A.6}$$

where

$$\nabla \wedge \mathbf{f} = (f_{z,y} - f_{y,z})\,\vec{e}_x + (f_{x,z} - f_{z,x})\,\vec{e}_y + (f_{y,x} - f_{x,y})\,\vec{e}_z \qquad \text{(curl)}.$$

Substitution of the displacement representation (A.6) into equation (A.5) yields

$$\mu\nabla^2\left[\nabla\phi + \nabla \wedge \boldsymbol{\psi}\right] + (\lambda+\mu)\,\nabla\nabla\cdot\left[\nabla\phi + \nabla \wedge \boldsymbol{\psi}\right] = \rho\frac{\partial^2}{\partial t^2}\left[\nabla\phi + \nabla \wedge \boldsymbol{\psi}\right]. \tag{A.7}$$

Since $\nabla\cdot\nabla\phi = \nabla^2\phi$ and $\nabla\cdot\nabla\wedge\boldsymbol{\psi} = 0$ [5], equation (A.7) can be rearranged to

$$\nabla\left[(\lambda+2\mu)\,\nabla^2\phi - \rho\ddot{\phi}\right] + \nabla \wedge \left[\mu\nabla^2\boldsymbol{\psi} - \rho\ddot{\boldsymbol{\psi}}\right] = 0. \tag{A.8}$$

Clearly, the displacement representation (A.6) satisfies the equation of motion if

$$\nabla^2\phi = \frac{1}{c_l^2}\ddot{\phi} \tag{A.9}$$

and

$$\nabla^2\boldsymbol{\psi} = \frac{1}{c_t^2}\ddot{\boldsymbol{\psi}}, \tag{A.10}$$

where

$$c_l^2 = \frac{\lambda+2\mu}{\rho} \quad \text{and} \quad c_t^2 = \frac{\mu}{\rho}. \tag{A.11}$$

It has to be noted that equation (A.6) relates the three components of the displacement vector to four other functions: the scalar potential and the three components

of the vector potential. This indicates that ϕ and the components of $\boldsymbol{\psi}$ should be subjected to an additional constraint condition. Generally the components of $\boldsymbol{\psi}$ are taken to be related in some manner. Usually, but not always, the relation

$$\nabla \cdot \boldsymbol{\psi} \;=\; 0$$

is taken as the additional constraint condition [2].

From equation (A.6) it follows that

$$\begin{aligned} u &= \frac{\partial \phi}{\partial x} + \frac{\partial \psi_z}{\partial y} - \frac{\partial \psi_y}{\partial z}, \\ v &= \frac{\partial \phi}{\partial y} - \frac{\partial \psi_z}{\partial x} + \frac{\partial \psi_x}{\partial z}, \\ w &= \frac{\partial \phi}{\partial z} + \frac{\partial \psi_y}{\partial x} - \frac{\partial \psi_x}{\partial y}. \end{aligned} \tag{A.12}$$

A.2 In Two-Dimensions

In the two-dimensional case the displacement vector and the ∇-operator are in the (x, y)-plane and consequently the vector potential $\boldsymbol{\psi}$ is directed normal to the (x, y)-plane, hence

$$\boldsymbol{\psi} \;=\; \psi_z \vec{e}_z \tag{A.13}$$

and equation (A.12) simplifies to

$$\begin{aligned} u &= \frac{\partial \phi}{\partial x} + \frac{\partial \psi_z}{\partial y}, \\ v &= \frac{\partial \phi}{\partial y} - \frac{\partial \psi_z}{\partial x}. \end{aligned} \tag{A.14}$$

Together with (A.13), the displacement equations of motion in form of potentials (A.9) and (A.10) reduce in the two-dimensional case to

$$\frac{\partial^2 \phi}{\partial x^2} + \frac{\partial^2 \phi}{\partial y^2} \;=\; \frac{1}{c_l^2} \frac{\partial^2 \phi}{\partial t^2} \tag{A.15}$$

and

$$\frac{\partial^2 \psi_z}{\partial x^2} + \frac{\partial^2 \psi_z}{\partial y^2} = \frac{1}{c_t^2} \frac{\partial^2 \psi_z}{\partial t^2}. \tag{A.16}$$

Furthermore, the constitutive equations (A.2) reduce in the two-dimensional case to

$$\begin{aligned} \sigma_{11} &= (\lambda + 2\mu) \frac{\partial u}{\partial x} + \lambda \frac{\partial v}{\partial y} \\ \sigma_{22} &= (\lambda + 2\mu) \frac{\partial v}{\partial y} + \lambda \frac{\partial u}{\partial x} \\ \sigma_{12} &= \mu \left(\frac{\partial u}{\partial y} + \frac{\partial v}{\partial x} \right). \end{aligned} \tag{A.17}$$

By substituting (A.14) into (A.17) and using (A.15), (A.16), the stresses may be written in terms of the displacement potentials as

$$\begin{aligned} \sigma_{11} &= \frac{\lambda}{c_l^2} \ddot{\phi} + 2\mu \left(\frac{\partial^2 \phi}{\partial x^2} + \frac{\partial^2 \psi_z}{\partial x \partial y} \right), \\ \sigma_{22} &= \frac{\lambda}{c_l^2} \ddot{\phi} + 2\mu \left(\frac{\partial^2 \phi}{\partial y^2} - \frac{\partial^2 \psi_z}{\partial x \partial y} \right), \\ \sigma_{12} &= \mu \left(-\frac{1}{c_t^2} \ddot{\psi}_z + 2 \left(\frac{\partial^2 \phi}{\partial x \partial y} + \frac{\partial^2 \psi_z}{\partial y^2} \right) \right). \end{aligned} \tag{A.18}$$

APPENDIX B

ONE-DIMENSIONAL WAVE EQUATION

This chapter derives the analytical solution for the one-dimensional BVP treated in Chapter 5.

B.1 Problem Formulation

This section presents the governing equations for the propagation of an one-dimensional plane wave in an elastic half-space ($y \geq 0$) due to an excitation at the boundary. The one-dimensional wave equation can be written as

$$\frac{\partial}{\partial y}\sigma_{22}(y,t) = \rho\frac{\partial^2}{\partial t^2}v(y,t), \tag{B.1}$$

where $\sigma_{22}(y,t)$ is given by the constitutive equation

$$\sigma_{22}(y,t) = (\lambda+2\mu)\frac{\partial}{\partial y}v(y,t). \tag{B.2}$$

Substituting (B.2) into (B.1) yields

$$\frac{\partial^2}{\partial y^2}v(y,t) = \frac{1}{c_l^2}\frac{\partial^2}{\partial t^2}v(y,t), \tag{B.3}$$

as the half-space is initially at rest, the initial conditions are

$$v(y,0) = \dot{v}(y,0) = 0. \tag{B.4}$$

The boundary condition at $y = 0$ is given by the excitation signal and can be written as

$$\sigma_{22}(0,t) = -QF(t). \tag{B.5}$$

B.2 Integral Transform

To obtain an analytical solution to the BVP given in the previous section, the Laplace transform (4.13) is applied to the one-dimensional wave equation (B.3), which yields

$$\frac{\partial^2}{\partial y}\bar{v}\left(y,p\right)-\frac{p^2}{c_l^2}\bar{v}\left(y,p\right) \;=\; 0, \tag{B.6}$$

where p denotes the Laplace variable. A solution to this ordinary differential equation can be obtained by the following ansatz

$$\bar{v}\left(y,p\right) \;=\; A\left(p\right)e^{\frac{p}{c_l}y}+B\left(p\right)e^{-\frac{p}{c_l}y}. \tag{B.7}$$

For this problem, only a propagating wave into the positive y-direction is considered. Furthermore, it can be assumed that $\Re\left\{p\right\}\geq 0$ and hence $A\left(p\right)=0$, since the Laplace function has to be bounded in the range [5]. Thus the solution in the Laplace domain is obtained using (B.7) together with the transformed boundary condition (B.5)

$$\frac{\partial}{\partial y}\bar{v}\left(0,p\right) \;=\; -\frac{Q}{\lambda+2\mu}\bar{F}\left(p\right), \tag{B.8}$$

which yields

$$B\left(p\right) \;=\; \frac{1}{p}\frac{Qc_l}{\lambda+2\mu}\bar{F}\left(p\right). \tag{B.9}$$

Hence the solution in the Laplace domain can be written as

$$\bar{v}\left(y,p\right) \;=\; \frac{1}{p}\frac{Qc_l}{\lambda+2\mu}e^{-\frac{y}{c_l}p}\bar{F}\left(p\right). \tag{B.10}$$

B.3 Inverse Integral Transform

Applying the inverse Laplace transform to the solution in the Laplace domain (B.10) together with the integral property [5]

$$L^{-1}\left\{\frac{1}{p}\bar{f}\left(p\right)\right\} \;=\; \left(\int_0^t f\left(\tau\right)d\tau\right)H\left(t\right), \tag{B.11}$$

and the shifting theorem [5]

$$L^{-1}\left\{e^{-ap}\right\} \;=\; f\left(t-a\right)H\left(t-a\right), \tag{B.12}$$

yields the solution in the time domain

$$v\left(y,t\right) \;=\; \left(\frac{Qc_l}{\lambda+2\mu}\int_0^{t-\frac{y}{c_l}} F\left(\tau\right)d\tau\right) H\left(t-\frac{y}{c_l}\right). \tag{B.13}$$

REFERENCES

[1] Aboudi, J. and Benveniste, Y., "The nonlinear lamb problem," *Computer Methods in Applied Mechanics and Engineering*, vol. 6, pp. 319–334, 1975.

[2] Achenbach, J. D., *Wave Propagation in Elastic Solids*, vol. 16 of *Applied Mathematics and Mechanics*. Elsevier Science Publishers B.V., 1975.

[3] Balbás, J. and Tadmor, E., "CentPack." online at http://www.cscamm.umd.edu/centpack/software, July 2006. Available at: http://www.cscamm.umd.edu/centpack/software.

[4] Bermes, C., Kim, J., Qu, J., and Jacobs, L. J., "Experimental characterization of material nonlinearity using lamb waves," *Applied Physics Letters*, vol. 90, 2007.

[5] Bronstein, I. N., Semendjajew, K. A., Musiol, G., and Mühlig, H., *Taschenbuch der Mathematik*. Verlag Harri Deutsch, 2001.

[6] Cantrell, J. H., "Acoustic-radiation stress in solids. i. theory," *Physical Review B*, vol. 30, pp. 3214–3220, 1984.

[7] Debnath, L., *Nonlinear Partial Differential Equations for Scientists and Engineers*. Birkhäuser, 1997.

[8] Forrestal, M. J., Fugelso, L. E., Neidhardt, G. L., and Felder, R. A., "Response of a half-space to transient loads," *Proceedings Engineering Mechanics Division Specialty Conference, ASCE*, pp. 719–751, 1966.

[9] Gerald, C. F. and Wheatley, P. O., *Applied Numerical Analysis*. Addison-Wesley Publishing Company, 1994.

[10] Godlewski, E. and Raviart, P. A., *Numerical Approximation of Hyperbolic Systems of Conservation Laws*, vol. 118 of *Applied Mathematical Sciences*. Springer, 1996.

[11] Gould, P. L., *Introduction to Linear Elasticity*. Springer, 1994.

[12] Graff, K. F., *Wave Motion in Elastic Solids'*. Dover Publications, Inc, 1991.

[13] Hamilton, M. F. and Blackstock, D. T., *Nonlinear Acoustics*. Academic Press, 1998.

[14] Kurganov, A. and Tadmor, E., "New high-resolution central schemes for nonlinear conservation laws and convection-diffusion equations," *Journal of Computational Physics*, vol. 160, pp. 241–282, May 2000.

[15] Lamb, H., "On the propagation of tremors over the surface of an elastic solid," *Philosophical Transactions of the Royal Society of London*, vol. A 203, pp. 1–42, 1904.

[16] Levander, A. R., "Fourth-order finite-difference p-sv seismograms," *Geophysics*, vol. 53, pp. 1425–1436, 1988.

[17] LeVeque, R. J., *Finite Volume Methods for Hyperbolic Problems*. Cambridge Texts in Applied Mathematics, Cambridge University Press, 2002.

[18] McCall, K. R., "Theoretical study of nonlinear elastic wave propagation," *Journal of Geophysical Research*, vol. 99, pp. 2591–2600, 1994.

[19] Meurer, T., Qu, J., and Jacobs, L. J., "Wave propagation in nonlinear and hysteretic media - a numerical study," *International Journal of Solids and Structures*, vol. 39, pp. 5585–5614, 2002.

[20] Miklowitz, J., *The Theory of Elastic Waves and Waveguides*, vol. 22 of *Applied Mathematics and Mechanics*. Elsevier Science Publishers B.V., 1978.

[21] Oppenheim, A. V., Schafer, R. W., and Buck, J. R., *Discrete-Time Signal Processing*. Prentice Hall International, Inc., 1999.

[22] Powers, D. L., *Boundary Value Problems*. Harcourt Academic Press, 4 ed., 1999.

[23] Smith, R. T., Stern, R., and Stephens, R. W. B., "Third-order elastic moduli of polycrystalline metals from ultrasonic velocity measurements," *Journal of the Acoustical Society of America*, vol. 40, pp. 1002–1008, 1966.

[24] Tadmor, E., *Approximate Solutions of Nonlinear Conservation Laws*. No. 1697 in Lecture Notes in Mathematics, Springer, 1998.

[25] Taylor, M. E., *Partial Differential Equations III - Nonlinear Equations*, vol. 117 of *Applied Mathematical Sciences*. Springer, 1996.

[26] Thomas, J. W., *Numerical Partial Differential Equations - Finite Difference Methods*, vol. 22 of *Texts in Applied Mathematics*. Springer, 1995.

[27] Thomas, J. W., *Numerical Partial Differential Equations - Conservation Laws and Elliptic Equations*, vol. 33 of *Texts in Applied Mathematics*. Springer, 1999.

[28] Vanaverbeke, S. and Abeele, K. V. D., "Two-dimensional modeling of wave propagation in materials with hysteretic nonlinearity," *Journal of Acoustical Society of America*, vol. 122, pp. 58–72, 2007.

[29] Whitham, G. B., *Linear and Nonlinear Waves*. Pure and Applied Mathematics, Wiley-Interscience, 1999.

[30] Xu, H., Day, S. M., and Minster, J. H., "Two-dimensional linear and nonlinear wave propagation in a half-space," *Bulletin of the Seismological Society of America*, vol. 89, pp. 903–917, 1999.